Center for
Advanced Nuclear
Energy Systems

Massachusetts Institute of Technology
77 Massachusetts Avenue, 24-215
Cambridge, MA 02139-4307

(617) 452-2660
canes@mit.edu
canes.mit.edu

Advanced Nuclear Power Program

CONSEQUENCE-BASED SECURITY OF A SODIUM-COOLED GRAPHITE-MODERATED THERMAL MICROREACTOR (SGTR)

Jérémy Mangin, Amaury Le Person, Koroush Shirvan, Jeong Ik Lee, Andrew Whittaker, and Neil Todreas

Department of Nuclear Science and Engineering
Massachusetts Institute of Technology

MIT-ANP-TR-200
April 2024

Massachusetts Institute of Technology

ABSTRACT

Significant effort is now underway in the United States (US) to develop the licensing basis for advanced reactors, which vary greatly in terms of power rating, physical size, types of fuel and coolant, and civil construction. At the same time, commercial deployment of these reactors need to satisfy capital cost and operations and maintenance targets, for which they can be highly correlated to their licensing basis. On this front, shrinking the reactor building footprint and volume of materials, reducing or eliminating the need for on-site, 24-hour-a-day security personnel, and maximizing the number of possible sites, including urban areas and cities, will be key to the economic viability of smaller MWe advanced reactors. In August 2023, the US Nuclear Regulatory Commission (NRC) ruled on emergency preparedness for small modular reactors and other new nuclear technologies. NRC ruling provides optimism for a performance-based treatment of smaller MWe reactors. However, physical security considerations were not part of the ruling and the guidance in this area remains unclear.

This investigation performs a consequence-based analysis to determine the ability of a microreactor to withstand physical security attacks without the intervention of an on-site security team. The work utilizes a MIT-designed 15MW Sodium-cooled Graphite-moderated Thermal microReactor (SGTR) as the reference reactor. A scope of postulated security threats, organized by category (fire, blast, aircraft crash, sabotage), is considered. A screening process is conducted, using probabilistic and qualitative factors, to identify Design-Basis Threats (DBTs). Damage from each DBT is studied, and mitigation strategies against various threats are identified. Particular effort is devoted to quantifying the robustness of the reactor building's (RB) to mechanical damage and impacts. Each DBT source term is evaluated through examination of a primary coolant fire and the mechanistic estimation of source term during a Prolonged Loss-of-Heat-Removal (PLHR) scenario. Resulting public dose exposure is assessed using a Gaussian-plume atmospheric dispersion model. Dose exposure goals of 25 and 1 rem (250 and 10 mSv) are expressed in terms of Low Population Zone (LPZ) and Emergency Planning Zone (EPZ) sizes. When relevant, recommendations for offsite security response timing and its impact on accident source term are provided.

From the civil engineering perspective, employing a thick (~2 m) reinforced concrete (RC) radiation shield as a core enclosure is highly effective in preventing mechanical damage to the core from physical security events. Regarding radiological impacts, it is shown that a PLHR event does not pose a threat to public health. However, the analysis highlighted the vulnerability of the SGTR design to high coolant (sodium) activation. Design-Basis aircraft crashes and contact blasts, capable of damaging the primary heat exchanger could be a more limiting accident. Based on this finding, the design of the SGTR was modified such that the the primary exchanger would be moved to the 2m-thick RC radiation shield enclosure, safeguarding it from the considered DBTs. Overall, since the SGTR was originally designed to have minimal off-site consequences during a PLHR event, this resiliency during a beyond design basis accident translated to high resiliency from a physical security point-of-view while the reactor is in operation. Therefore, we conclude that there is high potential for SGTR to forgo a need for onsite-security guards to protect its reactor building from DBTs under normal operation. This conclusion is design specific, not applicable to other operational modes (e.g., transportation of a microreactor back to a central facility), and subject to uncertainty and scope of the study.

CANES PUBLICATIONS

Topical and progress reports are published under seven series:

Advances in Nuclear Energy Disciplines (ANED) Series
Advanced Nuclear Power Technology (ANP) Series
Nuclear Fuel Cycle Technology and Policy (NFC) Series
Nuclear Systems Enhanced Performance (NSP) Series
MIT Reactor Redesign (MITRR) Series
Nuclear Energy and Sustainability (NES) Series
Nuclear Space Applications (NSA) Series

Please visit our website (mit.edu/canes/) to view more publication lists.

MIT-ANP-TR-199	Emile Germonpre and Jacopo Buongiorno, **Feasibility study of decentralized hydrogen production using nuclear batteries** (January 2024).
MIT-ANP-TR-198	Lucas Lallemant, Jacopo Buongiorno, Shafiqul Islam and Laurent Vernon, **Design of Fission Batteries Process (FIBAPRO) Facility** (October 2023).
MIT-ANP-TR-197	Matthew Chew and Jacopo Buongiorno, **A Cybersecurity Framework for Nuclear Microreactors** (June 2023).
MIT-ANP-TR-196	Paul E. Roege(MIT ANPEG), Alexander L. Schoonen(INL), James R. Case (INL), Corey L. Beebe(INL), Ryan Cumings (MIT LL), Zachary A. Collier (Collier Research Systems), **Assessment of Potential Ground Force Capability Enhancement Using Nuclear Microreactors** (August 2022).
MIT-ANP-TR-194	W. Robb Stewart and K. Shirvan (MIT), **Capital Cost Evaluation of Advanced Water-Cooled Reactor Designs With Consideration of Uncertainty and Risk** (June 2022).
MIT-ANP-TR-193	K. Shirvan (MIT), **Overnight Capital Cost of the Next AP1000** (March 2022).
MIT-ANP-TR-192	R. MacDonald and J. Parsons (MIT), **The Value of Nuclear Microreactors in Providing Heat and Electricity to Alaskan Communities** (October 2021).
MIT-ANP-TR-191	C. W. Forsberg (MIT) and A. W. Foss (INL), **Markets and Economic Requirements for Fission Batteries and Other Nuclear Systems** (March 2021).
MIT-ANP-TR-190	J. Buongiorno (MIT), **An Economic Evaluation of Micro-Reactors for the State of Washington** (January 2021).
MIT-ANP-TR-189	C. W. Forsberg (MIT), P. Sabharwall (INL)and A. Sowder (EPRI), **Separating Nuclear Reactors from the Power Block with Heat Storage:** A New Power Plant Design Paradigm (November 2020).

MIT-ANP-TR-188 X. Zhao and M. Golay, **Symptom-Based Conditional Failure Probability Estimation for Selected Structures, Systems, and Components:** Minor Milestone Report: Project on Design of Risk-Informed Autonomous Operation for Advanced Reactors DOE/EXT- DE-NE0008873 Project number: 19-17435 (July 2020).

MIT-ANP-TR-187 J. Buongiorno, K. Shirvan, E. Baglietto, C. Forsberg, M. Driscoll, W. Robb Stewart, Enrique Velez-Lopez (MIT), H. Einstein (Civil & Environmental Engineering), Iain Macdonald (ArtEZ), Kennard Johnston (Morgan State Univ.) and Go Hashimoto (Univ. of Tokyo), **Japan's Next Nuclear Energy System (JNext)** (March 2020).

MIT-ANP-TR-186 Y. Cai and M. W. Golay, **A Framework for Analyzing Nuclear Power Multiunit Accident Scenarios and Providing Accident Mitigation and Site Improvement Suggestions** (September 2019).

MIT-ANP-TR-185 C. W. Forsberg (MIT), P. Sabharwall and H. D. Gougar (INL), **Heat Storage Coupled to Generation IV Reactors for Variable Electricity from Base-load Reactors: Changing Markets, Technology, Nuclear-Renewables Integration and Synergisms with Solar Thermal Power Systems** INL/EXT-19-54909 (September 2019).

MIT-ANP-TR-184 C. W. Forsberg, **Implications of Carbon Constraints on (1) the Electricity Generation Mix For the United States, China, France and United Kingdom and (2) Future Nuclear System Requirements (**March 2019).

MIT-ANP-TR-183 C. W. Forsberg, **Fluoride-Salt-Cooled High-temperature Reactor (FHR) Temperature Control Options: Removing Decay Heat and Avoiding Salt Freezing** (January 2019).

MIT-ANP-TR-182 J. Buongiorno, N. Sepulveda and L. Rush, **White Paper: Potential Applications of the Modern Nuclear Fuel Cycle to (South) Australia** (November 2018).

MIT-ANP-TR-181 C. Forsberg and P. Sabharwall, **Heat Storage Options for Sodium, Salt and Helium Cooled Reactors to Enable Variable Electricity to the Grid and Heat to Industry with Base-Load Reactor Operations** (September 2018).

MIT-ANP-TR-180 C. W. Forsberg, et al. **Integrated FHR Technology Development Final Report: Tritium Management, Materials Testing, Salt Chemistry Control, Thermal Hydraulics and Neutronics with Associated Benchmarking** (September 2018).

MIT-ANP-TR-179 C. W. Forsberg, N. Sepulveda and K. Dawson **Implications of Carbon Constraints on Electricity Generation Mix For the United States, China, France and United Kingdom** (August 2018).

MIT-ANP-TR-178 C. W. Forsberg, N. Sepulveda and K. Dawson **Commercialization Basis for Fluoride-salt-cooled High-Temperature Reactors (FHRs): Base-load Reactor with Heat Storage for Variable Electricity and High-Temperature Heat to Industry** (August 2018).

MIT-ANP-TR-177 S.T. Lam, C. W. Forsberg, and R. Ballinger **Understanding Hydrogen/Tritium Behavior on Carbon to Predict and Control Tritium in Salt Reactors: Experiments, Modeling and Simulation** (August 2018).

Massachusetts Institute of Technology

CONTENTS

ABBREVIATIONS

Abbreviation	Definition
BDBT	Beyond-Design-Basis Threat
BWR	Boiling Water Reactor
CDP	Concrete Damage Plasticity
CEDE	Committed Effective Dose Equivalent (Sv)
DBT	Design-Basis Threat
DCF	Dose Conversion Factor ($Sv.Bq^{-1}$)
DDE	Deep Dose Equivalent (Sv)
DOE or USDOE	U.S. Department of Energy
EOC	End Of Cycle
EPZ	Emergency Planning Zone - 1 rem TEDE threshold
FEM	Finite Element Method
FGR	Fission Gas Release
FP	Fission Product
HTGR	High Temperature Gas-cooled Reactor
IAEA or AIEA	International Atomic Energy Agency
KDE	Kernel Distribution Estimation
LWR	Light Water Reactor
LPZ	Low Population Zone - 25 rem TEDE threshold
LOCA	Loss-of-Coolant Accident
MAR	Material-at-Risk (Bq)
MHT	Maximal Hypothetical Threat
MHA	Maximum Hypothetical Accident
MST	Mechanistic Source Term
NB	Nuclear Battery
NEI	Nuclear Energy Institute
NPP	Nuclear Power Plant
NRC or USNRC	U.S. Nuclear Regulatory Commission
PLHR	Prolonged Loss-of-Heat-Removal
PLOF	Prolonged Loss-of-Flow
PWR	Pressurised Water Reactor
RC	Reinforced Concrete
RCCS	Reactor Cavity Cooling System
SDOF	Single Degree Of Freedom
SGTR	Sodium-cooled Graphite-moderated Thermal microReactor
SMR	Small Modular Reactor
SSC	Structures Systems and Components
TEDE	Total Effective Dose Equivalent (Sv)
US or U.S.	United States of America
TNT	Trinitrotoluene

Massachusetts Institute of Technology

LIST OF SYMBOLS

Symbol	Definition	Symbol	Definition
Fundamental Constants			
$\mathcal{N}_A = 6.02 \times 10^{23}$		Avogadro constant (mol^{-1})	
$R = 8.314$		Perfect gas constant $(J.K^{-1}.mol^{-1})$	
Section 2 - Material-at-Risk (MAR) Estimation			
${}^{A}_{Z}X$	Nuclide X of mass number A and atomic number Z	$n_{^AX}$	Amount of substance of nuclide ${}^{A}X$ (mol)
$N_{^AX}$	Number of atoms of nuclide ${}^{A}X$	M_X	Molar mass of element X $(g.mol^{-1})$
p_X	Partial pressure of gas X (Pa)	T	Temperature (K)
V	Volume (m^3)	t	Time (s)
Φ	Thermal Neutron flux $(cm^{-2}.s^{-1})$	$\sigma_{^AX}$	Cross section of nuclide ${}^{A}X$ for the reaction of interest (b)
$\lambda_{^AX}$	Decay constant of nuclide ${}^{A}X$ (s^{-1})	ρ	Density $(kg.m^{-3})$
Section 3 - Mechanistic Source Term Analysis			
$\Pi^i_{x,y}$	Pathway matrix - Transfer rate of nuclide i from compartment y to x (s^{-1})	$\Lambda^i_{x,y}$	Transport matrix - Transfer rate of nuclide i from compartment y to x (s^{-1})
$\lambda^i_{x,y}$	Removal matrix - Removal rate of nuclide i from compartment y to x (s^{-1})	$l_{x \longrightarrow y}$	Volumetric leakage rate from compartment x to y $(vol\ \%\ /\ day)$
$\dot{\epsilon}$	Creep rate (s^{-1})	ϵ	Creep strain (mm/mm)
σ_h	Hoop stress (MPa)	σ_m	Membrane stress (MPa)
σ_b	Bending stress (MPa)	E	Young's Modulus (GPa)
w	Thickness (m)	σ_x, σ_y, σ_z	Briggs Urban dispersion factors (m^{-1})
$\chi(x,y,z)$	Integrated activity concentration at the point of space (x,y,z) $(Bq.s.m^{-3})$	Γ	Source Term (Bq)
$\frac{\chi}{\Gamma}$	Dispersion factor $(s.m^{-3})$	u	Wind speed $(m.s^{-1})$
h	Height (m)	ν_d	Deposition velocity $(m.s^{-1})$
z_0	Average height of an adult (m)= 1.7	DCF	Dose Conversion Factor $(Sv.Bq^{-1})$
h^X_E	Effective dose equivalent coefficient of nuclide X $(Sv.Bq^{-1}.s^{-1}.m^3)$	BR	Breathing rate $(m^3.s^{-1})$
$CEDE$	Committed Effective Dose Equivalent (Sv)	DDE	Deep Dose Equivalent (Sv)
$TEDE$	Total Effective Dose Equivalent (Sv)	BR	Breathing rate $(m^3.s^{-1})$
Section 4 - External Fire Threats			
Q	Flow rate $(m^3.s^{-1})$	A	Area (m^2)
D	Diameter (m)	δ	Depth (m)
$\dot{m}''$	Effective mass burning rate $(kg.m^{-2}.s^{-1})$	$\dot{q}''$	Heat flux $(W.m^{-2})$
ϵ_s	Emissivity	σ	Stephan-Boltzman Constant $(\sigma = 5.67 \times 10^{-8}\ W.m^{-2}.K^{-4})$
Section 6 & 7 - Distant Blast, Contact Blast			
Z	Scaled distance $(m.kg^{-1/3})$	m_S	Mass of system S (kg)

Symbol	Definition	Symbol	Definition
R	Standoff distance (m)	L	Length of the wall (m)
f_y	Compressive strength of the steel rebar (MPa or psi)	E	Concrete Young's modulus (MPa)
ρ_c	Concrete density (lb/ft^3)	p	Maximum reflected overpressure (MPa)
W	Explosive Mass (kg eq. TNT)	I_r	Reflected impulse (MPa.ms)
t_d	Duration of the positive phase (ms)	y_m	Maximum displacement of the wall (m)
y_e	Maximum elastic displacement of the wall (m)	μ	Ductility ratio
y	Displacement of the equivalent SDOF system (m)	M_e	Equivalent mass of the SDOF system (kg)
k_e	Equivalent stiffness of the SDOF system (lb/in)	F_1	Maximum load (lb)
$f(t)$	Load time amplitude	T	Natural period of oscillation of the SDOF system (s)
M_t	Total system mass (kg)	k	Real system stiffness (lb/in)
K_{LM}	Transformation factor	R_m	Maximum mechanical resistance (lb)
d_t	Total RC wall thickness (in)	w	Wall/Slab width (in)
I	Moment of inertia (in^4)	k_{cr}	Cracked stiffness (lb/in)
g	Gravity constant $(= 32.17 ft/s^2)$	M_p	Bending moment resistance $(lb.in)$
M_{max}	Maximum bending moment resistance $(lb.in)$	A_s	Area of reinforcement (in^2)
d	Effective depth of the RC wall (in)	θ	Code-imposed bending moment security margin
ρ	Steel ratio	t_c	Distance between the outer concrete surface and the closest steel plate (in)
T_c	Thickness of the internal concrete layer (in)	t_s	Thickness of the steel plates (in)
P	Weight (N)	N	Normal reaction of the ground (N)
$F(t)$	Blast-induced force applied on Hesco barriers (N)	$p(t)$	Reflected overpressure (MPa)
S	Targeted area (m^2)	f	Friction coefficient between the ground and the system
$x(t)$	Hesco barrier displacement (m)	Δ	Damage parameter
σ	Stress (MPa)	ϵ	Strain
P_b	Breaching charge (kg eq. TNT)	K	Material factor
K_0	Material parameter (kg/m^3)	C	Tamping factor
D_1	Ejection crater diameter (m)	D_2	Spalling crater diameter (m)
D_3	Hole diameter (m)	δ	Ejection crater depth (m)
Section 8 & 9 - Aircraft Threats, Wind-borne Missile Impact			
x_c	Penetration depth (in)	t_p	Thickness to prevent perforation (in)
α_c	Penetration reduction factor	f'_c	Concrete compressive strength (psi)
N	Flat nose coefficient	f'_t	Concrete tensile strength (psi)

Symbol	Definition	Symbol	Definition
V	Missile speed (ft/s)	D	Average case engine outer diameter (in)
SE	Energy absorption capability $(lb.in)$	S_e	Extended impact surface (m^2)
E_a	Imparted kinetic energy $(lb.in)$	D_{fb}	Fireball diameter (m)
p_{NPP}	Probability of commercial aircraft strike on an NPP	f	Frequency of occurrence of commercial aircraft strike on an NPP $(/year)$
Section 10 - Consequence Evaluation of Design-Basis Threats			
LPZ	Low Population Zone (m)	EPZ	Emergency Planning Zone (m)

List of symbols used in the paper

Massachusetts Institute of Technology

LIST OF FIGURES

Massachusetts Institute of Technology

LIST OF TABLES

1 OVERVIEW

1.1 Motivation and background

For the first four decades of the commercial nuclear power industry, emphasis was placed on large light water reactors, of GWe-scale, which were assumed to provide economies of scale. These economies have not materialized in the US and Europe, as evidenced for example by the cost and schedule over-runs at Plant Vogtle, and the canceled build at Plant V.C. Summer. It is worth noting that this trend does not necessarily apply to Asia. The nuclear power industry has thus pivoted in the past two decades towards smaller, less expensive reactors, ranging in size from 0.1 MWe to 300 MWe, which have been variously described as micro-reactors (0.1 MWe to 10s of MWe) and Small Modular Reactors (SMRs, 30 MWe to 300 MWe). These technologies, described by the US Nuclear Regulatory Commission as advanced reactors (although we do not differentiate here between light water and non-light-water coolants), offer the promise of much reduced capital outlay and construction schedule. The reduction in the volume of nuclear fuel, described by others as material at risk, coupled with the use of accident tolerant fuels in many reactor designs, offers clear siting advantages that may not be possible with conventionally fueled large light water reactors. The possible disadvantages of advanced reactors are higher capital cost per MWe and greater operations and maintenance cost per MWe, as described below.

Most of the advanced reactor technologies are not new, having been developed for naval propulsion or for research, but not applied to civil energy production. The licensing of advanced reactors therefore constitutes a major challenge for the NRC, which is currently engaging a broad spectrum of stakeholders to update regulations and license review guidelines, which until recently have only addressed large LWRs. With the most recent rule on *Emergency preparedness for small modular reactors and other new technologies* (SECY-22-0001 [1]) adopted by the NRC on 08/14/2023, and aiming at offering a performance-based alternative to the deterministic requirements of Title 10 of the Code of Federal Regulations [2], advanced reactor licensing criteria will define the future of SMR and microreactor projects. Current regulations and licensing strategies are discussed in Section 1.2 of this report.

The study documented in this report focusses on microreactors and their exposure to physical security threats. A confidential list of predefined Design-Basis Threats (DBTs) and prescriptive security requirements are set as guidance by the NRC. Designed for traditional gigawatt-scale LWRs, these on-site personnel and emergency planning NRC requirements are oversized for the inherent risk attached to advanced reactors and too stringent to economically enable microreactor projects. A study published by Sandia National Laboratories on advanced reactor safeguards [3] recently indicated that a physical protection system for a microreactor amounting to 56 full-time equivalent (FTE) security guards might be required. The current average U.S. nuclear worker salary (plus overhead and benefits) is on the order of $180,000/year. For a 5 MWe microreactor operating 80% of the time, 56 FTEs translate to $290/MWh, which is economically crippling for most energy applications. This outcome motivates a paradigm shift in nuclear security from prescriptive to performance and consequence-based regulations. In this context, the alternative physical security requirements for advanced reactors allows the following steps (NRC-2017-0227-0036, [4]):

1. Eliminating the requirement for a minimum number of onsite armed responders

2. Eliminating all requirements for any onsite armed responders assigned to interdict and neutralize the Design Basis Threat (DBT) in cases where reliance on offsite law enforcement or other offsite responders to fulfill the interdiction and neutralization capabilities is sufficient[1]

3. Allowing alternative means for accomplishing delay other than with physical barriers

For microreactors to be economically viable, the presence of on-site armed, trained security guards around the clock must be either avoided or minimized. Consequently, microreactors must be designed to be able to deal passively with these threats and studies conducted to justify the capability of microreactors to withstand physical security scenarios until law enforcement intervention without the support of on-site personnel. This calls for ensuring that no significant adverse health or environmental consequences would result from man-made attacks on the reactor.

In this report, the potential severe accidents induced by a family of man-made external threats (i.e. aircraft crashes, blasts, sabotage and arson fires) are investigated for a Sodium-cooled Graphite-moderated Thermal microReactor (SGTR) design conceived by Shirvan et al. [5].

The primary aim of this study is to help build a standardized methodology to determine the ability of an advanced reactor to withstand physical security attacks without on-site intervention. Although specifically applied to the SGTR, the methodology could be generalized. This study is a continuation of Gateau's work on consequence-based analysis of microreactors [6].

1.2 Regulation overview

1.2.1 • Performance-based regulatory approach and Consequence-based analysis

As for LWRs, advanced reactors must prove to be able to withstand a set of adverse events such as operational accidents, natural phenomena hazards (floods, tornados, fires), and man-made external events. Several regulatory approaches to safety and security analysis methodology exist, namely, prescriptive, goal-setting and performance-based approaches.

The first, the **prescriptive regulatory approach**, traditionally used by the NRC, establishes specific requirements accompanied by acceptability criteria. It has the advantage of setting clear requirements and reducing the expertise required to carry out a certification process but was written for GWe-scale reactors.

The **goal-setting regulatory approach**, traditionally used by countries like France and the United Kingdom, sets safety targets and leaves it to the licensee to demonstrate that safety and security practices are sufficient to achieve established regulatory safety outcomes.

Finally, the **performance-based regulatory approach**, adopted by countries like Finland and Canada, establishes performance and outcomes as the primary basis for regulatory decision-making. It is the only regulatory approach which, rather than only focusing on the accident prevention and risk assessment, considers its potential impact as a safety target. A **consequence-based analysis**,

[1] For example, the MIT Research Reactor, situated in a densely populated urban area, employs precisely this approach, though it was formerly a possibility only for Non-Power Production and Utilization Facilities (NPUFs), including research reactors, falling under the jurisdiction of the Department of Energy (DOE) rather than the NRC.

consisting of estimating the impact on people, property or the environment and including onsite accident progression, offsite release of radioactive material, and mitigation measures has to be carried out for every scenario and the resultant risk compared with the safety goal (or target risk). For reactors planned for deployment in urban areas, it also involves scaling the risk by the density of population that could potentially bear the consequences of the related accident. The extensive description of safety and security scenarios has the advantage of providing a better understanding of the various potential security threats to a nuclear power plant. On the other hand, this regulatory approach greatly increases the licensee's burden of proof and requires from the regulatory body a high level of expertise to provide an informed decision.

The NRC performance-based and technology-inclusive regulatory approach for advanced reactors, *Final rule: Emergency preparedness for small modular reactors and other new technologies*, was approved as previously indicated on 08/14/2023 (SECY-22-0001 [1]). It serves as an alternative to the existing prescriptive and deterministic requirements described in the the Code of Federal Regulations [2], and apply to light-water SMRs, nonlight-water reactors (non-LWRs) and Non-Power Production and Utilization Facilities (NPUFs - category including research reactors).

1.2.2 • Current regulation for zones in siting and dose exposure

The regulations that will apply for the licensing process of advanced reactors is not finalized. To understand the current state of regulation and their potential applicability, exclusion area and low population zone are next defined, taken from 10 CFR-100.3 [2] :

- **Exclusion area** is the area surrounding the reactor, in which the reactor licensee has the authority to determine all activities including exclusion or removal of personnel and property from the area.
- **Low population zone (LPZ)** is the area immediately surrounding the exclusion area which contains residents, the total number and density of which are such that there is a reasonable probability that appropriate protective measures could be taken in their behalf in the event of a serious accident. A permissible population density or total population within the LPZ is not specified because the situation may vary from case to case.[2]

Regulations for the Exclusion Area Boundary (EAB) and the Low Population Zone (LPZ) are provided in 10-CFR-50.34 and 10-CFR-50.67 [2] :

"(1) An individual located at any point on the boundary of the exclusion area (EAB) for any 2 hour period following the onset of the postulated fission product release, would not receive a radiation dose in excess of 25 rem total effective dose equivalent (TEDE).

(2) An individual located at any point on the outer boundary of the low population zone, who is exposed to the radioactive cloud resulting from the postulated fission product release (during the entire period of its passage) would not receive a radiation dose in excess of 25 rem total effective dose equivalent (TEDE);"

[2] According to RG 4.7 [7], the LPZ must be sized such that "the boundary of the densely populated center containing more than 25,000 residents must be at least one-and-one-third times the distance from the reactor to the outer boundary of the LPZ".

- The Regulatory Guide 1.242 [8] on emergency preparedness for advanced reactors, which was adopted in August 2023 (see the NRC Commissioners decision SECY-22-0001 [1]), described the plume exposure pathway **emergency planning zone (EPZ)** for advanced reactors as "the area within which public dose [...] is projected to exceed 10 mSv (1 rem) total effective dose equivalent (TEDE) over 96 hours from the release of radioactive materials from the facility, considering accident likelihood and source term, timing of the accident sequence, and meteorology." Within this zone, predetermined, prompt protective measures must be extensively described as part of the reactor's Emergency Plan Response to be submitted to the regulatory body for licensing.

Traditional PWR regulation for EPZs is described in 10-CFR-50 [2] and in other NRC guidance documents. The NRC has historically distinguished a plume exposure pathway EPZ, set to 10 miles (16 km), to an ingestion pathway EPZ of 50 miles (80 km). As ingestion of contaminated foods and water is a longer-term concern, which does not apply in the early phase of a severe accident, RG 1.242 states that requirements regarding an ingestion pathway EPZ for advanced reactors are eliminated. As this work focuses on advanced reactors, the notion of EPZ will be limited to the definition of a plume exposure pathway EPZ given in RG 1.242 [8] for this study.

- The **site boundary** refers to "the line beyond which the land or property is not owned, leased, or otherwise controlled by the licensee". See 10-CFR-20.1003, "Definitions" [2].

At present, no legislation applicable to advanced reactors clearly defines a dose exposure limit that should apply to the site boundary. The NRC is expected to make a decision in the near future.

If microreactors are to be implemented in urban areas, it is clear that the boudary site should at least be limited to the low population zone (LPZ) defined in the law applicable to conventional LWRs.

Discussions are underway to determine whether, for advanced reactors, the limit to be applied to the site boundary ought to be 1 rem (i.e. equivalent to the EPZ). This discussion is supported by the U.S. Environmental Protection Agency (EPA), which in 2017 suggested that the public dose exposure limit be set at 1 rem for research reactors located in urban areas (referred to as Non-Power Production and Utilization Facilities NPUFs, and falling within the scope of guide RG 1.242), to take into account the proximity of citizens living close to these reactors. Nevertheless, RG 1.242 [8] takes into account the two situations where the emergency planning zone would be included or would exceed the site boundary, and refers to additional requirements for the second case.

This study focuses on determining the dose received by a member of the public standing at a given distance exposed for the entire duration of an accident to the resulting radioactive cloud. As it is not the aim of this work to settle the debate on the dose limit to be reached at the boundary site, the distances corresponding to doses of 25 rem and 1 rem are both calculated. Hereafter, the 25 rem limit is referred to as the "*Low Population Zone (LPZ)*" and the 1 rem limit as the "*Emergency Planning Zone (EPZ)*".

1.3 Objectives and detailed methodology

This work aims at determining the ability of a microreactor to withstand physical security attacks, meaning man-made external events or human actions that could be taken against the reactor, without

the intervention of an on-site security team.

The scope of physical security scenarios considered includes **fires**, **sabotage**, **blasts** and **aircraft crashes**. Sabotage scenarios consider threats of incapacitation of vital safety systems through direct physical interactions by intruders, including piping sectioning or obstruction leading to a decay heat system failure. Cyber sabotage threats were left out of this study, as control systems are not considered yet. Theft threats, which constitute an unprecedented physical security concern specific to container-size microreactors, were also set aside, due to the difficulty of translating this type of scenario in terms of radiological consequences. The intrusion of counterfeit components during the reactor construction was also discussed but considered out of the scope of this study due to the difficulty of translating this type of scenario into radiological consequences. With no security team on site, all these attack scenarios were initially considered as design-basis. Justifications are required to prove that they do not fall within this framework. These are provided in Section 3.1. Every event sequence analysis specifies the Initial Conditons (ICs), referring to physical facility features, to be distinguished from the Initial Assumptions (IAs), referring to external initial states.

For each DBT, the dose received by a member of the public standing at a given distance and exposed to the resulting radioactive cloud for the entire duration is determined. With the aim of complying as closely as possible to the traditional licensing process, assumptions and reasoning made to determine theses doses refer to a set of NRC-issued documents, with a particular focus on Regulatory Guides RG 1.242 [8] and RG 1.183 [9]. If made, further assumptions are expressly stated. The results provided by this study are, for a determined design-basis scope of physical security scenarios, the minimum sizes of the LPZ and EPZ, and, when applicable, the maximum time for an intervention team to stop the accident before the release exceeds the 1 rem EPZ limit. Discussion on the final zone in siting sizes for the reactor designs is finally provided.

The study is applied to a Sodium-Cooled Graphite-moderated Thermal microReactor (SGTR) designed by Shirvan et al. [5], and presented in Section 1.4. The following methodology is adopted:

1. Material-at-risk (MAR), which represents the total inventory of radioactive isotopes (fission products and activated material) that is likely to be released during an accident scenario, is assessed in Section 2.

2. In Section 3, a limit is defined within the Design-Basis frawework, and attack scenarios are posed as either DBTs or Beyond Design-Basis Threats (BDBTs). Representative scenarios (i.e., scenarios of maximum magnitude within the scope of the Design-Basis limit), standing for all threat categories (i.e., fire, blast, aircraft crash, sabotage), are finally listed.

3. For each representative scenario, the corresponding attack event sequence is detailed and the damage caused to the facility is assessed. Sections 4, 5, 6 and 7 cover external fire, sabotage, blast and aircraft crash threats respectively. Section 8 explores the topic of wind-borne missiles, which naturally extends from the discussion on aircraft impacts, and is insightful from a physical security perspective.

4. Section 9 computes the release and dispersion of radioactive material for representative DBT scenarios, utilizing prior damage assessment and MAR evaluation. Two models are employed: one of a primary sodium coolant pool fire and another of a Mechanistic simulation of a Prolonged Loss-of-Heat-Removal (PLHR). An extensive methodology for the Mechanistic Source Term

(MST) assessment is detailed in Section 9.4. Public dose exposure throughout the accident is determined relative to the microreactor's distance and the sizes of the emergency zones (LPZ and EPZ) are established. Additionally, for the PLHR scenario, the time before public dose exposure exceeds 1 rem is calculated, potentially informing the establishment of deadlines in an Emergency Response Plan.

5. Based on qualitative risk assessment, accident severity, and likability of a successful intervention, a Maximal Hypothetical Threat (MHT)[3] is defined in the Conclusions, which could be used to compute the necessary emergency zone sizes from a physical security perspective.

1.4 Presentation of the Reactor Design

The reactor considered for this study is a Sodium-cooled and Graphite-moderated Thermal microreactor (SGTR) developed by Shirvan et al. [5]. This design is similar to the Hallam reactor, a 75 MWe nuclear facility built in Nebraska in 1963 by Atomics International and shut down in 1964. This reactor operated for about 9 months. Additional operational and experimental feedback can be taken from the extensive study of Sodium Fast Reactors (SFRs) [10].

The SGTR's exact design is not finalized, and so this MIT report investigates a range of dimensions for the the reactor building and several variations of its features. These considerations make the study more readily applicable to other microreactors and allows discussion of the pros and cons of different design choices from a physical security perspective.

Key features of the SGTR are listed in Table 2. The achievable fuel burnup is low, since the reactor is specifically designed to minimize the source term while leveraging the availability of $< 5\%$ conventional UO_2 fuel.

Table 2: Basic information on the MIT SGTR

Thermal power (MWt)	15
Fuel type and enrichment	UO_2 - 4.8%
Fuel mass	1770 kgU
Discharge burnup	9.6 MWd/kgU
Cycle and thermal efficiency	Supercritical CO_2 Brayton 31%
Electric power (MW)	4.7
Coolant	Sodium (Na)
Coolant inlet/outlet temperatures (°C)	300/510
Coolant pressure	Atmospheric
Cladding material	316 Stainless Steel

SGTR's layout and safety systems are next described. SGTR's layout, relevant dimensions and main equipments are displayed in Figure 1. The drawing is not to scale. Section 6.1.4 studies the

[3]The terminology "Maximum Hypothetical Threat" is taken from the term "Maximal Hypothetical Accident (MHA)", specific to the licensing process of NPUFs including research reactors. The MHA bounds all credible accidents and can be used to illustrate the analysis of events and consequences.

possibility of adding additional physical barriers such as Hesco barriers to the current layout. Nevertheless, for the different source term estimations, no barriers external to the reactor building are considered.

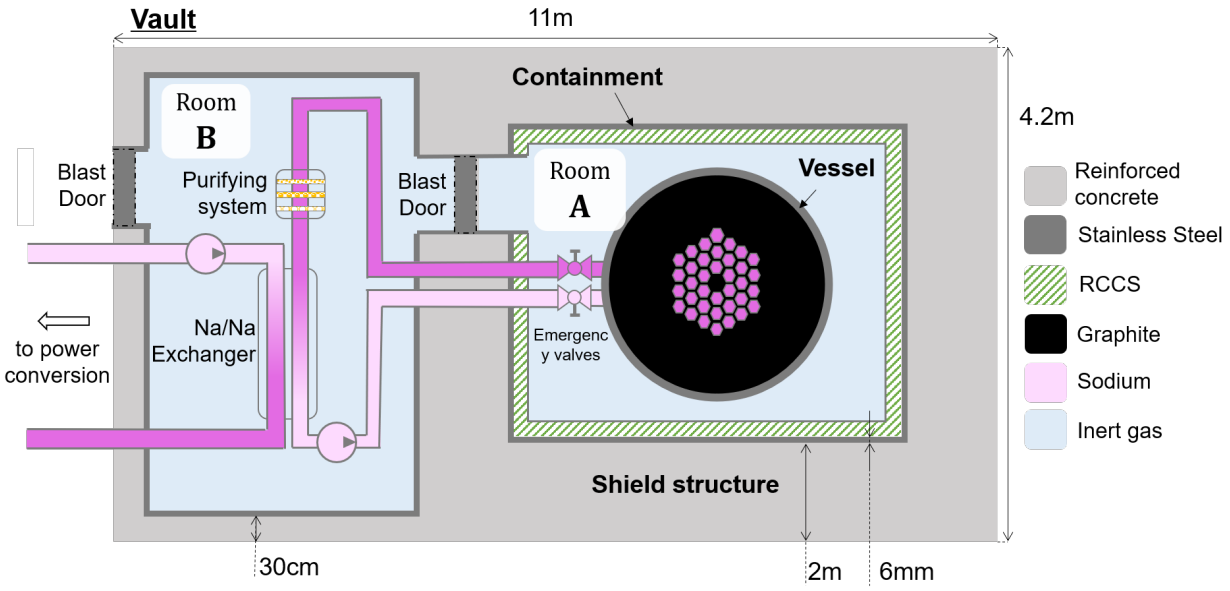

Figure 1: SGTR layout (Top-view, not at scale)

To protect important equipment against external threats and to prevent MAR from being released, the reactor mainly relies on reinforced concrete walls, which also act as radiation shield, (annotated "Shield structure" in Figure 1) surrounding a steel liner (annotated "Containment" in Figure 1).

The building or vault is divided into two rooms :

- Room A houses the core and is separated from the environment by a 6mm thick stainless steel liner and 2m of reinforced concrete. Room A's wall thickness of 2 m is selected for radiation shielding and hence is fixed.
- Room B houses important equipment for the operation and safety of the reactor, key among which is the heat exchanger between the primary and secondary sodium loops, from which activated coolant could be released in case of an accident. It is constructed with a 6mm liner and 300mm-thick RC walls and roof.

As a working assumption, the external dimensions of the vault will be taken as $11m$ of length and $4.2m$ of width and height.

Reactor Cooling Cavity system (RCCS): The RCCS, hatched in green in Figure 1, is a passive decay heat removal system designed in case of a primary loop Prolonged Loss of Flow (PLOF). When the reactor shuts down, the decay heat is radiated from the vessel, through the inert gas layer, to the RCCS pipes, where air flow is maintained by natural convection. A study of this mechanism and a thermal model of the SGTR is presented in [11].

Primary sodium drain mechanism: In certain cases involving an unplanned reactor shutdown (including the detection of a physical security attack or a coolant loss-of-flow accident), the primary coolant can be drained by gravity to a tank beneath the reactor building. The volume of sodium coolant stored in the reactor core is 170 L ($0.17m^3$). The inventory of sodium coolant including the pipelines, heat exchanger and purifying system is approximately 340 L ($0.34m^3$). The time required to drain the primary system to the reservoir is approximately 5 minutes. The primary sodium coolant is drained in the event of an unplanned reactor shutdown because :

- In the case of a PLOF, draining the coolant would prevent sodium boiling in the vessel, which could trigger vessel pressure rise, vessel breach, and coolant radioactivity release.
- Since the reactor has a thermal spectrum, the primary sodium is expected to be highly activated (a hundred times more than in a sodium fast reactor of the same power). Primary sodium coolant activation release constitutes one of the main vulnerabilities of the SGTR design. As described in Section 9.3.3, the radioactivity release into the atmosphere resulting from a primary sodium fire could result in a significant public dose exposure. Supported by the results of this study, it is indeed considered to be safer to drain the coolant, foregoing the sodium's ability to scrub fission products in case of cladding breach, rather than risking liberating the radioactivity held in the coolant itself.

The drain mechanism is not yet resolved. The assumption here is that the primary sodium is drained from the vessel and replaced by an inert gas. Sodium holdup in the primary system and its volatilization, contributing to the accident source term, is taken into account in subsequent analysis. Draining the sodium is conservative in terms of assessing radionuclide transport to the atmosphere in case of a fuel-related accident, since volatile fission products cannot be scrubbed by the coolant. It also greatly simplifies the study of a fuel-related accident progression and therefore the process of proving that the reactor is safe enough, by eliminating many potential subsequent event sequences induced by multiple sodium interactions with the reactor's subsystems.

2
MATERIAL-AT-RISK (MAR) ESTIMATION

The Material-at-Risk (MAR) has to be first evaluated to estimate the total effective dose equivalent at the site boundary for any accident scenario. MAR is the total inventory of radioactive material present under nominal conditions and likely to be released during an accident. The most significant part of the MAR comes from fission products produced within the fuel (accounting for approximately 99% of all material-at-risk). However, it is not possible to neglect other sources of radioactivity for a new reactor concept without justification. This is because a part of minor radioactivity present in components other than fuel can have high probability of being released in full during an accident, and can become a significant part of the source term. This is particularly the case for radioactive elements contained in coolant or moderator. These elements are activated by the neutron flux, and potentially released in case of a leak in the primary loop.

In the case of SGTR, sodium activation in the primary loop is one of the main concerns for the MAR. Indeed, due to the high cross-section of ^{23}Na in the neutron thermal energy spectrum, the activity of the sodium coolant should be two to three orders of magnitude higher than in a fast reactor of the same power. The radioactivity due to the activation of graphite impurities is also considered, which is likely to be released in case of graphite fire. Assumptions will thus be made about the amount of impurities contained in the graphite moderator used for the reactor. The containment material activation is ignored in this study, as it is minimal and unlikely to be released into the atmosphere during an accident. The radioactivity from cladding impurities released to the coolant is also neglected, since this contribution is expected to be a small amount in the core. MAR inventories for SGTR have been estimated through depletion calculations performed using the SERPENT Monte Carlo code. To crosscheck values obtained from SERPENT and add to the result the contribution of impurities, a simple algebraic model for each significant MAR source is developed. The new numerical value is compared to SERPENT results. Later in the study, MAR issued from SERPENT results is used for the radiological release evaluation.

2.1 Fission products inventory - UO_2 fuel

The fuel for the SGTR is Uranium Dioxide (UO_2) with a 4.8% enrichment level. It is bounded by a blanket of natural uranium fuel, at the top and bottom of the fuel rods.

MAR determination scaled from the USNRC estimated inventory A first evaluation of the MAR in the fuel for SGTR at the end of cycle can be performed by using the results of the report NUREG-1887 [12]. The USNRC estimated an inventory of the most important radionuclides in terms of health effects, for a UO_2-fueled $1MW_{th}$ reactor with a burnup of 30 MWd/kgU. Their results are presented in Table 3:

This inventory defined as I_0 needs to be adjusted to the established power of 15 MWth for the MIT nuclear SGTR design. Moreover, the inventory needs to be scaled-up to the right burnup for radionuclides with a half-life exceeding one year, which is 9.6 MWd/kgU in the case of the SGTR. Indeed radionuclides with long half-life compared to the fuel cycle tend to accumulate during operation.

Table 3: Nuclear power plant core inventory during operation for low enriched uranium fuel (30 MWd/kgU burnup)

Nuclide	Core inventory [Ci] (UO_2 1MWt 30MWd/kgU)	Nuclide	Core inventory [Ci]
Ba-140	5.30E+04	Ru-103	3.70E+04
Ce-144	2.80E+04	Ru-106	1.33E+04
Cs-134	4.17E+03	Sb-127	2.00E+03
Cs-136	1.00E+03	Sb-129	1.10E+04
Cs-137	2.67E+03	Sr-89	3.10E+04
I-131	2.80E+04	Sr-90	2.00E+03
I-132	4.00E+04	Sr-91	3.70E+04
I-133	5.70E+04	Te-129m	1.80E+03
I-134	6.30E+04	Te-131m	4.00E+03
I-135	5.00E+04	Te-132	4.00E+04
Kr-85	3.17E+02	Xe-131m	3.30E+02
Kr-85m	8.00E+03	Xe-133	5.70E+04
Kr-87	1.60E+04	Xe-133m	2.00E+03
Kr-88	2.30E+04	Xe-135	1.10E+04
La-140	5.30E+04	Xe-138	5.70E+04
Mo-99	5.30E+04	Y-91	4.00E+04
Np-239	5.50E+05		

In contrast, short-lived radionuclides tend to reach equilibrium and their accumulated mass does not depend on the burnup. Thus, the adjustment formula that should be applied to a radionuclide with a half-life over 1 year is shown in Equation 1:

$$\mathrm{I}_{SGTR} = \mathrm{I}_0 \times \mathrm{Power}_{SGTR}[\mathrm{MW}] \times \frac{\mathrm{BURNUP}_{SGTR}}{30\mathbf{MWd/kgU}} \tag{1}$$

For radionuclides with a half-life below 1 year, the adjustment must be made using equation 2:

$$\mathrm{I}_{SGTR} = \mathrm{I}_0 \times \mathrm{Power}_{SGTR}[\mathrm{MW}] \tag{2}$$

It is noted that radionuclides with a half-life below 0.5 day will be screened out in this study, since it is expected that any such radionuclide will decay quickly before causing any health effects to the public.

By applying this method to every nuclide in Table 3, the first estimation of the MAR for the fuel can be obtained. The results are summarized in Table 4:

For example, we have $MAR_{^{131}I} = 4.2 \times 10^5 Ci = 1.6 \times 10^{16} Bq$.

If the total fuel MAR is to be evaluated, these activities can be added. The total fuel MAR is $1.57 \times 10^7 Ci = 5.8 \times 10^{17} Bq$. However, the sum is not relevant for the determination of the source term later, since different nuclides will be released in different ways and therefore the source term contribution is not linearly dependent on the total MAR.

Table 4: MAR for fuel in the MIT SGTR scaled from the USNRC initial inventory

Nuclide	**Activity considered** [Ci]	**Nuclide**	**Activity considered [Ci]**
Ba-140	7.95E+05	Ru-103	5.55E+05
Ce-144	4.20E+05	Ru-106	6.38E+04
Cs-134	2.00E+04	Sb-127	3.00E+04
Cs-136	1.50E+04	Sb-129	0.00E+00
Cs-137	1.28E+04	Sr-89	4.65E+05
I-131	4.20E+05	Sr-90	9.60E+03
I-132	0.00E+00	Sr-91	0.00E+00
I-133	8.55E+05	Te-129m	2.70E+04
I-134	0.00E+00	Te-131m	6.00E+04
I-135	0.00E+00	Te-132	6.00E+05
Kr-85	1.52E+03	Xe-131m	4.95E+03
Kr-85m	0.00E+00	Xe-133	8.55E+05
Kr-87	0.00E+00	Xe-133m	3.00E+04
Kr-88	0.00E+00	Xe-135	0.00E+00
La-140	7.95E+05	Xe-138	0.00E+00
Mo-99	7.95E+05	Y-91	6.00E+05
Np-239	8.25E+06		

MAR determination using SERPENT depletion studies Another way to estimate the MAR for the UO_2 fuel is to rely on the depletion calculation. SERPENT is a Monte-Carlo code capable of performing such calculation. Prof. Shirvan's team uses the code to design the MIT SGTR, and was able to transmit the results concerning fuel activity at End of Cycle (EOC). The results were then filtered with the half-life half-day screening criterion. The nuclides with an activity over $10^5 Ci$ are presented in Table 5:

For example, we have $MAR_{^{131}I} = 3.85 \times 10^5 Ci = 1.4 \times 10^{16} Bq$.

The total fuel MAR is $1.93 \times 10^7 Ci = 7.1 \times 10^{17} Bq$. This value is slightly higher than the value obtained from the USNRC inventory (5.8×10^{17}). This difference represents an increase of 22% of the USNRC inventory value. The possible explanation is that first the reactor has different neutron energy spectrum even though both the MIT SGTR and and the USNRC reference reactor are thermal reactors. Moreover, the SERPENT calculation may consider radionuclides missing from NUREG-1887 inventory as shown in Table 3. Table 6 show these neglected radionuclides with activity larger than 10^5 Ci. The "major contributors" account for almost all the difference between the 1.57×10^7 Ci total fuel MAR derived from the USNRC inventory, and the 1.93×10^7 Ci total fuel MAR yielded by the code. The value from the SERPENT code was used in the following sections of this report.

2.2 Sodium coolant

2.2.1 • Pure coolant case

Several assumptions are made considering sodium coolant activation. First, only the most likely and significant nuclear reaction path is taken into account in sodium activation. (Among other things, the

Table 5: Main contributors to the fuel MAR ($Activity > 10^5 Ci$)

Nuclide	**Activity [Ci]**
Np239	6.37E+06
Xe133	8.38E+05
I133	8.36E+05
Nb95	7.60E+05
Zr95	7.58E+05
Mo99	7.23E+05
La140	7.50E+05
Ba140	7.45E+05
Ce141	7.05E+05
Pr143	6.90E+05
Ce143	6.90E+05
Y91	6.31E+05
Ce144	6.00E+05
Te132	5.58E+05
Zr97	5.37E+05
Sr89	5.02E+05
Ru103	4.92E+05
I131	3.85E+05
Nd147	2.73E+05
Rh105	2.55E+05
Pm149	1.44E+05
U237	1.31E+05
Pm147	1.26E+05
Ru106	1.18E+05

activity of ^{22}Na is neglected) :

$$^{23}Na + n \longrightarrow ^{24}\ Na \tag{3}$$

By comparing the orders of magnitude of the cross-sections of ^{23}Na for this reaction in the thermal range ($\sigma_{thermal} \approx 10^{-1}\ b$) and the fast neutron range ($\sigma_{fast} \approx 10^{-4}\ b$), and considering that the reactor of interest is a thermal reactor, only the thermal part of the energy spectrum is considered to estimate the amount of ^{24}Na formation.

The half life of ^{24}Na is 15h, i.e. negligible when compared to the irradiation time of the reactor (3 years), it is thus assumed that its activity has reached a steady state : $\frac{dn_{^{24}Na}}{dt} = 0$. The equations describing the amount of ^{24}Na in the coolant (in mol) are the following :

$$\begin{cases} \frac{dn_{^{23}Na}}{dt} = -\Phi\sigma_{^{23}Na}n_{^{23}Na} \\ \frac{dn_{^{24}Na}}{dt} = \Phi\sigma_{^{23}Na}n_{^{23}Na} - \lambda_{^{24}Na}n_{^{24}Na} \end{cases} \tag{4}$$

With :

Table 6: List of the major contributors to the fuel MAR missing from NUREG-1887 but considered in SERPENT simulations

Major contributors missing from NUREG-1887	Activity [Ci]
Zr95	7.58E+05
Zr97	5.37E+05
Nb95	7.60E+05
Rh105	2.55E+05
Ce141	7.05E+05
Ce143	6.69E+05
Pr143	6.90E+05
Nd147	2.73E+05
Pm147	1.26E+05
Pm149	1.44E+05
U237	1.31E+05
Total major contributors	4.56E+06

- $\sigma_{^{23}Na} = 0.26\ b$, the cross-section of ^{23}Na for the studied reaction at 0.1 eV according to the JEFF-3.3 database.
- $\lambda_{^{24}Na} = 1.29 \times 10^{-5}\ s^{-1}$, the decay constant of ^{24}Na
- $\Phi = 1.2 \times 10^{13}\ cm^{-2}.s^{-1}$, the neutron flux in the core integrated over the thermal peak (0.02 eV - 0.5 eV). (Value obtained through design studies)

When the steady state assumption is applied to the above set of equations :

$$\frac{n_{^{24}Na}}{n^0_{^{23}Na}} = \frac{\Phi\sigma_{^{23}Na}}{\lambda_{^{24}Na} + \Phi\sigma_{^{23}Na}} \approx 0.00002\% \tag{5}$$

Knowing that the volume of sodium coolant for the MIT SGTR is $V_{coolant} = 0.09m^3$ and the coolant temperature range is T = 300 - 510 °C ($< T > = 405$ °C), the amount of sodium in the coolant can be estimated using the molar mass of sodium $M_{Na} = 22.98g.mol^{-1}$ and the following density correlation applicable between 100 and 800°C : $\rho(T) = 949 - 0.223T - 0.0000175T^2\ kg.m^{-3}$ with T in °C. [13]

$$n^0_{^{23}Na} = \frac{\rho(< T >)V_{Na}}{M_{Na}} = 3.35 \times 10^3\ mol \tag{6}$$

The activity of the sodium coolant is then computed using the decay constant of ^{24}Na and the Avogadro constant $\mathcal{N}_A = 6.02 \times 10^{23} mol^{-1}$,

$$MAR_{Na} = n_{^{24}Na} \times \mathcal{N}_A \times \lambda_{^{24}Na} = 6.3 \times 10^{15}\ Bq \tag{7}$$

The depletion studies in the core performed by the design team estimated a total coolant activity of $9.2 \times 10^{15}\ Bq$. However, this study also considers the activity of the sodium isotope ^{24m}Na, with an half-life of $20ms$. If ^{24m}Na is to be taken into account to determine the surrounding activity of the reactor during operation, in case of release or if the reactor shutdowns, this activity completely dissapears in a matter of seconds. It is therefore not accounted for in the MAR. The final MAR

result obtained by depletion studies is $MAR_{Na} = 5.17 \times 10^{15}\ Bq$. This result is of the same order of magnitude as the simple model developed above. The discrepancy in the results can be explained by the neglected reactions such as the fast neutron influence and activity of ^{22}Na.

2.2.2 • Sodium coolant impurities

The model described above and design depletion studies only consider the case of a pure coolant. However, impurities are also to present in the coolant and can account for a contributor of Material-at-risk. These impurities primarily consist of dissolved corrosion products originating from stainless steel. The corrosion products precipitate from cladding surface, become activated and redissolve. Iron and cobalt are the primary impurities contributing to coolant activity, but their activities are negligible compared to the pure coolant activation. For example, considering a high iron impurity concentration of $500\mu g/kg$ of coolant, and without accounting for the depletion of ^{55}Fe, results in a conservative coolant activity of approximately $10^7\ Bq/kg$ of coolant after three years of operation, totaling $10^9\ Bq$ for the entire coolant capacity. However, this remains insignificant compared to the high coolant activation reaching $10^{15}\ Bq$.[4]

Without quantitative information on the primary coolant purifying system's performances, impurity levels in the coolant during operation cannot be assessed more precisely. Nevertheless, compared to the high sodium coolant activity, the activity coming from activated impurities is expected to be negligible.

2.3 Graphite impurities

Simple model Graphite is used as moderator in the MIT SGTR and it is massively present inside the core. Graphite is expected to become activated by the neutron flux. Most of the radioactivity at EOC comes from impurities which were initially present in the graphite matrix and became activated. Determining the maximum quantity and the nature of these impurities in the graphite that will be used is crucial if the MAR for graphite has to be computed precisely. However, given the fact that this graphite MAR will very likely to be small compared to the fuel MAR and the fact that the technical specification of MIT SGTR graphite is not determined, the initial amount and types of impurities are estimated.

A report from the USNRC[4] gathers results about the concentration of the most common impurities for different types of nuclear grade graphite. "Average nuclear grade graphite" is assumed by taking the median value among various vendors for every impurity for this initial estimation. The results are presented in Table 7.

According to the previous study on graphite decommissioning [5], the main radionuclides constituting the MAR for graphite are :

- ^3H coming from impurity ^6Li
- ^{60}Co coming from impurity ^{59}Co

[4]The contribution of ^{59}Fe, which quickly reaches equilibrium during reactor operation, is disregarded here due to its concentration being two orders of magnitude lower than that of ^{55}Fe.

- ^{14}C coming from impurity ^{14}N and ^{13}C naturally present
- ^{63}Ni coming from impurity ^{62}Ni
- ^{36}Cl coming from impurity ^{36}Cl
- ^{41}Ca coming from impurity ^{40}Ca
- ^{55}Fe coming from impurity ^{54}Fe

Knowing the initial concentration of every element, and the natural abundance of the isotope that leads to the production of a radionuclide, a few assumptions were made to facilitate the calculation of MAR :

1. Only the most likely nuclear reaction path for the radionuclide of interest is considered.
2. The radioactive decay of the radionuclide of interest is neglected, since its half-life is very long compared to the lifespan of the reactor.
3. Only the interaction with thermal neutrons is considered.

With these assumptions, the formation rate of the radionuclide of interest is expressed in Equation 8:

$$\frac{\mathrm{d}N_2}{\mathrm{d}t} = \sigma_{1\to2} \times \phi \times N_1(t) \tag{8}$$

We apply to every impurity concentration the process expressed in equation 9 :

$$N_2 = N_1(0) \times A \times \sigma_{1\to2} \times \phi \times t \tag{9}$$

Where

- N_2 is the concentration of the radionuclide of interest end of cycle $[cm^{-3}]$
- N_1 is the initial concentration of the impurity $[cm^{-3}]$
- A is the natural abundance of the isotope of interest
- $\sigma_{1\to2}$ is the average thermal cross-section of the reaction of interest $[cm^{-2}]$
- ϕ is the thermal neutron flux $[cm^{-2}.s^{-1}]$
- t is the time of exposure, that is the fuel cycle duration [s].

Note that all those values are spatial-averages for the core.

For SGTR, the design team provided $\phi = 1.24 \times 10^{13} cm^{-2}.s^{-1}$, and a time of exposure of 1000 days that corresponds to a burnup of 9.6 MWd/kgU.

The analysis parameters and the results are summarized in Table 7. The most problematic impurity is lithium, since the thermal cross-section for the reaction producing ^{3}H is very large compared to the reactions in other impurities. This model yields an activity per g of graphite for each radionuclide of interest. For example, the ^{3}H activity in graphite is 1.31×10^{5} Bq/$g_{graphite}$. After summing the activities per gram of graphite of each radionuclide mentioned in Table 7, the total activity is

3.06×10^5 Bq/$g_{graphite}$. The mass of graphite in the core is 2.4×10^7g. Therefore the MAR for graphite becomes $1.99 \times 10^2 Ci = 7.35 \times 10^{12} Bq$. It is only a small fraction of the fuel MAR, but at the same time the radioactivity in graphite can be released more easily than that in the fuel, during an accident. This is part of the reason why it is important to estimate the MAR from every material inside the core even though the fuel is responsible for the vast majority of the total activity.

Table 7: Main input parameters and results of the estimation by hand of graphite activation in SGTR

Graphite reference / Impurity	Li [ppm]	Co [ppm]	Cl [ppm]	Ni [ppm]
IG-110	14	0,05	4,1	1,1
Toyo Tanso High-Purity	0,001	0,001	0	0,006
NBG-17	0,21	0,11	0	1,2
NBG-18	0,05	0,2	0	12
PCEA	0,01	0,05	0,19	0,1
Median concentration [ppm]	0,05	0,05	0	1,1
Considered isotope	Li6	Co59	Cl35	Ni62
Natural abundance	0,0759	1	0,7576	0,036345
Considered concentration of this isotope [ppm]	0,003795	0,05	2,2	0,0399795
Radioactive product	H3	Co60	Cl36	Ni63
Average Cross-section [b]	380	15	18	6
Source of cross-section	ENDF/B-VII, MT105	ENDF/B-VII, MT102	ENDF/B-VII, MT102	ENDF/B-VII
Concentration of radioactive product EOC [cm-3]	1,545E+14	8,0352E+13	4,2426E+15	2,5699E+13
Concentration of radioactive product EOC [g-1 of graphite]	7,3572E+13	3,8263E+13	2,0203E+15	1,2238E+13
Half-life [s]	388789632	166344100	9,4988E+12	3158915000
Activity [Bq/g of graphite]	1,31E+05	1,59E+05	1,47E+02	2,68E+03

Graphite reference / Impurity	Ca [ppm]	Fe [ppm]	Max N [ppm]	C natural
IG-110	4,5	0,55	————	————
Toyo Tanso High-Purity	0,08	0,06	————	————
NBG-17	2,2	26	————	————
NBG-18	8	50	————	————
PCEA	0,19	0,06	————	————
Median concentration [ppm]	2,2	0,55	10	1,00E+23
Considered isotope	Ca40	Fe54	N14	C13
Natural abundance	0,969	0,05845	0,9964	0,01103
Considered concentration of this isotope [ppm]	2,1318	0,0321475	9,964	11030
Radioactive product	Ca41	Fe55	C14	C14
Average Cross-section [b]	0,17	0,9	0,75	0,0005
Source of cross-section	ENDF/B-VII, MT102	ENDF/B-VII, MT102	ENDF/B-VII, MT103	JEFF-3,3
Concentration of radioactive product EOC [cm-3]	3,8827E+13	3,0997E+12	8,0063E+14	5,9086E+14
Concentration of radioactive product EOC [g-1 of graphite]	1,8489E+13	1,4761E+12	3,8125E+14	2,8136E+14
Half-life [s]	3,2189E+12	86373150	1,7988E+11	1,7988E+11
Activity [Bq/g of graphite]	3,98E+00	1,18E+04	1,47E+03	1,08E+03

Estimation using SERPENT depletion calculation A depletion study was run using SERPENT, with the initial impurities specified in Table 7, for a power of 15MWth. The results are gathered in Table 8, and compared with the hand-estimation:

Table 8: Comparison between the estimated activity and the SERPENT simulated activity in graphite after 3 years

Radionuclide	**Activity Hand-calculation [Bq]**	**Activity SERPENT simulation [Bq]**
^{3}H	3.13E+12	5.45E+12
^{60}Co	3.81E+12	2.592E+12
^{35}S	Not calculated	2.56E+12
^{33}P	Not calculated	6.20E+11
^{14}C	6.10E+10	6.76E+10
^{55}Fe	2.83E+11	5.08E+10
^{63}Ni	6.41E+10	1.34E+10
^{36}Cl	3.52E+09	1.19E+09
^{41}Ca	9.51E+07	2.50E+07
Other	Not calculated	3.45E+11
Total	**7.28E+12**	**1.17E+13**

It should be noted that all the nuclides listed in Table 8 have a half-life longer than 0.5 day. However the total activity yielded by SERPENT of 1.17×10^{13} Bq includes short-lived nuclides which have not been screened out since their cumulative activity in this particular case is very small (less than 3.45×10^{11} Bq) compared to the total graphite activity. Therefore the contribution to the MAR from graphite will be considered to be $MAR_{graphite} = 1.17 \times 10^{13}$ Bq.

2.4 Stainless steel

The fuel cladding as well as the spacers between fuel pins are made of stainless steel. Their composition is shown in Table 9. No impurities are considered.

Table 9: Composition of SS316 in terms of weight fraction

Element	**Weight %**
Ni	12.00
Cr	17.00
Mo	2.50
Fe	65.345
Si	1.00
Mn	2.00
C	0.080
P	0.045
S	0.030

From the SERPENT depletion calculation, the nuclides with activity over $10^{3}Ci$ are extracted and presented in Table 10:

Table 10: Main contributors to the stainless steel MAR ($Activity > 10^3 Ci$)

Nuclide	Activity [Ci]
Fe59	5.45E+04
Cr51	2.15E+04
Fe55	8.20E+03
Mn54	6.61E+03
Mo99	3.14E+03
Co58	1.40E+03

The MAR for the stainless steel of which the core is composed (cladding and spacers) amounts to $9.60 \times 10^4 Ci = 3.56 \times 10^{15} Bq$.

2.5 Summary of results

The figure below provides an overview of Material-at-Risk (MAR) sources for SGTR and their relative weights at end-of-cycle under nominal conditions. Although the relative fuel share in MAR seems overwhelming compared to other contributors, primary sodium coolant activation is actually one of the main concerns and vulnerabilities for this design. Indeed, as pointed out in the second paragraph in the introduction to Section 2, due to the high cross-section of ^{23}Na in the neutron thermal energy spectrum, the activity of the sodium coolant is two to three orders of magnitude higher than in a fast reactor of the same power, resulting in coolant activity accounting for a significant share of MAR.

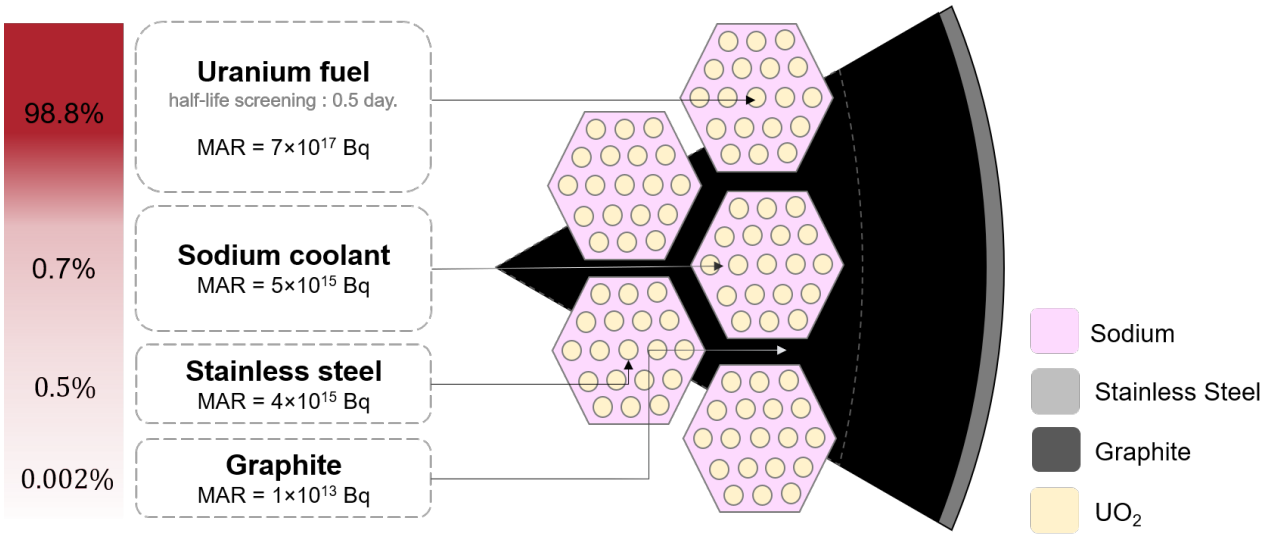

Figure 2: MAR sources for SGTR - 15MWth - EOC = 3 years

3
REPRESENTATIVE SCENARIOS OF DESIGN-BASIS THREATS (DBTS)

The scope of physical security scenarios considered includes **fires**, **blasts**, **aircraft crashes** and **sabotage**. Sabotage scenarios consider threats of incapacitation of vital safety systems through direct physical interactions by intruders, including piping failure or obstruction leading to a decay heat system failure. Cyber sabotage threats were excluded from this study, since control systems are not considered yet at this stage of the design process. Theft threats, which constitutes an unprecedented physical security concern specific to container-size microreactors, were also set aside, due to the difficulty of translating this type of scenario into terms of radiological consequences. The introduction of counterfeit components during the reactor construction was has not been explored due to the difficulty of translating this type of scenario into terms of radiological consequences. With no security team on site, all these attack scenarios should initially be considered as Design-Basis. Justifications are required to prove that they do not fall within this framework. These are provided in subsection 3.1.

Initial Assumptions (IAs) When addressing a design-basis threat, it is assumed that intruders gain full possession of the reactor facility, having direct access to the vault's walls and can perform any malicious activities they are technically capable of doing within a "reasonable" time period. Intruders are assumed to be on foot and more specifically cannot directly access the vault in a vehicle, meaning that they have to carry themselves the explosive or flammable material they want to use, which limits their capacity. On that matter, Section 6.1.4 study establishes the ability of Hesco barriers to contain the explosion of a vehicle bomb. Room A and B doors are blast proof and closed. Blast doors are typically less vulnerable to blasts than the surrounding walls, and it is presumed that intruders lack alternative means to bypass their security. It is assumed that intruders do not have military-grade knowledge of explosives, and more specifically they do not master the skills required to shape charges. Military grade weapons are out of this study.

Physical security response (by the local police for example) is initially overlooked to assess the consequences of an unmitigated scenario. In a latter step, the ability of an intervention team or of an additional physical barrier such as Hesco barriers to mitigate the accident are considered. When required, additional Initial Assumptions (IA) are given for each scenario.

3.1 Defining the Spectrum: Design-Basis versus Beyond Design-Basis Security Considerations

The list of Design-Basis Threats' representative scenarios considered and of Beyond Design-Basis Threats for this study is given in Figure 3.[5] As displayed in Figure 3, only commercial aircraft crashes and contact blasts of magnitude equivalent greater than 150 kg of TNT are considered to lie outside the Design-Basis framework. Without carrying out a full Probabilistic Risk Assessment (PRA), this

[5]It is noted that DBTs and BDBTs analysed in this paper do not correspond to the confidential NRC predefined list. The new proposed list aims at adapting requirements to the relative risk posed by microreactors compared to large light water reactors (LWRs).

section provides quantitative and qualitative arguments supporting the fact that **commercial aircraft crashes** and **contact blasts exceeding 150 kg of TNT** should be considered Beyond Design-Basis.

Commercial aircraft crash In the case where a commercial airplane was to crash against a structure small as a microreactor, no study is needed to predict destruction of the airplane and the microreactor. A more detailed discussion on the likelihood of a commercial aircraft crash is also presented in Section 7.6. Sample reasons are:

- In case of accidental aircraft crash, it is estimated in Section 7 that with current air traffic, the frequency of occurrence of commercial aircraft crash onto a microreactor to $f = 10^{-7}$/yr in the worst case when the plant is located closer than 5 miles from an airport.
- Commercial long-haul aircraft (e.g., A320, A380) are much larger than the SGTR, as seen in Figure 26. A normal strike on the walls of the vault by a hijacked commercial aircraft is physically impossible because the outside diameter of the engine cowling is similar to the height of the wall. An intentional normal strike on the roof of the SGTR may be physically possible but a) has not been proven to be so, to the knowledge of the authors, and b) is so unlikely that the event can be screened out as a beyond-design-basis threat.
- In case of a hijacking whose motivation is to maximise damage and loss of life, a microreactor is not considered a prime target.

Contact blast with magnitude equivalent greater than 150 kg of TNT When considering contact blasts, establishing a precise threshold for what a reactor building should withstand becomes challenging. However, it is imperative to define a limit, as an unbounded amount of explosive force would inevitably lead to the destruction of the target. This study suggests imposing such a limit at an equivalent magnitude of 150 kg of TNT, which aligns with the amount necessary to penetrate 2 meters of reinforced concrete and access Room A, as evaluated in Section 6.2.1.4. Setting specific requirements for contact blast design-basis limits for advanced reactors is the responsibility of regulatory bodies. However, it is important to highlight that current NRC standards, as outlined in 10-CFR-73 [2], are impractical to operate a container-size microreactor.

Consequence evaluation of BDBTs The outlined BDBTs could result in severe damage of the MIT-designed SGTR building and direct mechanical damage to the reactor core, a scenario not accounted for within the DBTs framework. This direct impact on the reactor fuel is expected to trigger a "cliff edge" effect in terms of radioactivity release. The potential full release of the MAR could extend the LPZ and EPZ boundaries to several kilometers. With help of Probabilistic Risk Assessments (PRA) such scenarios will perhaps be eliminated in future guidelines set by the NRC, even though they are considered for existing large reactors.

3.2 Representative Scenarios of Design-Basis Threats (DBTs)

Representative scenarios were selected to have maximum impact within the scope of the assumed Design-Basis limit for each threat category (fire, blast, aircraft crash, sabotage) and main release pathway (fuel, coolant). The initiating events selected as representative scenarios for this design, listed in Figure 3, are the following:

- A large hydrocarbon liquid fire engulfing the reactor, inducing a high level of heat flux to the core,
- A detonation of high explosives at a standoff distance from the reactor of at least 10 m,
- Sabotage of the Reactor Cooling Cavity System (RCCS), by obstructing the air pipes or RCCS air inlet chimneys, leading to a decay heat system failure,
- A contact detonation of 150 kg of TNT, giving the intruders potential access to Room B, where they are free to perform sabotage such as pipe break,
- A leisure aircraft (e.g. Cessna type) or private jet aircraft crash.

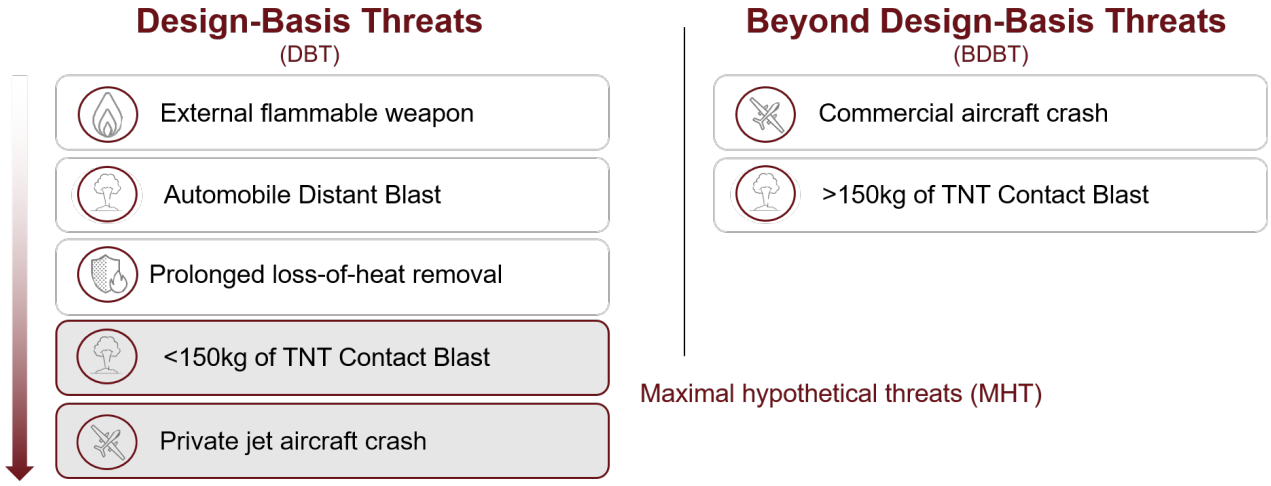

Figure 3: Design-Basis Threats (DBT) and Beyond Design-Basis Threats (BDBT)

The following Sections 4, 5, 6, and 7 evaluate the impacts of representative DBT scenarios including external fire, sabotage, blast, and aircraft crashes, respectively. Section 8 transitions from security to safety considerations and examines wind-borne missiles (schedule 40 pipe and automobile), which naturally extends from aircraft impacts, providing insightful perspectives from a physical security standpoint. Finally, Section 9 assesses accident source term, public dosage, and LPZ and EPZ boundaries associated with representative DBT scenarios, through the modeling of a primary sodium coolant pool fire and a Prolonged Loss-of-Heat-Removal (PLHR).

4
EXTERNAL FIRE THREATS

The postulated fire-related accident scenarios will be further defined and assumptions made for each of them will be described. Physical parameters and stresses associated with each fire scenario will be identified using the Society of Fire Protection Engineers's Handbook (SFPE, 2008) [14] and NUREG-1805, Fire Dynamic Tools [15], as advised in DOE-HDBK-1224-2018, Section 4.2, "Fire Scenario Analysis" [16].

4.1 Scenario initial assumptions (IAs)

In this scenario, intruders pour liquid fuel all over the microreactor's vault and ignite it. In order to consider the worst representative scenario possible, the entire vault surface and surroundings are covered with fuel. The amount of fuel brought by the intruders considered is then the maximal amount that can cause damage at once to the reactor, as additional fuel poured onto the vault would only flow away of the vault area and have minimal impact. The reasoning below assesses that a volume of 640 L and a team effort of 8 intruders are required to cover the area of interest of $222m^2$ in 2 minutes. It is clear that, even if such a large attack seems very unlikely to happen on a microreactor, proving that the reactor can withstand this maximal accident scenario proves that it can withstand any similar scenario of reduced scale. The following assumptions are made :

- The intruders are under time pressure and an intervention team is on its way. Intruders do not have time to build any structure in order to retain the fuel on the vault roof or in trenches surrounding the microreactor walls. The characteristics of the fire studied are thus the ones of an unconfined spill followed by ignition. This type of fire is described in the SFPE Handbook Volume III 3, Chapter 65, "Liquid Fuel Fires". [14]
- Intruders cannot bring vehicles in direct proximity to the reactor. It also means that a car cannot explode in direct proximity of the reactor, explosives in general are not considered in this section which focuses on fire and heat flux impacts.
- Intruders have access to a collection of liquid fuels including gasoline, kerosene, JP-4, JP-5. Most of liquid fuels happen to have similar properties. Conservative results considering the most impactful fuels will be selected.
- The microreactor is in the open air or in a large ventilated warehouse when there is no oxygen shortage. The fire is thus an open fire and the hot gases released are quickly dispersed in the atmosphere.
- As 3-dimensional fires have not been studied in the literature, 3-dimensional effects of the vault are neglected and orders of magnitude of spill depth and burning times are assessed for a spill spreading on a flat horizontal surface. The role played by vertical walls on extending the spill spread is thus neglected. This assumption is conservative, as a more condensed fuel will induce higher heat release rate and burning time.
- The spill is considered static, meaning that the fuel nominally spreads to a given area and then is ignited. Ignition time occurs at $t = 120\ s$. Indeed, 120s are considered to be necessary for the

8 intruders to pour the fuel over the vault. For a fuel volume of 640 L, it corresponds to a fuel flow rate of $Q_{tot} = 5.3\ L.s^{-1}$ or of $Q = 0.66\ L.s^{-1}$ per intruder, which is a reasonable flow rate coming out of a jerrycan. Spreading of the fuel spill after ignition is neglected. This assumption is conservative, as a more condensed fuel will induce higher heat release rate and burning time.

- It is assumed that fire spreads instantly over the whole spill area. In practice, flame spread rate impact the overall burning time for large spill areas. Indeed, with an approximated peak flame spread rate of 10 $cm.s^{-1}$ for liquid phase-controlled flame over the surface of $222m^2$, the fire would take around 2 minutes to spread over the whole spill area, which is potentially longer that the actual burning time. However, assuming that fire spreads instantly over the whole spill area still provides a good order of magnitude of burning time at a given point of the spill.

4.2 Physical analysis of the fire scenario

Unlike a fuel "pool", a fuel "spill" is generally associated with thin fuel layers (lower than 5mm) resulting from an unconfined release of fuel. The nature of a spill fire is highly variable, depending on the source of the release, surface feature of the substrate, and the characteristics of ignition (place, time). Spill fire are described in the SFPE Handbook Volume III, Chapter 65, "Liquid Fuel Fires" [14], that provided values and references used in the reasoning below.

In order to determine the consequences of the spill fire on the vault, two parameters have to be assessed : the fire burning time and the averaged heat flux conveyed to the vault structure. In order to compute these values, spill depth, fuel volume to cover the area of interest, and fuel mass burning rate have to be determined.

Spill depth, covered area and volume of fuel needed The spill spread over an area is based on the initial momentum of the fluid, the fluid surface tension, and the features of the substrate onto which it spilled (porosity and roughness). Experimental results from literature provide a basis for estimating spill depth, depending on substrate and volume spilled. The most recent paper, from Mealy et al. [17], measures spill depth ranges from 0.12 to 2.9 mm depending on the fuel and substrate, but only considers spills up to 20L. Although from an ideal fluid dynamic point of view, there should be no dependence of spill depth on spill quantity, empirical data as well as transient spill models indicate that some dependence exist. The JP-4 spill data of Chambers [18] illustrates this dependency for spills on a concrete runway for spills ranging from 4 to 190L with a corresponding increase in spill depth from 1.1 to 2.9mm. Due to limited experimental data, this data by Chambers provides the best estimate of upper limit fuel depths for large quantity spills at a time of 120s. Based on experimental data, the spill depth is then assumed to be $\delta = 2.9mm$.

The area of interest is the vault surface and its surrounding (up to $\approx 1m$ away for its walls). Knowing the vault dimensions ($5.75m \times 11m \times 4.2m$), this area is around $222m^2$.

Knowing the fuel spill thickness and area of interest, the necessary volume of fuel for the accident is computed :

$$V = A \times \delta = 0.64\ m^3 \approx\ 640L. \tag{10}$$

By considering that intruders cannot bring vehicles in direct proximity to the reactor, that one intruder can only afford two round trips to cars before an intervention team arrives and carry two jerrycans of 20L of liquid fuel at a time, it is estimated that such an attack would require a team effort of 8 intruders.

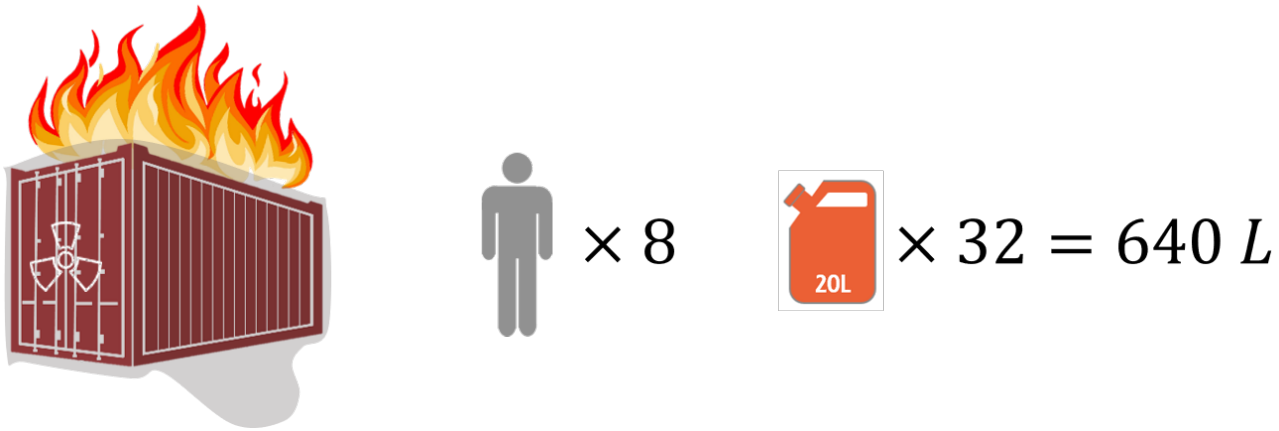

Figure 4: Large hydrocarbon spill fire covering the vault accident scenario

Mass burning rate NUREG-1805, Fire Dynamic Tools (FDTs), Chapter 3, "Estimating burning characteristics of liquid pool fire, heat release rate, burning duration and flame height", Table 3-2 [15] provides values of mass burning rates of multiple petroleum products such as gasoline, kerosene, JP-4 or JP-5. The liquid fuel that has the lowest burning rate that will result in the longest burning time is kerosene with a mass burning rate of $\dot{m}''_\infty = 0.039\ kg.m^{-2}.s^{-1}$.

The burning rate of a pool fires with diameters greater than 0.2 m increases with increasing diameter. Zabetakis and Burgess [19] developed the following relationship to represent the burning rate per unit area as a function of pool diameter, D [m]:

$$\dot{m}'' = \dot{m}''_\infty(1 - e^{-k\beta D}) \tag{11}$$

Where :

- $\dot{m}''$ is the effective mass burning rate of the pool fire $(kg.m^{-2}.s^{-1})$
- $\dot{m}''_\infty$ is the mass burning rate of the pool fire with infinite diameter $(kg.m^{-2}.s^{-1})$
- $k\beta$ is an empirical constant depending on the fuel (for kerosene, $k\beta = 3.5\ m^{-1}$)
- D is the effective diameter area of the pool (m). defined for a non circular pool as $D = (\frac{4A}{\pi})^{1/2} = 16.8\ m$, with $A = 222m^2$ the area of the pool (m^2).

For a large effective diameter, $\dot{m}'' \approx \dot{m}''_\infty$ can be assumed.

Spill fires defined by thin fuel layers ($\delta < 5\ mm$) also have different dynamics than pool fires. A more recent test program conducted by Mealy, Benfer and Gottuk [17] has provided additional insight regarding the burning dynamics of unconfined fuel spills compared to pool fires. A series of tests evaluated the burning dynamics of multiple fuels (gasoline, kerosene, denatured alcohol), at various depths (0.5–20 mm), on multiple substrates (concrete, wood, vinyl, steel, water). Based upon the data collected, correlations were developed for both gasoline and kerosene that can be used to predict the reduction in peak mass burning rate as a function of fuel depth and fuel area. The correlation developed for kerosene is displayes in Equation (12):

$$C_\delta = 0.91 \times (1 - e^{-0.58\delta}) = 0.74 \tag{12}$$

where

- C_δ is the depth coefficient,
- $\delta = 2.9\ mm$ is the spill fuel depth (mm),

The product of this depth correlation with the diameter dependent mass burning rate correlation provides a more accurate prediction of a mass burning rate for a thin fuel layer fire scenario:

$$\dot{m}''(D,\delta) = C_\delta \times (\dot{m}''_\infty(1 - e^{-k\beta D})) \approx C_\delta \times \dot{m}''_\infty = 0.029\ kg.m^{-2}.s^{-1} \tag{13}$$

Burning time In order to assess the thermal threat associated with a fuel spill fire scenario, the peak fire size must be coupled with exposure duration. Most fuel spill fires nominally burn out in less than 1-2 min. Estimating exposure duration can be more precisely accomplished using Equation (14) by assuming that the peak fire size is reached instantly and is maintained as long as the fuel is present. The exposure time associated with this assumption is most likely underestimated but still provides a right order of magnitude.

$$t_b = \frac{4\rho V}{\pi D^2 \dot{m}''_\infty} = 82\ s = 1.4\ min \tag{14}$$

where

- t_b is the burning duration for a given scenario (s),
- $\rho = 820\ kg.m^{-3}$ is the density of kerosene (NUREG-1805 Table 3-2 [15]),
- $V = 0.64\ m^3$ is the volume of fuel,
- $D = 16.8\ m$ the effective spill diameter (m)
- $m'' = 0.029\ kg.m^{-2}.s^{-1}$ is the peak mass burning rate per unit area computed in Equation (13).

Heat flux to target As specified in the SFPE Handbook Volume I, Chapter 34, "Methods for Predicting Temperatures in Fire-Exposed Strcutures", [14], heat is transferred from fire to target by radiation and convection. The contribution of these modes of transfers are independent and must be treated independently. When assuming the surface emissivity and absorptivity equal according to the Kirchhoff's identity, the total heat flux per unit of area $\dot{q}''_t ot$ $(W.m^{-2})$ to a target is :

$$\dot{q}''_{tot} = \dot{q}''_{rad} + \dot{q}''_{conv} \approx \epsilon_s \sigma (T_f^4 - T_s^4) + h(T_f - T_s) = 189\ kW.m^{-2} \tag{15}$$

With

- $\dot{q}''_{rad}$ the net radiation heat flux $(W.m^{-2})$,
- $\dot{q}''_{conv}$ the heat transfer to the surface by convection $(W.m^{-2})$,
- $T_f = 1100\ °C = 1374\ K$ the maximal time-averaged fire temperature for a large pool fire (K),
- T_s the targeted surface temperature (K). For a short fire and with a low thermal conductivity substrate, T_s can be estimated to be equal to atmospheric temperature $T_s \approx 15°C = 288\ K$. In practice, a normal weight concrete surface will reach a temperature of 90% of the fire temperature after 30min.

- ϵ_s the emissivity of the surface, which is a surface property, and can be assumed equal to 0.8 for most building materials such as concrete.
- $\sigma = 5.67 \times 10^{-8}\ W.m^{-2}.K^{-4}$ the Stephan-Boltzmann constant,
- h the convective heat transfer coefficient ($W.m^{-2}$). Its value is not decisive for the temperature development near a fire-exposed surface of a structure as a radiative heat transfer dominates at high temperature. In Eurocode 1 [20], a value of $25W.m^{-2}$ is recommended.

The value provided by Equation (15) is likely overestimated because of the concrete surface temperature considered constant at atmospheric temperature during the time of the fire. Thus, although this value provides a right order of magnitude, it cannot be considered as a time-averaged heat-flux value. The SFPE Handbook Volume III, Chapter 66, "Fire Hazard Calculations for Large, Open Hydrocarbon fires" [14] provides experimental data on temperatures and heat flux conveyed to object immersed in large pool fires. For a wide pool fire, the maximum time-averaged temperatures are generally observed to be approximately 900 - 1100 °C. This maximum has been found to be remarkably independent of the fuel. Based on available data, a maximum time-averaged heat flux to objects fully immersed in optically thick flames of 120 $kW.m^{-2}$ is a reasonable, conservative representation of the available data. McLain [21] and Taylor et al. [22] measured slightly lower heat fluxes ($75-85\ kW.m^{-2}$) in their tests with large items that were similar in size to the pool fire. Indeed, larger calorimeters have an impact on fire temperatures and effectively average the fluxes over the size of the calorimeter, which tends to reduce the measured fluxes.

4.3 Scenario impact assessment

A simulation using the SGTR thermal model developed by Kallieros et al. [11] is used to asses the impact of the spill fire on building temperatures. To simulate the fire, a heat flux boundary value of $120kW.m^{-2}$ is applied for a time of 82s to the vault surface. Results of reactor temperatures are displayed in Figure 5. It is noted that for a burning time in the order of a minute, the spill fire does not affect significantly reactor temperatures apart from the vault's concrete temperature, which increases over the concrete limit temperature for the duration of the fire. Even if the concrete's limit temperature is exceeded for the duration of the fire, studies show that no significant damage is expected to the core. Indeed, the fire resistance of reinforced-concrete is in the order of hours [23].

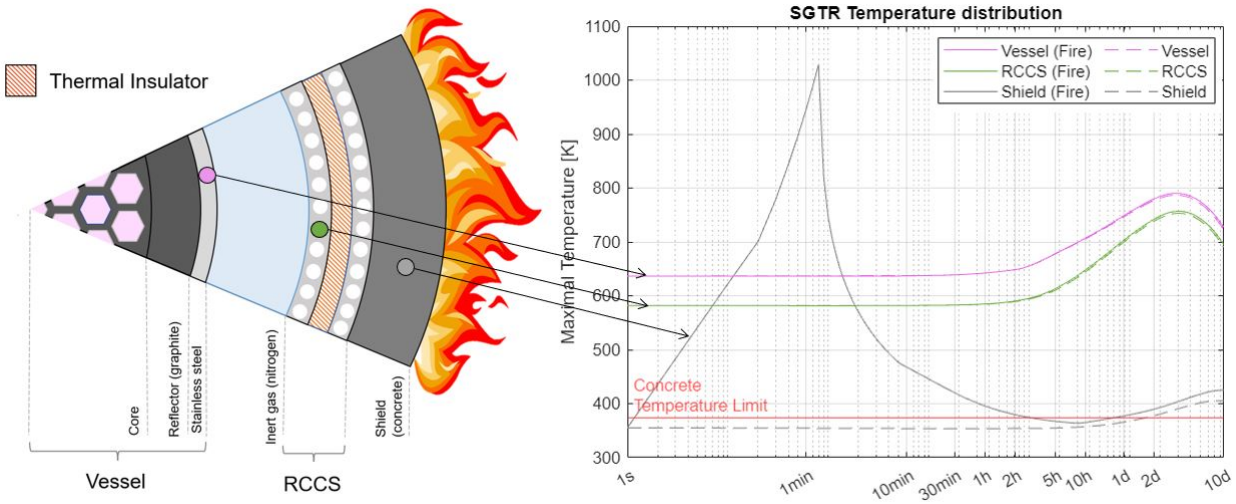

Figure 5: Microreactor temperatures after a 82s spill fire covering the vault

Looking at fuel temperatures after the accident, it is concluded that this accident scenario does not result in a major threat that could lead to radioactivity release. It is deduced that a large heat flux to the core from an external fire is not the main security concern. A small fire scenario disabling the decay heat removal system nominal operations for a significant time period (to the order of the hour) is more likely to have larger consequences than a large fire covering the vault for a few minutes. Indeed, a long-term fire impacting the RCCS system could have ripple effects inducing various failures in the system and increased leak rates, potentially leading to radioactivity release after a significant amount of time. Plausible event sequences have to be more extensively studied in order to assess the impact of such an initiating event.

5
SABOTAGE THREATS

Sabotage poses a significant threat to the safety, security, and stability of nuclear facilities. Defined as the deliberate act of damaging, disrupting, or interfering with operations, infrastructure, or processes, sabotage can have catastrophic consequences within the context of a nuclear power plant. The complexity and potential severity of sabotage actions underscore the critical importance of robust security measures and constant vigilance within these facilities.

Sabotage can take various forms, ranging from physical attacks on critical components to cyber-attacks. A potential sabotage scenario involves the compromise of cybersecurity systems, allowing malicious actors to gain unauthorized access to sensitive information or control systems. Such breaches could enable adversaries to manipulate reactor operations, falsify data, or disrupt communications, undermining the integrity and reliability of nuclear facilities. This threat although not addressed in this report, should be carefully investigated as microreactors will likely be remotely monitored to a great extent.

One common form of physical sabotage involves the intentional manipulation or destruction of vital equipment, such as control systems, valves, or cooling mechanisms, which are essential for maintaining the safe operation. For instance, tampering with coolant systems or disabling emergency shutdown mechanisms could lead to a loss of control over the reactor. The physical attacks utilizing explosives (Section 6), projectiles (Section 8) or ramming by both cars and planes (Section 7) are addressed in other sections. This section aims to provide early insights on obstruction of the emergency cooling mechanism and damaging of pipes. However, it is important to note that this analysis is not exhaustive, focusing instead on key scenarios leading to cooling loss for drawing meaningful conclusions. A more comprehensive investigation would be required to encompass the full spectrum of potential sabotage scenarios and their consequences, but such an exhaustive study is beyond the scope of our current analysis.

5.1 Pipe failure

According to SGTR's layout as given in Figure 1, the only pipes which could be directly accessible to an intruder are the sodium pipes from the secondary loop. If failure in those pipes would result in a potential sodium fire, the secondary loop does not constitute a threat in terms of radioactivity release. This threat is therefore considered to have negligible impacts for the scope of this study.

In this study, pipe failure in the primary loop is considered as a secondary event in case the intruders gain access to Room B following a contact blast of a power equivalent exceeding 2 kg of TNT. The consequences of such a scenario are further studied in Section 9.3.3.

5.2 Obstruction of the Reactor Cavity Cooling System (RCCS) : Prolonged Loss-of-Heat-Removal (PLHR)

5.2.1 • Accident scenario initial assumptions (IAs)

In this scenario, intruders then sabotage the Reactor Cavity Cooling System (RCCS), by obstructing the air pipes or RCCS air inlet chimneys, leading to a decay heat system failure. It is assumed that the intrusion is detected : the reactor shuts down and the sodium coolant is drained from the vessel. In graphs, the Prolonged Loss-of-Heat-Removal is referred to as PLHR.

Discussion was held on whether RCCS failure could be the consequence of a long-term solid fuel (wood, charcoal) or lithium-ion battery fire. This possibility has been ruled out. Indeed, because of low thermal inertia of the air, a constant flow of air is necessary for efficient decay heat removal. If a fire could potentially heat up the air inside the RCCS ducts and thus have the same short term effect of an inlet obstruction, hot gases from the fire would have to be actively pumped into the ducks to expect to cause more damage than an air inlet blockage. A fire being difficult to maintain for a whole month, pipe obstruction was considered as the worst-case scenario in terms of loss-of-heat removal.

5.2.2 • Physical analysis of the scenario

Using the same SGTR thermal model described in Section 4.3, Kallieros et al. [11] were able to determine SGTR's temperature evolutions when the reactor cavity cooling system (RCCS) is disabled. The reactor temperatures, determined up to 90 days, are displayed in Figure 6. The peak temperature of SGTR during a PLHR reaches approximately 1500 K after 40 days. As depicted in Figure 6, increasing temperatures lead to cladding and vessel failures after 12 and 19 days, respectively, if cooling is not restored in the meantime. Such failures result in the subsequent release of fission products into the reactor containment, with partial leakage reaching the environment. A comprehensive examination of cladding and vessel creep, encompassing uncertainties related to creep rate and creep strain to failure, as well as containment leakage is provided in Sections 9.4.7 and 9.4.8 as part of the accident scenario Mechanistic Source Term (MST) assessment.

5.3 Mitigation strategies against sabotage threats

This section is not a comprehensive list of all the possible threats which could fall under the term sabotage, but aims to provide the reader with considerations to take into account while designing mitigation strategies.

One strategy common to all physical and cyber threats is to detect the attack and delay it. Due to either no or few physical security personnel on site of a microreactor, delaying the attack is all the more crucial to give time to local law enforcement to intervene. In addition, delaying is also of paramount importance to give time for counter measures to be taken and completed. Those counter measures consist in putting the reactor in a state that minimizes its vulnerability, or the consequences in case of a successful attack. They could be for example shutting down the reactor, draining the activated coolant, etc. The detection should be as early as possible to give as much time to both counter measures and law enforcement.

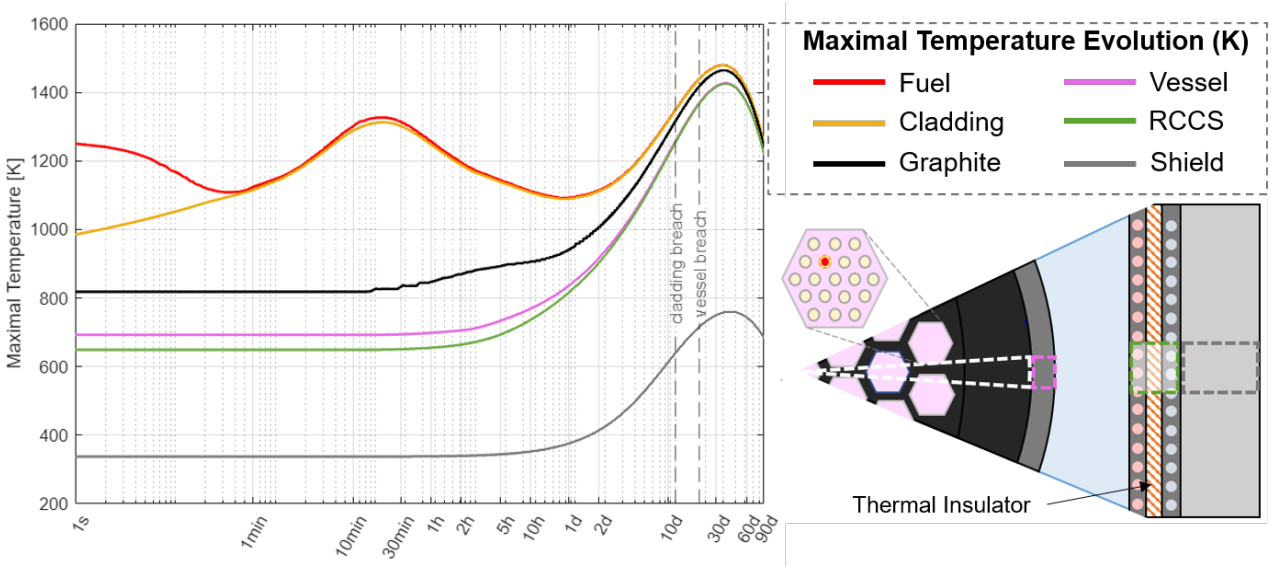

Figure 6: SGTR PLHR Temperature Evolution

Microreactor designs play a crucial role in mitigating threats, either by both making certain attacks impossible (or extremely difficult), or by delaying the intruders. A first example of mitigating design is a great thickness of reinforced concrete (RC), which prevents collapse or perforation by reasonable amounts of explosives, prevents ramming, or delays intruders by forcing them to rely on time consuming strategies. Another important feature is the design of the RCCS outlet, which should hinder its obstruction, and also prevent the introduction of an explosive device inside. Finally, a physical barrier in the form of fences or Hesco barriers delimiting the Exclusion Zone could serve a triple purpose: preventing or delaying the trespassing of both intruders or civilians, hindering ramming attacks and absorbing the shock wave generated by high explosives. Mitigation strategies against blasts and aircraft impacts are elaborated on in the specific sections.

6
BLAST THREATS

6.1 Distant blasts

6.1.1 • Introduction to blasts and scope of assessment

The detonation of explosives could damage microreactors. An assessment of the consequences of different types of blasts must be conducted, both to develop mitigation features and to evaluate the release of radioactivity in the context of the consequence-based analysis.

The effects of a blast on a structure are characterized by the "standoff" distance R between the target and the detonation location, and the equivalent mass of TNT of the explosive charge W. The scaled distance $Z = R/W^{1/3}$ enables a comparison between different types of blasts. If two blasts have the same scaled distance, they will have the same effects on the targeted structure. The lower the scaled distance, the greater the loading on the target. The scaled distance is also a criterion to distinguish between the different types of blast, which are [24]:

- Contact blast: $Z < 0.4$ m/kg$^{1/3}$
- Near field blast: $0.4 < Z < 1.5$ m/kg$^{1/3}$
- Distant blast: $Z > 1.5$ m/kg$^{1/3}$

Figure 7 illustrates the scenarios considered in this study: (a) detonation of a contact charge positioned at mid-height on the external surface of a wall, (b) detonation of 20kg of TNT (a backpack weapon) at mid-height and 10m from the vault, corresponding to $Z = 3.7$ m/kg$^{1/3}$, and (c) detonation of 450kg of TNT (a vehicule weapon) 10m away from the vault, corresponding to $Z = 1.3$ m/kg$^{1/3}$.

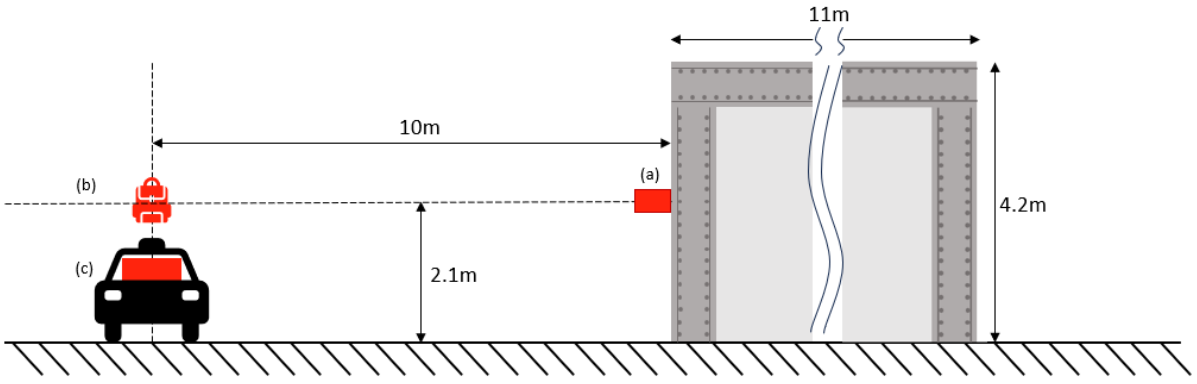

Figure 7: Representation of the three blasts

In the safety report from IAEA [24], the effects of those different blasts are described as follows: "*In the case of a distant blast, the main loading effect is the overpressure caused by the incoming pressure wave, increased by wave reflection.*" "*In the case of structures subjected to a near field or a contact*

blast, the shock wave originating from the detonation travels directly through the solid construction material causing a sharp increase in pressure, and loading conditions are very different to the loads of a distant blast.".

For the calculations that follow, it is assumed that intruders do not have physical access to the vault. The detonation occurs at a distance from the vault so that the detonation is a distant blast. The vault walls are designed to resist this threat. Subsequently, it is assumed that an intruder can place an explosive charge directly on a wall of the vault: a contact blast.

This section provides a calculation of the wall thickness required to prevent the formation of substantial cracks due to an air-blast occurring at a standoff distance R with an explosive of mass W. The situation is described in Figure 8.

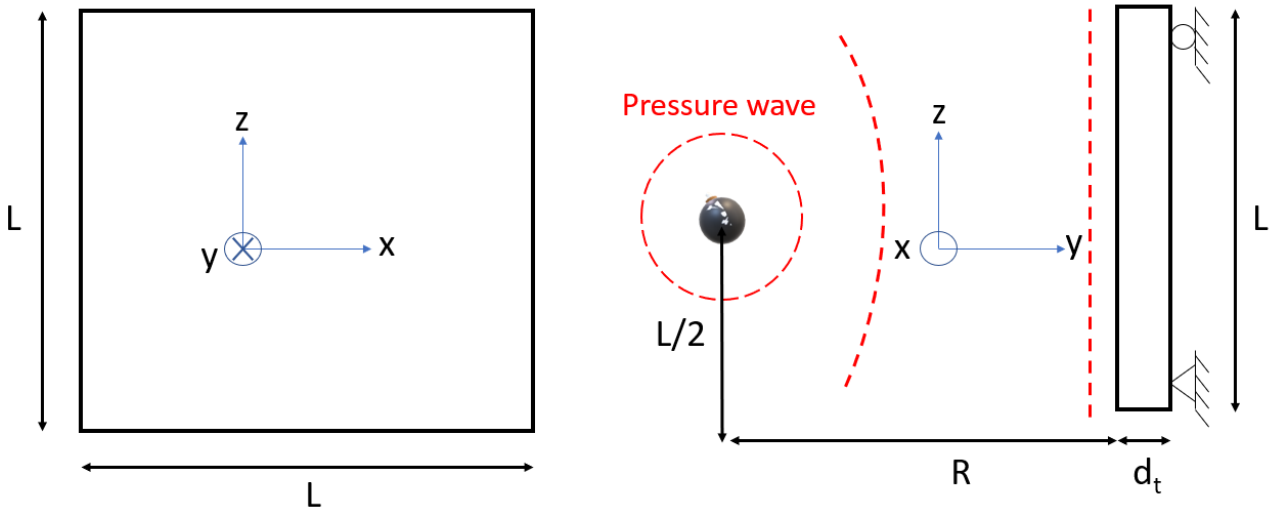

Figure 8: Air-blast model

6.1.2 • Single Degree of Freedom Model

A Single Degree Of Freedom (SDOF) model such as that proposed by Biggs [25], can be used to estimate a trial thickness of a reinforced concrete wall.

The wall analyzed here is square in elevation with a side length $L = 4.2m = 13.8ft$. The wall is pinned at its top and bottom, and the vertical edges are free to deflect. Gravity loads are ignored for this calculation. The total thickness d_t is to be determined. The explosive charge is detonated opposite the center of the wall, $L/2 = 2.1$m above the ground. The wall is reinforced with grade 60 rebar, with yield strength $f_y = 60,000psi = 414$MPa. For the concrete, uniaxial compressive strength $f'_c = 5,000psi = 34$MPa, Young's modulus $E = 4 \times 10^6 psi = 6895$MPa and density $\rho_c = 150lb/ft^3 = 2403$kg/m^3.

6.1.2.1 Loading

The air-blast creates a pressure wave that propagates until it reaches the surface of the wall. The loading on the wall is due to the reflection of the pressure wave. We assume for this hand calculation that the overpressure (i.e. pressure above ambient) generated by the blast on the wall is uniform across the face at a given time step. Only the positive phase of the loading is considered. Under these conditions the overpressure time history can be simplified to that shown in Figure 9, where p_r is the maximum reflected overpressure and the area under the pressure-time curve is the reflected impulse:

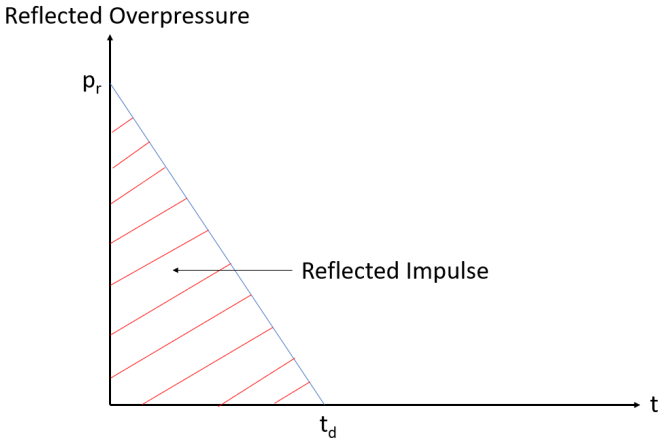

Figure 9: Simplified reflected overpressure loading.

In this approximation, the maximum reflected overpressure p_r and the duration t_d of the positive phase fully characterize the load. Blasts can be characterized by their scaled distance $Z = R/W^{1/3}$ [26]. For $R = 10m$ and $W = 20kg$, $Z = 3.7m/kg^{1/3}$. The time t_d is back-calculated from p_r and I_r, calculated here using Figure 2-7 of [26]: $p = 0.11$MPa $\approx$ 16psi and $I_r/W^{0.33} = 0.1$MPa.ms/kg$^{0.33}$, where I_r is the scaled unit positive normal reflected impulse, and for $W = 20$kg, $I_r = 0.27$MPa.ms. The corresponding positive phase duration is $t_d = 2I_r/p = 4.9ms$.

6.1.2.2 Structural response to the load

To limit damage and maintain leak tightness (i.e. no significant cracking), the maximum blast-induced displacement of the wall y_m, has to remain below the maximum elastic (i.e. yield) displacement y_e. We define a ductility ratio $\mu = y_m/y_e$. With this definition, the "no significant cracks" criterion is $\mu < 1$, where μ is limited here to 0.6 to provide a margin.

As explained in [25], many structures can be idealized and modeled as single-degree-of-freedom systems. Herein, the interaction between the load and the wall is described by an undamped harmonic oscillator:

$$M_e \frac{d^2y}{dt^2} + k_e y = F_1 f(t) \tag{16}$$

where M_e is the equivalent mass of the system, y is the displacement, k_e is the equivalent spring stiffness, F_1 is the maximum load and $f(t)$ is the load-time amplitude. The spring-mass system is selected

such that the deflection of the mass is the same as at some point of significance on the structure, for example, the center of the wall. The constants of the equivalent system are evaluated on the basis of the assumed displaced shape of the actual structure. This shape will be taken to be the same as that resulting from the static application of the dynamic loads. See [25] for details.

The natural period of response of the actual structure is defined as $T = 2\pi\sqrt{\frac{K_{LM}M_t}{k}}$, where M_t is the total mass of the system, k is the real stiffness, and K_{LM} is a transformation factor accounting for the deflected shape, whose value is discussed later.

The maximum response of elasto-plastic one-degree systems (undamped) due to a triangular load is presented in Figure 10:

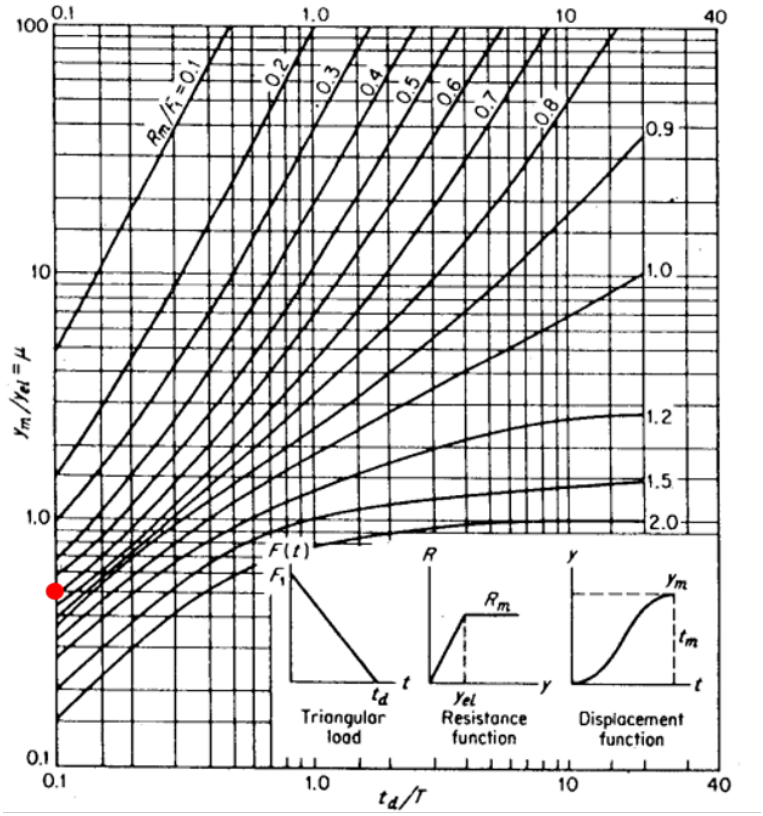

Figure 10: Maximum response of an elasto-plastic, undamped SDOF due to a triangular load pulse. [25]

In this figure, R_m is the maximum resistance, presented in the same units as the peak load F_1; all other terms were defined previously.

The process of evaluating the minimum thickness is trial-and-error. A trial thickness is $d_t = 12in$ (30cm), and a unit width of wall, $w = 1ft$ (30cm), is assumed for analysis. The moment of inertia around the x axis as shown in Figure 8 for a rectangular section is computed as follows:

$$I = \frac{wd_t^3}{12} = \frac{12\text{in} \times (12\text{in})^3}{12} = 1728 \text{ in}^4 \tag{17}$$

The uncracked stiffness of the strip is then given by the following equation extracted from [25]:

$$k = \frac{384EI}{5L^3} = \frac{384 \times 4 \times 10^6 \times 1728}{5 \times (12 \times 13.8)^3} = 118,000 \text{ lb/in} \tag{18}$$

Minor cracking is inevitable, and based on engineering judgment:

$$k_{cr} = 0.4k = 47,000 \text{ lb/in} \tag{19}$$

The total mass of the strip is:

$$M_t = \rho_c d_t L w g^{-1} = 150 \times 1 \times 13.8 \times 1 \times 1/386 = 5.3 \text{ lb.s}^2\text{/in} \tag{20}$$

The transformation factor, $K_{LM} = 0.78$ from Table 5-1 of [25], which corresponds to the deformation of the slab close to but below its elastic limit. Accordingly,

$$T = 2\pi\sqrt{\frac{K_{LM}M_t}{k_{cr}}} = 2\pi\sqrt{\frac{0.78 \times 5.3}{47,000}} = 0.059s \tag{21}$$

Using this natural period $t_d/T = 4.9\text{ms}/59\text{ms} \approx 0.1$, where t_d was calculated in Section 6.1.2.1. Using $\mu = 0.6$, Figure 10 gives $R_m/F_1 = 0.5$, shown by the solid red circle in Figure 10. Since F_1 is the force created by the maximum reflected overpressure $p_r = 16psi$ (as defined in figure 9), the required maximum resistance is:

$$R_m = 0.5 \times p_r = 8psi = 1,150 \text{ lb/ft}^2 \tag{22}$$

The required bending moment resistance M for 1-foot width of simply supported wall is:

$$M = \frac{R_m L^2}{8} = \frac{1,150 \times 13.8^2}{8} = 27,375 \text{ lb-ft/ft width} = 328,500 \text{ lb-in/ft width} \tag{23}$$

The bending resistance of a 1-foot wide reinforced concrete wall is M_n:

$$M_n = 0.95A_s f_y^* d \tag{24}$$

where A_s is the area of reinforcement, $f_y^* = 1.2f_y$ is the expected yield strength of the steel reinforcement, d is the effective depth of the reinforcement from the compression face of the wall and which can be set equal to the total thickness d_t minus 2 inches for these calculations. For $M_n > M$:

$$A_s > \frac{M_p}{0.95f_y^* d} = \frac{328,500}{0.95 \times (1.2 \times 60,000) \times 10} = 0.48 \text{ in}^2\text{/foot width} \tag{25}$$

Number 6 (#6) reinforcing bars at 12 inches on center gives 0.44in^2/foot width (9.3cm^2/m width), and this reinforcement is assumed for the numerical simulations. For ease of construction, #6 bars are used on each face of the wall, in the vertical and horizontal directions.

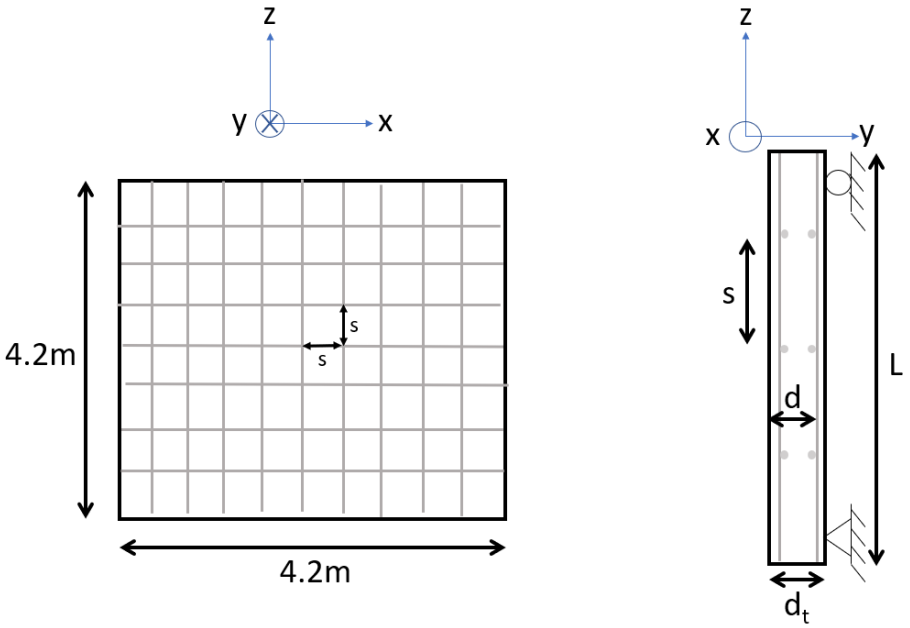

Figure 11: Sketch of the steel reinforcement (gray) in the wall. Not to scale

6.1.2.3 Conclusions of the hand calculations

If 10m away from a 20kg TNT free-air burst, a wall thickness of 12in= 30cm (associated with a reinforcement as specified in the previous section), concrete strength of 5000psi= 34MPa, #6 grade 60 rebar at s = 12in= 30cm (see Figure 11) on center on each face, should prevent the formation of significant cracks. This thickness to prevent substantial cracks is valid not only for this [standoff distance, explosive mass] pair, but for every pair such that $Z \geq 4$ m/kg$^{1/3}$.

6.1.3 • Verification of the blast wall design using ABAQUS CAE

The wall design presented in Section 6.1.2.3 is verified using ABAQUS CAE [27], a finite element code by *Dassault Systèmes*. This software includes CONWEP library, which is a collection of blast-load curves that can be directly applied to a surface.

6.1.3.1 ABAQUS model of the wall and detonation

The reinforced concrete wall is modeled as a layered shell, with external concrete layers separated from the internal concrete layer by steel plates (reinforcement) as shown in Figure 12.

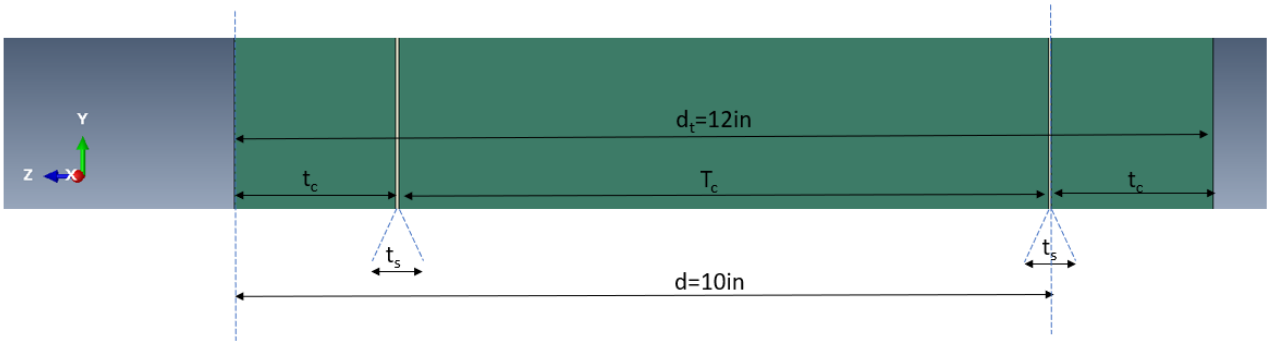

Figure 12: Wall model: concrete layers in green, steel plates in white.

To simulate the structural response of the reinforced concrete wall, the following are assumed:

- Reinforcement ratio $\rho = \frac{A_s}{wd} = \frac{0.44in^2}{12in \times 10in} = 0.365\%$ **for each face**
- Total thickness of wall $d_t = 12in$
- Effective depth of reinforcement $d = 10in$.

The definition of these quantities gives the following set of equations:

$$\begin{cases} 2t_c + 2t_s + T_c = d_t \\ t_c + t_s + T_c + \frac{t_s}{2} = d \\ \rho = \frac{t_s}{d} \end{cases} \tag{26}$$

Therefore:

$$\begin{cases} t_s = 0.0365in = 0.09271cm \\ t_c = 1.98175in = 5.03365cm \\ T_c = 7.9635in = 20.2273cm \end{cases} \tag{27}$$

Each layer is modeled as a shell element with a thickness as determined in Equation (27). The interaction between the different layers is a cascade of "Tie" interactions, meaning that the displacement of the different surfaces are constrained to a master surface displacement in the pattern described in Figure 13:

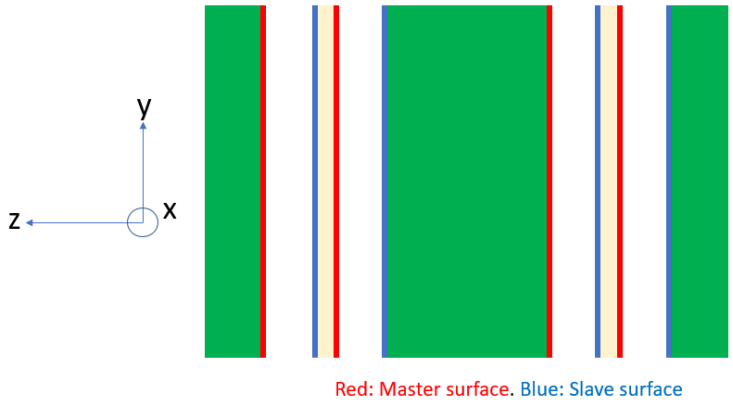

Figure 13: Cascade scheme of tie constraints

As regards boundary conditions, the top edge of the front external layer is restrained along the z axis, whereas for the bottom edge all translation degrees are restrained. The detonation occurs 10m from the center of the front external layer. The ABAQUS explicit solver is used with the non-linear geometry option activated. The detonation of 20kg TNT occurs at $t = 0$ and the simulation lasts for 0.2s. Data is saved every 0.5ms.

Material models The concrete material model used is Concrete Damage Plasticity (CDP) implemented in ABAQUS. The equations governing this model as well as the physical meaning of the different parameters are reported in [28]. The elasticity and plasticity parameters are chosen to represent the behavior of B40 grade concrete and given in Table 11, extracted from [28].

The Johnson-Cook plasticity model is used for the reinforcement, as described in [29]. The values implemented in ABAQUS are given in Table 12 extracted from [29]. These values correspond to AISI 1006 steel, with properties similar to ASTM A992 (Grade 50).

Material's parameters	B40	Plasticity parameters	
		Dilation angle	31
Concrete elasticity		Eccentricity	0.1
E (GPa)	30	fb0/fc0	1.16
	0.2	K	0.67
		Viscosity parameter	0
Concrete compressive behavior		Concrete compression damage	
Yield stress (MPa)	Inelastic strain	Damage parameter C	Inelastic strain
20.4	0	0	0
25.6	2.66667E-05	0	2.66667E-05
30	0.00008	0	0.00008
33.6	0.00016	0	0.00016
36.4	0.000266667	0	0.000266667
38.4	0.0004	0	0.0004
39.6	0.00056	0	0.00056
40	0.000746667	0	0.000746667
39.6	0.00096	0.01	0.00096
38.4	0.0012	0.04	0.0012
36.4	0.001466667	0.09	0.001466667
33.6	0.00176	0.16	0.00176
30	0.00208	0.25	0.00208
25.6	0.002426667	0.36	0.002426667
20.4	0.0028	0.49	0.0028
14.4	0.0032	0.64	0.0032
7.6	0.003626667	0.81	0.003626667
Concrete tensile behavior		Concrete tension damage	
Yield stress (MPa)	Cracking strain	Damage parameter T	Cracking strain
4	0	0	0
0.04	0.001333333	0.99	0.001333333

Table 11: CDP values implemented in the ABAQUS model [28]

Table 12: Values of parameters in the J-C model in ABAQUS

Parameter	A [MPa]	B [MPa]	n	m	Melting Temp. [°C]	Transition Temp. [°C]
Value	350	275	0.36	1	1811	300

6.1.3.2 Simulated overpressure and displacement history

In this section, the results of the simulation are reported and compared to the expected values yielded by the SDOF calculations. The overpressure history being applied to the wall by the CONWEP module is shown in Figure 14. The detonation occurs at $t = 0$s, 10m from the face of the wall where the pressure history is measured. The arrival time of the wave is 15ms with a maximum pressure of 0.13MPa. The pressure then drops to zero in 8ms. The difference in the durations of the positive phase for the idealized and the simulated loads is due to the different shapes. The shape of

the CONWEP wave is close to the overpressure profile assumed for the hand-calculation.

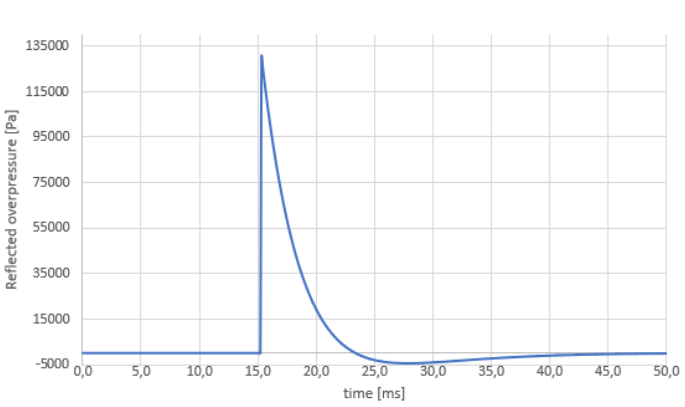

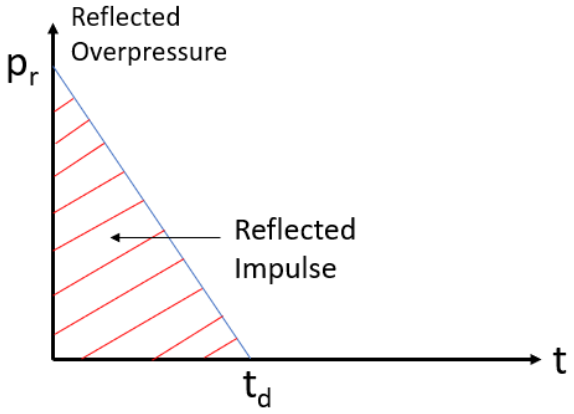

	Hand calculation	Simulation
Maximum overpressure [MPa]	0.11	0.13
Reflected impulse [MPa-ms]	0.271	0.320
Duration positive phase [ms]	4.9	8.00
Arrival time [ms]	16	15

Figure 14: CONWEP (simulated) and triangular (hand calculation) reflected overpressure profiles

The displacement along the z axis at the center of the front face of the wall is displayed in Figure 15. There is an alternating between negative and positive deflection, in an harmonic shape characterized by a period of 38ms. The maximum displacement is 2.8mm in absolute value during the first negative peak. Images from the simulation with an amplifying factor of 100 are shown in Figure 16. The contouring represents $U3$ displacement, which is the displacement along the z axis.

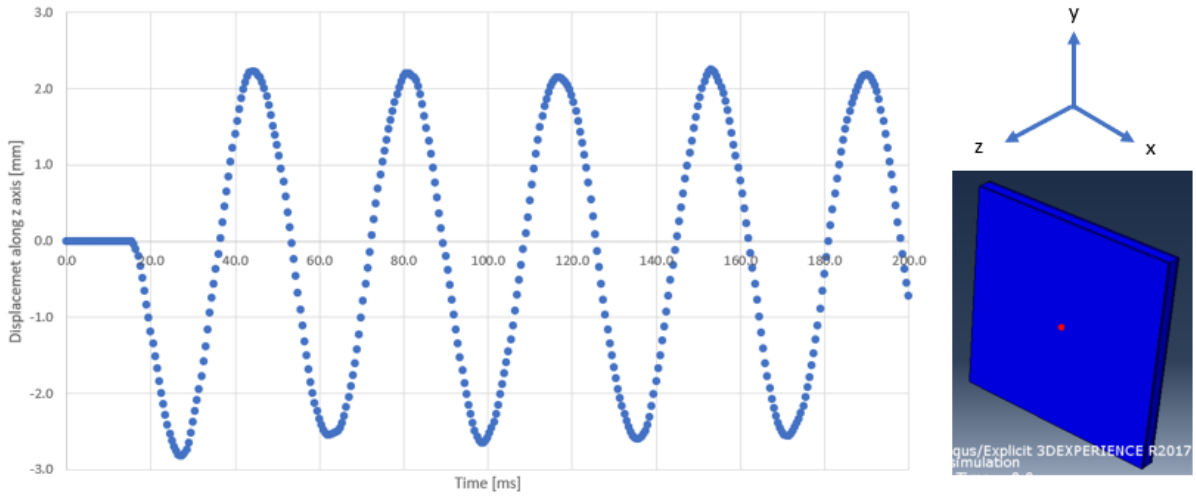

Figure 15: Simulated displacement history, z axis, center of front face

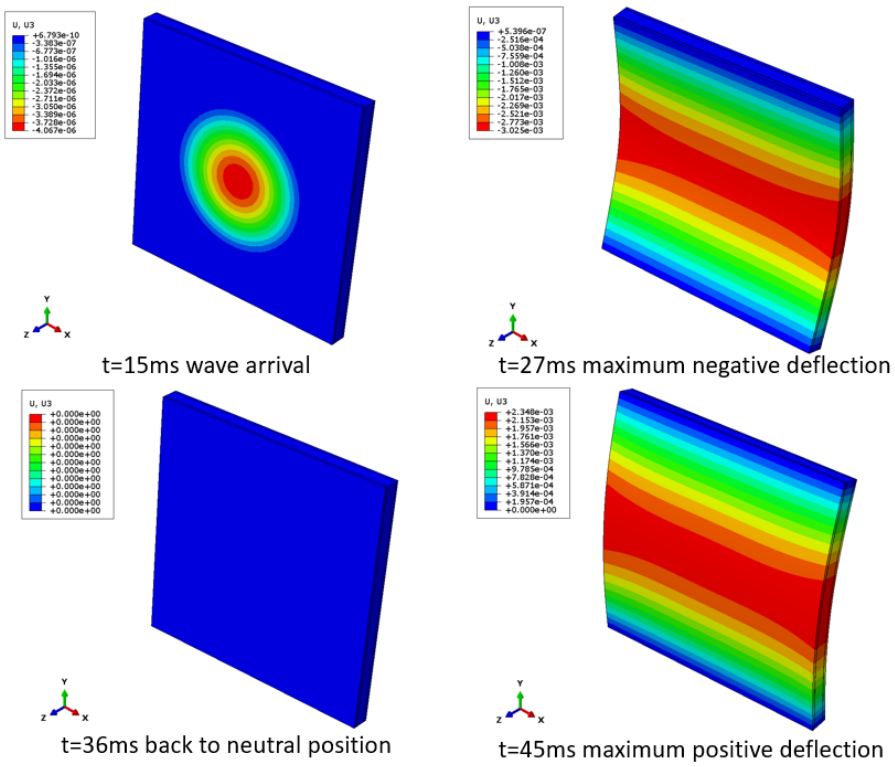

Figure 16: Deflection of the wall along the z axis at different times ($\times$100 exaggerated)

6.1.3.3 Comparison with the expected values from the SDOF model

To compare the results of the hand calculations and the ABAQUS simulation, the expected maximum displacement and natural period response need to computed for the thickness and type of reinforcement described in the previous sections. The maximum resistance R_m of the wall is:

$$A_s = 0.44 \text{ in}^2/\text{ft width} \therefore M_{max} = 0.95 A_s f_y^* d = 301,000 \text{ lb-in/ft width } = 25,080 \text{ lb-ft/ft width} \tag{28}$$

$$\text{Moreover } M_{max} = \frac{R_m L^2}{8} \therefore R_m = 1393 \text{ lb/ft}^2 \tag{29}$$

$$y_e = \frac{R_m L}{k} = 0.17 \text{ in} = 3.6 \text{ mm} \tag{30}$$

$$\text{For } \mu = \frac{y_{max}}{y_e} = 0.6 \therefore y_{max} = 2.2mm \tag{31}$$

$$T = 2\pi\sqrt{\frac{K_{LM} M_t}{k}} = 2\pi\sqrt{\frac{0.78 \times 5.3}{118,000}} = 0.037s \tag{32}$$

These results are in very close agreement with the simulated results: $T = 38ms$ and $y_{max} = 2.8mm$ which gives credibility to both the SDOF model and the ABAQUS model.

6.1.4 • Explosion outside the Hesco barriers perimeter

Hesco barriers, renowned for their cost-effectiveness alongside their efficacy in blast mitigation, provide a versatile solution for safeguarding assets against explosive threats. Deploying Hesco barriers around an asset involves strategically placing these modular units filled with sand, gravel, or other suitable materials to form a protective perimeter. Their design, comprising welded mesh walls lined with heavy-duty fabric, offers exceptional resistance against blast pressures by effectively dissipating and redirecting the force of the explosion. Moreover, their collapsible nature facilitates easy transportation and rapid deployment. By establishing a buffer zone between the asset and potential blast sources, Hesco barriers serve as a formidable barrier, minimizing the impact of blasts and safeguarding critical infrastructure and personnel. With their economical nature and low maintenance requirements, Hesco barriers could emerge as a solution fit for MMRs. A picture of deployed Hesco barriers is provided in Figure 17.

Figure 17: Hesco barriers [30]

6.1.5 • Vehicle weapon sufficient to collapse Room B

In this section, calculations are performed to estimate the size of a vehicle weapon needed to badly damage the wall of Room B, assuming it is detonated 10m from the wall and no Hesco barriers are deployed. The thickness of this wall is taken to be 1ft= 30cm.

Collapse criterion One criterion for collapse is a maximum deflection y_{max} at the mid-height of the wall equal to 2.5% of its height (or a support rotation of 0.05rad). For the 4.2m high wall:

$$y_{max} = 0.025 \times 4.2 = 10.5cm \tag{33}$$

A parameter to identify material failure (cracks) is the tensile damage parameter. Indeed concrete most of the time fails because of loads in tension, since its tensile strength is usually 10 times smaller than its compressive strength. Compressive and tensile damage correspond to a loss of stiffness and resistance. Both are calculated using the following equations:

$$\begin{cases} \Delta = 0 \text{ if } \epsilon < \epsilon_s \\ \Delta = 1 - \frac{\sigma}{\sigma_s} \text{ if } \epsilon > \epsilon_s \end{cases} \tag{34}$$

where Δ is the damage parameter, ϵ is the strain, σ is the stress and ϵ_s is the strain associated with the maximum tensile strength σ_s. Damage is irreversible. Once an element is strained beyond its tensile (or compressive) strength (red line in Figure 18), damage occurs, and the damage value can only increase from this point. If an element has tensile damage above 0.9, it is assumed here to have failed. Figure 18 shows the stress-strain curves in tension and compression, and the damage curves for the implemented concrete material model.

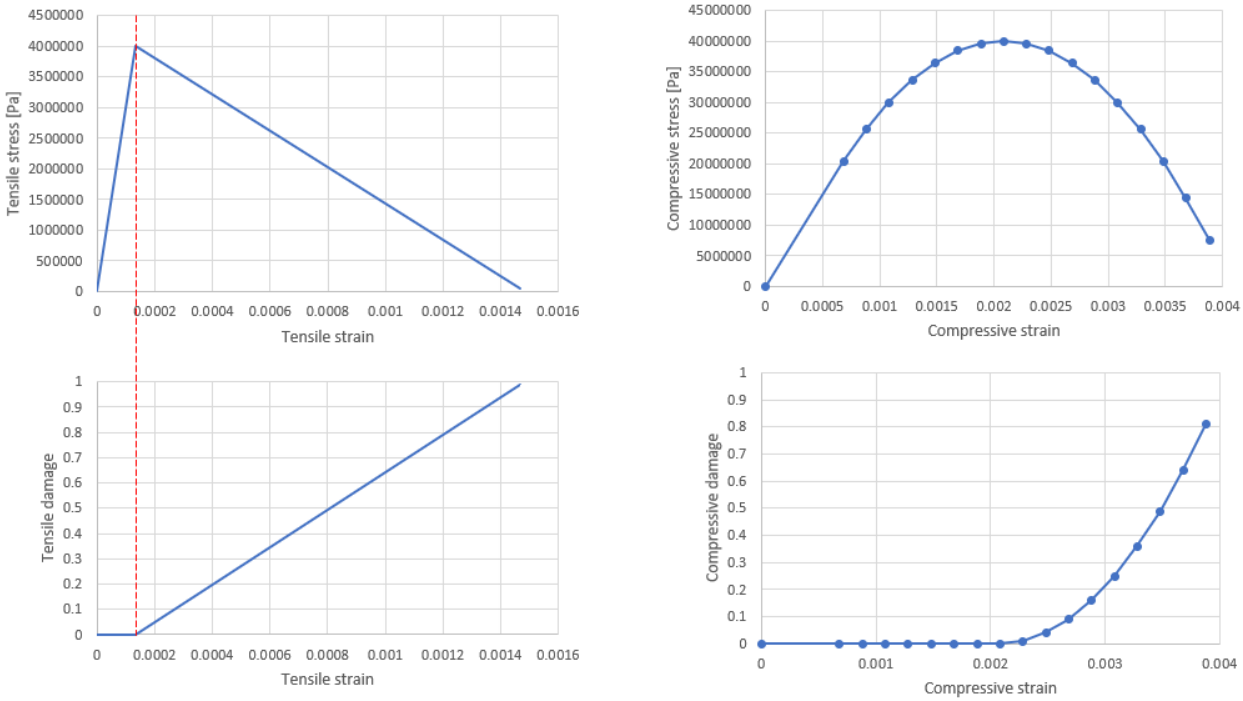

Figure 18: Left: tension curves. Right: compressive curves. Top: Stress-strain curves. Bottom: Damage curves

To determine the mass of explosive required to damage Room B wall for a standoff distance of 10m, ABAQUS simulations were performed using the model described in Section 6.1.3.1. For 450kg of TNT, the maximum wall displacement is 11cm, which is approximately the displacement yielded by Equation (33). This mass of explosive corresponds to a vehicle (Sedan automobile) weapon per [31]. The tensile damage reaches 99% on most of the front and back surface of the wall, and in the core region. These results are displayed in Figure 19, taken 0.1s after detonation. Element deletion was not activated.

The scaled distance of such a blast is $Z = \frac{10m}{(450kg)^{1/3}} = 1.3\text{m/kg}^{1/3}$, which qualifies as near-field. Because this value is close to the limit separating distant and near-field, heat is assumed to play no

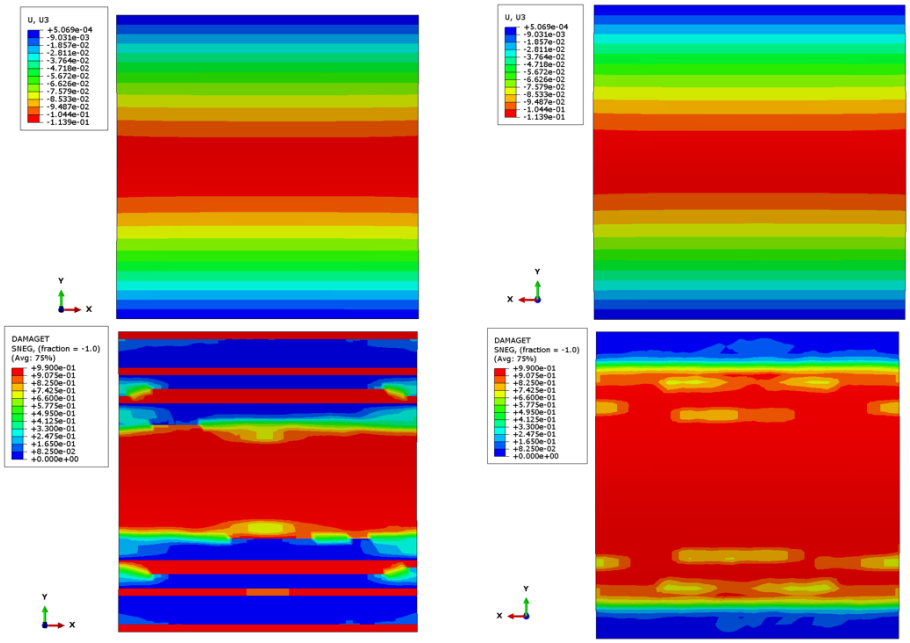

Figure 19: Structural effects of the detonation of 450kg of explosives 10m from the vault. Left: Front face. Right: Back face. Top: Displacement in $U3 = z$ direction [m]. Bottom: Tensile damage

role in the structural response of the RC wall.

The conclusion drawn here is that a large vehicle weapon (450kg TNT) could badly damage a 1ft-thick RC wall if detonated 10m from it. Depending on how the internal steel liner is attached to the inside face of the wall, it could serve to reduce the damage and prevent the ingress of scabbed concrete and overpressure into Room B.

6.1.6 • Other ABAQUS simulations

ABAQUS simulations were run for both a 30cm-thick and a 50cm-thick wall. The length of the wall was also increased from 4.2m to 11m to address a blast striking the long walls of the vault. The length of wall had no significant impact on the required amount of TNT to damage the wall. Using a standoff distance of $10m$, simulations were executed to identify the mass of TNT required to:

- Crack a 30cm-thick wall
- Badly damage a 30cm-thick wall
- Crack a 50cm-thick wall
- Badly damage a 50cm-thick wall

The corresponding scaled distances, shown in Figure 21, were then used to estimate the required mass of TNT at standoff distances, up to 20m.

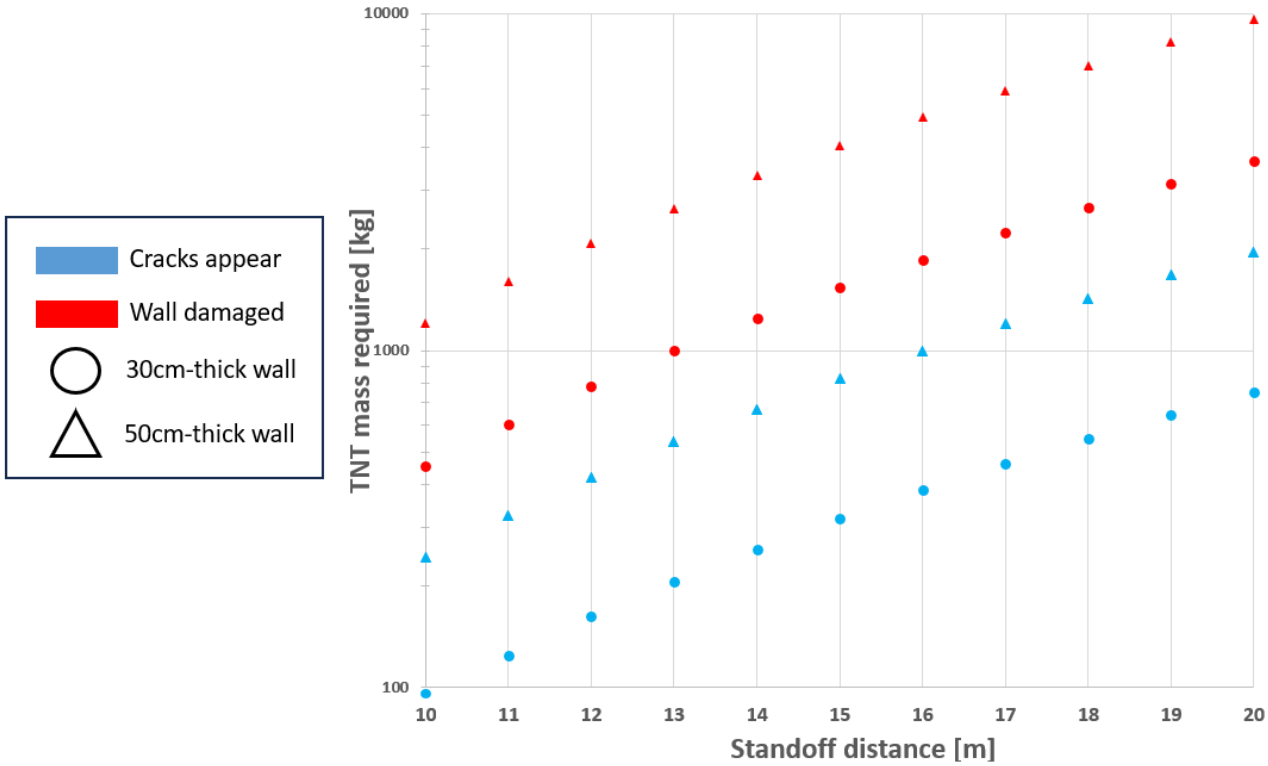

Figure 20: Required mass of TNT to crack and damage an RC wall, as a function of standoff distance and wall thickness.

Figure 20 identifies two mitigation strategies for distant blasts: increasing the wall thickness, or imposing a larger standoff distance. Noting that the y-axis is in log scale, the most efficient mitigation strategy is increasing standoff, which can be easily achieved with routine protective measures. Important results for distant blasts are displayed in the form of a flowchart in Figure 21. The assumptions made are:

- The vault is above ground.
- The RCCS coolant is air, meaning that the heat removal system of the reactor is not compromised by the distant blast (unlike a water RCCS system whose water tank could by pierced and lose its fluid).
- The steel liner is attached to the inside face of the RC wall, meaning that scabbing of concrete does not necessarily damage equipment.
- The standoff distance is 10m.
- Room B wall thickness is either 30cm (colored in blue) or 50cm.
- Room A wall thickness is 2m, which is the thickness of the radiation shield. Therefore only small damage (in the form of small cracks) is possible with any plausible amount of TNT, and no damage is caused to the core.

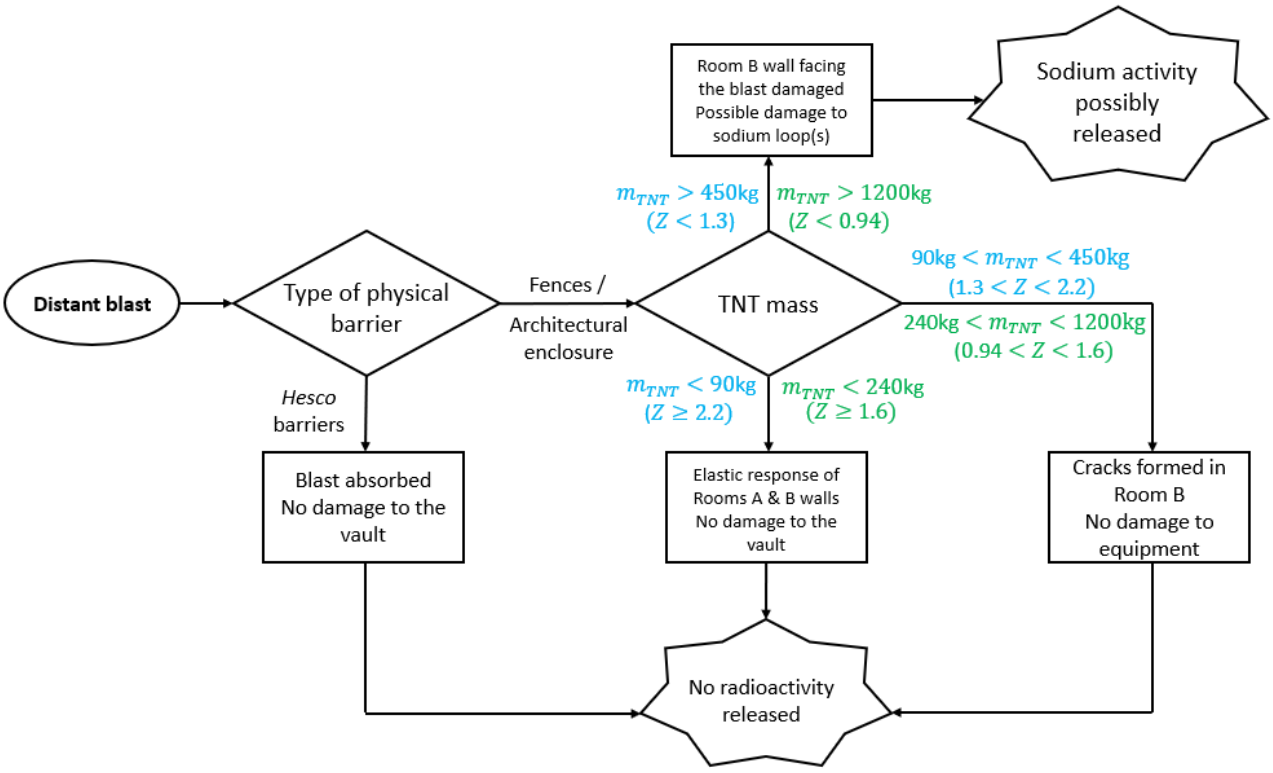

Figure 21: Summary flowchart for distant blasts

6.2 Contact blasts

If intruders penetrate the protected perimeter and gain access to the perimeter of the vault, an explosive charge could be placed on a wall. This section provides a methodology to assess the effects of a contact blast, and applies it to the reinforced concrete (RC) vault walls described in the previous sections, and to a 1cm-thick steel plate wall.

6.2.1 • Required amount of explosive to breach a RC wall

6.2.1.1 Breaching charge

The goal of this section is to estimate the required mass of TNT to breach a RC wall. The equations and empirical factor values are taken from [32]. A breach is defined as a perforation through the thickness of the wall. The required explosive mass (TNT-equivalent) to breach a RC wall, P_b, is:

$$P_b = 16 \times d_t^3 KC \tag{35}$$

where P_b is in [kg], d_t is the wall thickness in [m], K is the material factor and C is the tamping factor (depends on the position and whether the explosive is confined), and 16 is an aggregated conversion factor from [lbs] to [kg] and [ft] to [m] since the original formula is in imperial units. For RC, the material factor is a function of the wall thickness as given in Table 13. A breach occurs when the explosive mass employed $P > P_b$.

Table 13: Values of K as a function of wall thickness

Thickness d_t	d_t<0.3m	0.3m<d_t<0.9m	0.9m<d_t<1.5m	1.5m<d_t<2.1m	d_t>2.1m
K	1.76	0.96	0.80	0.63	0.54

Tamping serves to direct as much of the explosive energy as possible to the target. Here the explosive is assumed to be untamped since the intruders will not have much time before police intervention and the explosive is placed above the ground surface. In these conditions, Figure 22, which is extracted from [32], yields $C = 1.8$.

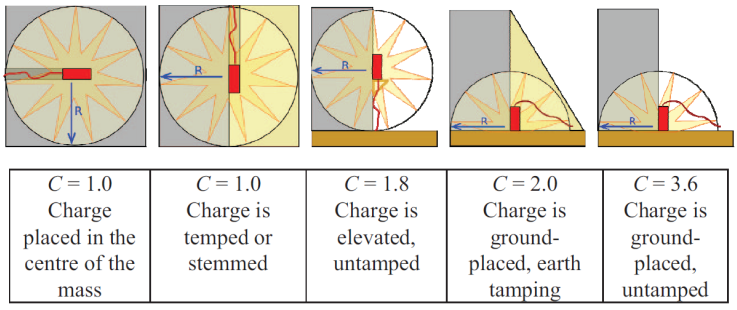

Figure 22: Tamping factor C for breaching charges

6.2.1.2 Breach shape and diameter

If breaching occurs, the breach shape and its characteristic distances are typically as shown in Figure 23.

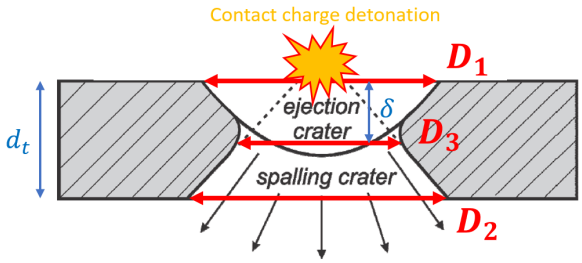

Figure 23: Typical shape of a contact blast-induced breach in a RC wall [32]

D_1 [m], the diameter of the ejection crater, is computed as:

$$D_1 = 2\left(\frac{P}{18K_0}\right)^{1/3} \tag{36}$$

where P is the TNT-equivalent explosive mass [kg] and K_0 is a material parameter that can be taken as 8.4 kg/m^3. If a breach is formed ($P > P_b$ where P_b is given by Equation (35)), the spalling crater D_2, the breach diameter D_3 and the ejection crater depth δ are approximately:

$$\begin{cases} \delta = 0.2D_1 \\ D_2 = 2d_t \\ D_3 = 2\delta \end{cases} \tag{37}$$

6.2.1.3 Contact blast on Room B

Herein, the targeted wall has the same dimensions as those specified in Section 6.1.2.3. The material is RC and the thickness $d_t = 1ft \approx 30cm$. Equation (35) yields $P_b \approx 2kg$. This mass of explosive corresponds to what can be placed in a pipe [31]. Inserting $P = 2$kg into Equations (36) and (37) yields:

$$\begin{cases} D_1 = 50cm \\ \delta = 10cm \\ D_2 = 60cm \\ D_3 = 20cm \end{cases} \tag{38}$$

This calculation can be done also for $20kg$ of TNT, which corresponds to a suitcase or backpack weapon for which:

$$\begin{cases} D_1 = 100cm \\ \delta = 20cm \\ D_2 = 60cm \\ D_3 = 40cm \end{cases} \tag{39}$$

A comparison of the effects of these two contact charges is provided in Figure 24. The steel reinforcement will likely be intact but exposed at the hole location. The bars in the front and back curtains are at 12 inches on center, meaning that objects larger than that cannot be introduced to the vault through the hole.

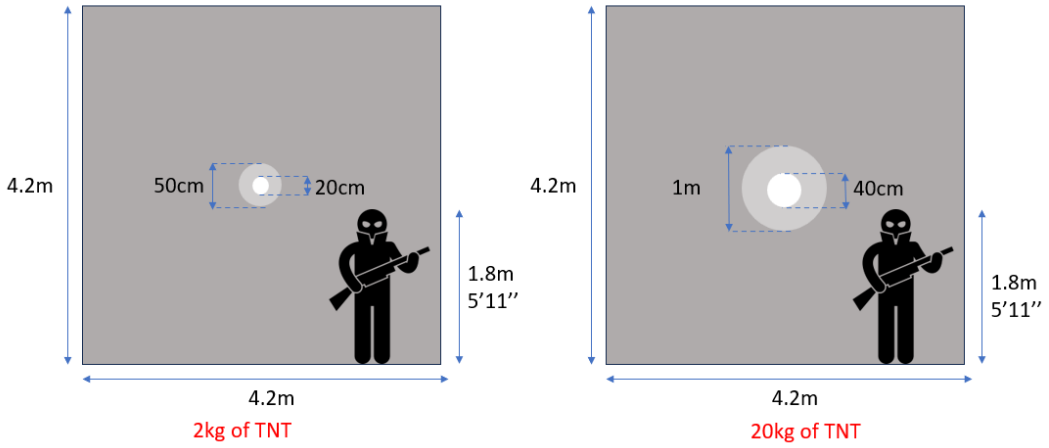

Figure 24: The effects of 2kg TNT (left) and 20kg TNT (right), on scale

6.2.1.4 Contact blast on Room A

Equation (35) can be used for a 2m-thick wall to compute the charge mass P_b required to breach room A: $P_b = 150$kg. On foot, intruders can each carry up to 23kg in a backpack or a suitcase [31]. Therefore to carry out an attack necessary to breach Room A, 6 intruders are required. Furthermore placing such a large mass of explosives on the wall is not a straight forward and would be time consuming.

Assuming that a vehicle loaded with 150kg of explosives cannot access the vault, the likelihood of a breach in Room A is very low and therefore the radiological consequences of this scenario will not be assessed.

6.2.1.5 Demolishing a RC wall to gain access to the inside of the vault

An alternate approach to gain access to the vault is to distribute a number of contact charges on the wall, in an engineered pattern, and then to detonate them in an engineered sequence: information in the domain of military engineers and not in the published literature.

6.2.2 • Required amount of explosive to breach a steel wall

The physics of breaching a steel wall is different from a RC wall because steel is ductile. The effects of a contact blast will not result in the formation of a round hole, but will create linear cuts. Breaching a steel vault requires a much deeper knowledge of explosives since they need to be shaped. This attack is not very realistic because knowledge of shaped charges is required.

6.2.3 • Summary of possible outcomes

Figure 25 summarizes possible outcomes of a contact-blast attack, based on the following assumptions:

- The vault is above ground. If buried, the only available target is the roof, which behaves like a side wall of the same thickness and span.
- The RCCS coolant is air, meaning that the heat removal system of the reactor is not compromised by the distant blast (unlike a water RCCS system whose water tank could by pierced and lose its fluid).
- The steel liner is attached to the inside face of the RC wall, meaning that scabbing of concrete does not damage equipment.
- Room A wall thickness is 2m, selected for radiation shielding. It is highly unlikely that Room A could be breached. However, if Room A walls have the same thickness as the Room B walls, because the radiation shield is not the RC structure, then the Room A and Room B walls are equally vulnerable.
- The doors to Rooms A and B are blast resistant and secured, with no unauthorized access. Intruders do not have military weapons, including shaped charges, to attack the vault.
- Intruders are on foot and cannot access the vault in a vehicle, limiting the mass of a contact charge.

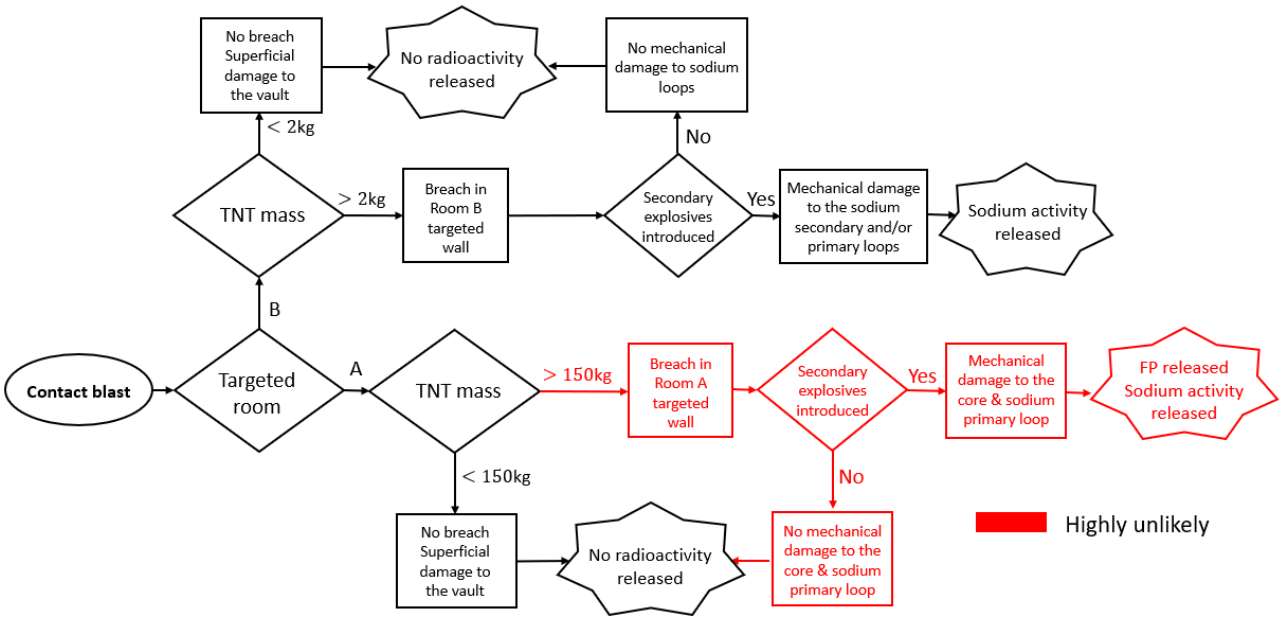

Figure 25: Summary flowchart for contact blasts

7
AIRCRAFT THREATS

7.1 Introduction to aircraft impacts

This section aims to assess the consequences of the impact of an aircraft on a microreactor, in terms of structural integrity of the different containment barriers. Although this section focuses on a specific microreactor design, the Sodium Graphite Thermal Reactor, developed by MIT Professor Koroush Shirvan (described in Section 1.4), the results are more broadly applicable.

The effects of a malevolent impact on a nuclear structure can be divided into three categories [33]:

1. Local effects: the potential perforation of the target by the engines of the aircraft.
2. Global effects: the collapse of the structure due to the impact of the aircraft.
3. Damage to Safety related Structures, Systems and Components.

A discussion about the extremely low likelihood of a direct aircraft impact on an MMR is included in Section 7.6 for both an accident and a malevolent attack.

7.2 Local effects assessment

Only the densest part of the impacting aircraft may represent the threat, namely the engines. The impacting engines, also known as the *missiles*, will penetrate the target. *Perforation* involves the missile penetrating through the target with a positive exit velocity.

Important equipment, including the vessel, are shielded by the vault reinforced concrete (RC) walls that are backed by a 6mm-thick steel plate liner as shown in Figure 1. The goal of this study is to provide guidance regarding the minimum thickness of the reinforced concrete wall to avoid local penetration by an engine, for different aircraft classes. The effect of the steel plate on the likelihood of scabbing is ignored here, although its presence will contain scabbed concrete.

The Nuclear Energy Institute (NEI) provides empirical formulae [33] that can be used to calculate the parameters of interest. This guidance is used by the U.S. Nuclear Regulatory Commission (NRC), and is adopted in the following sections.

7.2.1 • Reinforced concrete penetration

For impact on an infinitely thick reinforced concrete (RC) panel, the penetration depth x_c, in inches, is given by the following equation taken from [33]:

$$x_c = \alpha_c \sqrt{4KWND\left(\frac{V}{1000D}\right)^{1.8}}, \text{ for } \frac{x_c}{\alpha_c D} < 2 \tag{40}$$

where V is the engine velocity in ft/s, D is the average outer diameter of the engine casing in inches, W is the total engine weight in lbs, $N = 0.72$ is a coefficient that accounts for a flat-nosed missile, $K = \frac{180}{\sqrt{f'_c}}$ where f'_c is the concrete strength is psi, and α_c is a reduction factor to account for missile deformability ($= 0.5$).

The wall thickness required to prevent perforation t_p, in inches, is given by [33]:

$$t_p = \alpha_p D \left(2.2\frac{x_c}{\alpha_c D} - 0.3(\frac{x_c}{\alpha_c D})^2\right), \text{ for } \frac{x_c}{\alpha_c D} < 1.52 \tag{41}$$

where the recommended value for α_p is 0.60.

If perforation does occur, the residual speed (or exit velocity) of the missile is important, since this parameter characterizes the residual kinetic energy of the missile that damages the reactor and other equipment.

7.2.2 • Scabbing and residual speed after perforation

When a concrete wall is penetrated or perforated, back-face concrete is "scabbed". Concrete that is "scabbed" is projected into the vault (in this case) with some potential, considered small, to damage equipment. The weight of ejected concrete W_{cp} in lbs can be estimated [33] using a conical plug geometry, where the volume of ejected concrete is given by a cone with minor radius $r_1 = \frac{D}{2}$ and major radius $r_2 = r_1 + t_w \tan\theta$ where $\theta = \min\left(60°, \frac{45°}{(t_w/D)^{1/3}}\right)$ and where t_w is the wall thickness. The plug weight, for a concrete density ρ_c, is thus given by:

$$W_{cp} = \frac{\pi \rho_c t_w}{3}(r_1^2 + r_1 r_2 + r_2^2) \tag{42}$$

For missile velocities in excess of those required to perforate a given wall thickness, the equation [33] to estimate the residual (or exit) velocity V_R is:

$$V_R^2 = \frac{1}{1 + W_{cp}/W}(V_I^2 - V_P^2), \text{ for } V_I > V_P \tag{43}$$

where V_I is the impact velocity, and V_P is the missile velocity that just initiates perforation for a wall thickness t, in inches:

$$V_P = 1000D\left(\frac{D\left(2.2 - \sqrt{4.84 - 1.2\frac{t}{\alpha_p D}}\right)^2}{1.44KWN}\right)^{1/1.8} \tag{44}$$

For small W_{cp}/W and $V_I > V_P$,

$$V_R^2 = V_I^2 - V_P^2 \tag{45}$$

7.2.3 • Thickness to prevent perforation

The parameters (defined in Section 7.2.1) used for calculations are presented in Table 14. They represent roughly the characteristics of different classes of planes. In Table 14, W is the weight of one engine in each plane, because if a plane has several engines each will act as an independent missile. Moreover given the size of the vault, it is impossible for more than one engine to hit the structure. The initial impact speed $V = 492$ ft/s corresponds to a speed of 150 m/s widely used in the literature. Because this speed is well above the top speed of a leisure aircraft, the impact speed is set to 300ft/s for the Cessna in this analysis.

Table 14: Parameters used for the local effects assessment.

Parameter	**Cessna**	**Private jet**	**Regional jet**	**B737 & A320**	**B747 & A380**
α_c [/]	0.5	0.5	0.5	0.5	0.5
D [in]	50	40	80	100	100
V [ft/s]	300	492	492	492	492
W [lbs]	300	1400	3800	4400	12400
f'_c [psi]	5000	5000	5000	5000	5000
N [/]	0.72	0.72	0.72	0.72	0.72
α_p [/]	0.6	0.6	0.6	0.6	0.6

Equations (40) and (41) yield the following thicknesses to avoid perforation, presented in Table 15:

Table 15: Minimum thickness of a reinforced concrete panel to prevent perforation [cm]

	Cessna	**Private jet**	**Regional jet**	**B737 & A320**	**B747 & A380**
t_p	12	42	52	52	85

For a Cessna impact, the reinforced concrete wall thickness to avoid perforation by the engine is 12cm. If the diameter of outer engine casing is set equal to that of the spindle supporting the jet engines, greater minimum thicknesses are calculated. For example, if $D = 36$ inches for the A380, the minimum thickness increases from 85cm to 135cm. Note that:

- The dimensions and weights for the different missiles are approximate.
- It is assumed that the impact is normal to the face of the panel.
- The steel liner is ignored.

7.3 Global effects assessment of a leisure aircraft impact

Global structural response refers to the displacement response of the building. Unlike the local-effects analysis where the missile is the aircraft engine, the impact of the entire plane is considered for global analysis.

Two approaches will be developed in this report. The first one is the **Energy-balance method**, which can be carried out by hand. The second one is the **Force Response-History method**, also known as the Riera method, which requires the use of a finite element method software. In both approaches, we consider the impact of a Cessna Skyhawk 172, speed $V = 150\text{ft/s} = 46m/s$, on one of the two longer walls of the building.

- A global assessment is relevant only when much of the aircraft crashes into the target. Given the vault dimensions, this study can only be conducted for a Cessna and a private jet, as illustrated in Figure 26.
- The collision of planes is judged highly unlikely or impossible for a number of reasons mentioned in Section 7.6.

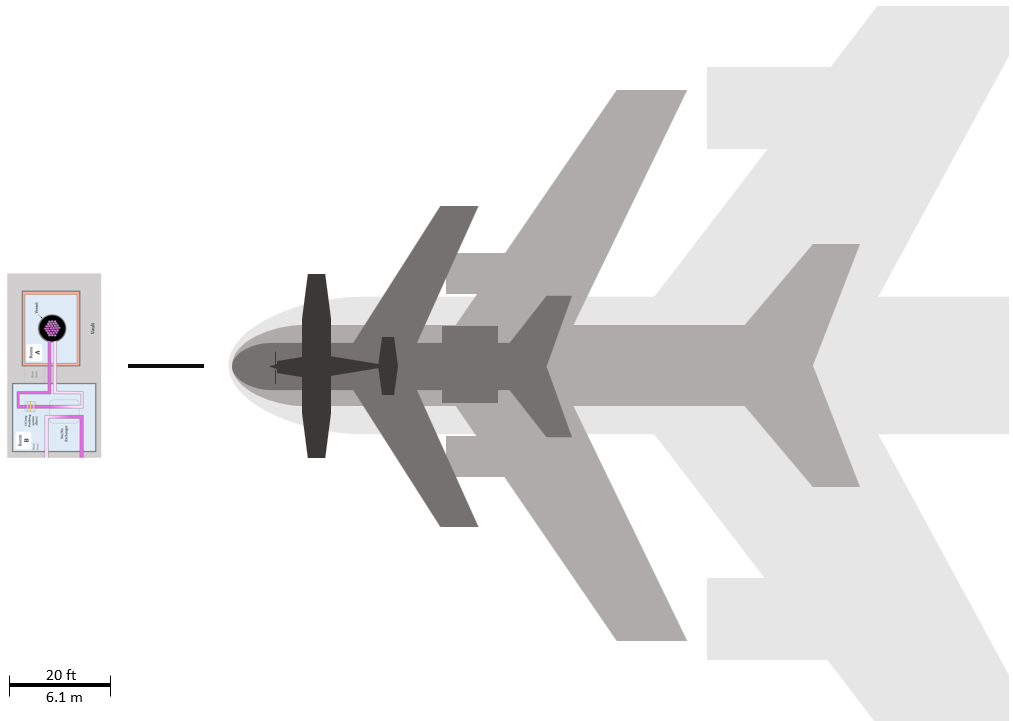

Figure 26: Different types of aircraft represented on scale with the SGTR vault. From the lightest to the darkest shade: A380, A320, Falcon 7X, Cessna 172 Skyhawk

It is assumed that most of the kinetic energy imparted by the plane is absorbed by the impacted structural member. Here the lateral supports of the impacted wall are considered rigid and assumed able to withstand the lateral loads generated by the impact. The dimensions of the wall and the area of impact are shown in Figure 27 where the dimensions of 1.45m, 1.95m and 0.145m were chosen to represent the shape of the 172 Skyhawk projected onto the plane of impact.

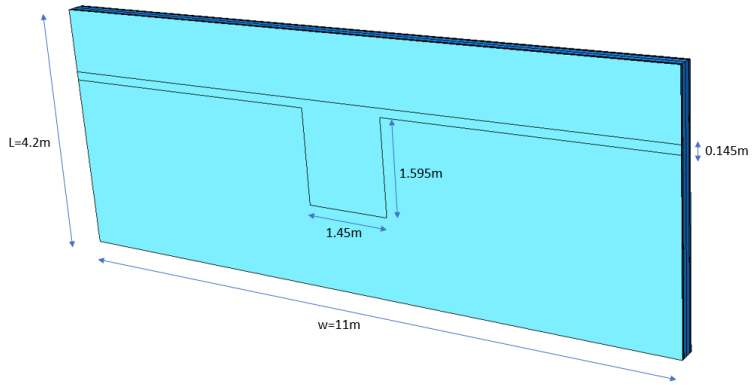

Figure 27: Area of impact and wall dimensions

7.3.1 • Energy-balance method

As explained in Section 6.3.3.1 of [34]: *"The objective of the energy-balance method of global response evaluation is to determine whether the target structure can absorb the energy that is imparted to it without deforming excessively. This method uses the principles of conservation of energy and conservation of momentum, and requires that the energy absorption capability (SE) of the target be greater than the kinetic energy imparted to it (E_a). It recognizes that, since a significant portion of the impact energy is dissipated in deforming the aircraft body, the effective missile mass is less than the total mass of the aircraft but more than the mass of the rigid components, such as the engines. The effective missile mass for calculating the total kinetic energy of impact (E_i) will depend on the mass of the engines and the relative rigidity of the aircraft body."*

***SE* calculation:** The energy absorption capability SE of the target structure is determined per Section 6.3.3.1 of [34]:

$$SE = R_m y_e(\mu - 0.5) \tag{46}$$

where R_m is the maximum resistance of the Single Degree Of Freedom (SDOF) system [lb], y_e is the maximum elastic displacement of the SDOF system and μ is the maximum permissible ductility ratio which is here a parameter taken as $\mu = 3$ for RC walls and roofs in [35].

First, y_e can be calculated as $y_e = R_m/k$, where k is the stiffness defined in Section 6.1.2.3 and Equation (46) becomes, for $\mu = 3$:

$$SE = \frac{2.5R_m^2}{k} \tag{47}$$

The value for SE is therefore dependent on R_m and k.

Here the 30cm-thick wall with #6 Grade 60 reinforcement at 12 inches on center, each way, in each face of the wall is analyzed: the wall analyzed in Section 6.1.2.3. The total thickness of the wall d_t and the effective depth of the tension reinforcement are:

$$d_t = 30cm = 11.8in \tag{48}$$

$$d = d_t - 2in = 9.8in \tag{49}$$

Most of the following parameters are given for a 1-foot-wide strip of wall, denoted /ftw. The moment of inertia of the cross-section is:

$$I = \frac{d_t^3 \times 12in}{12} = 1643 \text{ in}^4/\text{ftw} \tag{50}$$

The cracked stiffness is:

$$k_{cr} = 0.4\frac{384EI}{5L^3} = 44,500 \text{ lb/in/ftw} \tag{51}$$

E is the concrete Young's modulus ($= 4.0 \times 10^6$psi for $f'c = 5000$psi) and L is the height of the wall ($= 4.2$m$= 157.48$in). The flexural reinforcement ratio is $\rho = 0.365\%$ ($= \frac{0.44}{12\times10}$) and ρ is conserved for other thicknesses. Therefore the area of reinforcement A_s is:

$$A_s = d \times \rho \times 12in = 0.43\text{in}^2/\text{ftw} \tag{52}$$

The maximum plastic moment resistance M_p of the panel, per foot width, is:

$$M_p = 0.9A_s f_y = 2.3 \times 10^5 \text{ lb-in/ftw} = 1.9 \times 10^4 \text{ lb-ft/ftw} \tag{53}$$

where $f_y = 60,000$psi is the steel yield strength, and d the effective depth of the reinforcement from the compression face of the wall.

The maximum resistance R_m is therefore:

$$R_m = \frac{8M_p}{L} = \frac{8 \times 1.9 \times 10^4}{13.8} = 1.1 \times 10^4 \text{ lb/ftw} \tag{54}$$

and the energy capacity, SE, per foot width is:

$$SE/\text{ftw} = 2.5\frac{R_m^2}{k_{cr}} = 2.6 \times 10^4 \text{ lb-in/ftw} \tag{55}$$

which yields the total energy capacity of the wall of width $w = 11$m$= 36.09$ft:

$$SE = SE/\text{ftw} \times w = 9.8 \times 10^5 \text{ lb-in} \tag{56}$$

This calculation can be performed for different thicknesses. Results are reported in Figure 28. The quasi-linear dependency of SE on d_t can be observed, which is expected since $Rm \propto d_t^2$, for ρ held constant, and $k_{cr} \propto d_t^3$ therefore Equation (46) yields $SE \propto d_t$. Note that $\mu = 3$ is low, with substantially greater values possible.

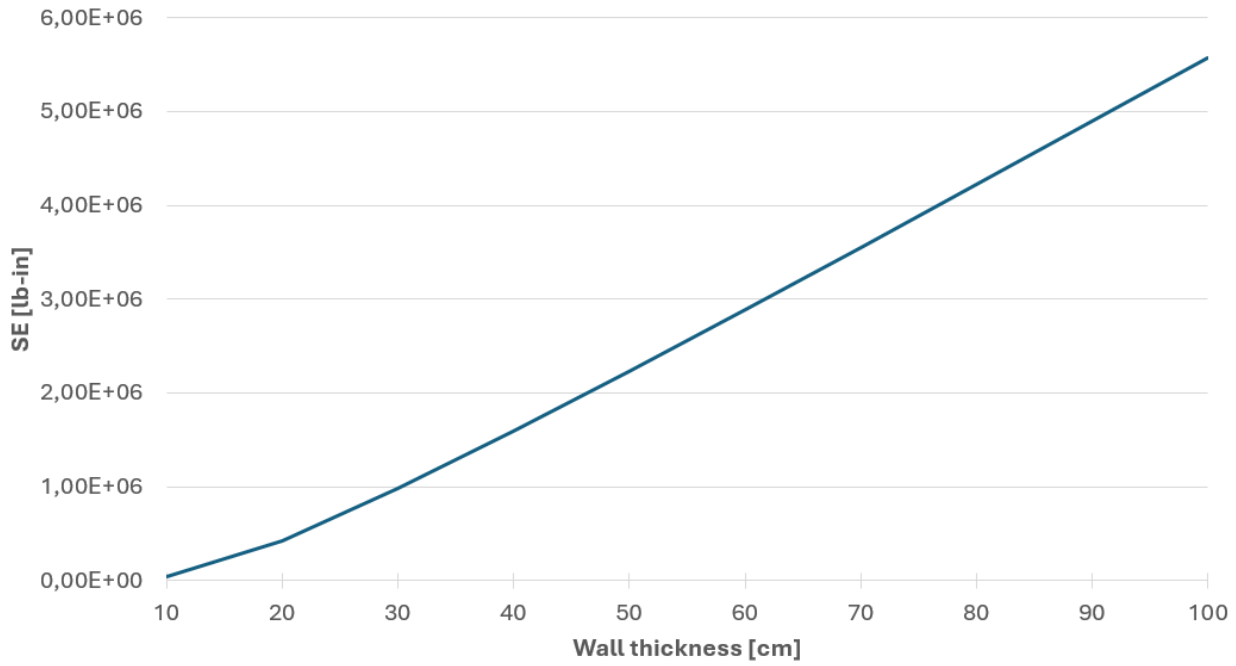

Figure 28: Energy absorption capacity as a function of wall thickness, $\rho = 0.365\%$ (each face), Grade 60 reinforcement, $f'c = 5000$psi

E_a calculation: The effective missile mass, m, can be conservatively set equal to the total mass of the Cessna plane: $m = 2300lb \approx 1043kg$.

To calculate E_a, the effective target mass M_e may conservatively be taken as the mass of the target structure that is included within $d_t/2$ of the periphery of the impact interface [34], where d_t is the thickness of the target in the direction of missile travel. This extended impact surface is noted S_e. However M_e should not be less than 10% of the total mass of the target wall. The impact area shown on Figure 27 has a surface $S = 3.91m^2 = 42.1ft^2$. The relation between S and S_e is calculated using the dimensions shown in Figure 27:

$$S_e = S + d_t \times (w + 1.595\text{m}) \tag{57}$$

where w is the width of the wall and $= 11m = 433in$. For a 30cm-thick wall $S_e = 7.69m^2$. For a concrete density of $\rho_c = 2,500kg/m^3$, $M_e = \rho_c S_e d_t = 5,766kg = 12,712lb$.

The fraction of the plane's kinetic energy that will be imparted to the target depends on how deformable it is. The imparted energy E_a is between the lower limit, $E_{a,min}$, which corresponds to a plastic impact where the aircraft moves with the target, and the upper limit, $E_{a,max}$, which corresponds to an elastic impact. Section 6.3.3 of [34] gives:

$$\begin{cases} E_{a,min} = \frac{1}{2}mV^2 \frac{m}{m+M_e} \\ E_{a,max} = \frac{1}{2}mV^2 \frac{4m/M_e}{(1+\frac{m}{M_e})^2} \text{ if } \frac{m}{M_e} < 1 \end{cases} \tag{58}$$

Reference [35] recommends comparing SE to the geometric average of the two limits, if the deformability of the aircraft is unknown:

$$E_a = \sqrt{E_{a,min} E_{a,max}} \tag{59}$$

For the 30-cm-thick wall, with #6 at 12in each face, and $m = 2,300lb = 1,043kg$, $M_e = 12,712lb = 5,766kg$, $V = 46m/s = 150ft/s$:

$$E_{a,min} = 169,000J \tag{60}$$

$$E_{a,max} = 572,500J \tag{61}$$

and therefore

$$E_a = 3.11 \times 10^5 \text{ J } = 2.75 \times 10^6 \text{ lb-in } > 9.8 \times 10^5 \text{ lb-in} \tag{62}$$

Since $E_a > SE$, it can be concluded that a 30cm-thick wall with #6 at 12in each face would be badly damaged, and potentially collapse following the impact of the Cessna plane. Solutions include increased reinforcement, increased wall thickness, and a greater value of μ. This calculation was performed for different thicknesses: results are presented in Table 16:

Table 16: Cessna impact, energy absorption capability, and imparted energy for different wall thicknesses. The thicknesses collapse may occur/cannot occur are colored in red/green.

d_t **[cm]**	10	20	30	40	50	60	70
SE **[lb-in]**	4,02E+04	4,25E+05	9,79E+05	1,59E+06	2,23E+06	2,89E+06	3,55E+06
E_a **[lb-in]**	6,49E+06	4,16E+06	2,75E+06	1,93E+06	1,42E+06	1,08E+06	8,54E+05

Conclusion of the energy-balance global effects assessment For a Cessna Skyhawk plane, weighting 2300lb, impacting at 150ft/s a concrete wall with a flexural reinforcement ratio of 0.365%, the thickness needs to be 50cm to ensure that the wall will not collapse.

7.3.2 • Response-history method

To confirm the results yielded by the energy-balance approach, the response-history method, also known as the Riera method, is conducted using a finite element software: ABAQUS. This method involves applying a pressure load on the targeted structure corresponding to the crushing aircraft forces. This pressure is applied on the 2D projection of the aircraft on the target: the area drawn on Figure 27. Force-history curves are derived from experimental or calculated data and are provided in [35] for some common aircraft. The curve corresponding to a Cessna Skyhawk 172 with a take-off weight of 2300lb, flying at 150ft/s, is displayed in Figure 29:

The maximum force corresponds to the weight of roughly 50 elephants, although applied only for a few milliseconds. This force is converted into a pressure applied uniformly on the plane-shaped-area depicted in Figure 27. Details of the wall model and the constitutive material models implemented in ABAQUS are provided in Section 6.1.3.1.

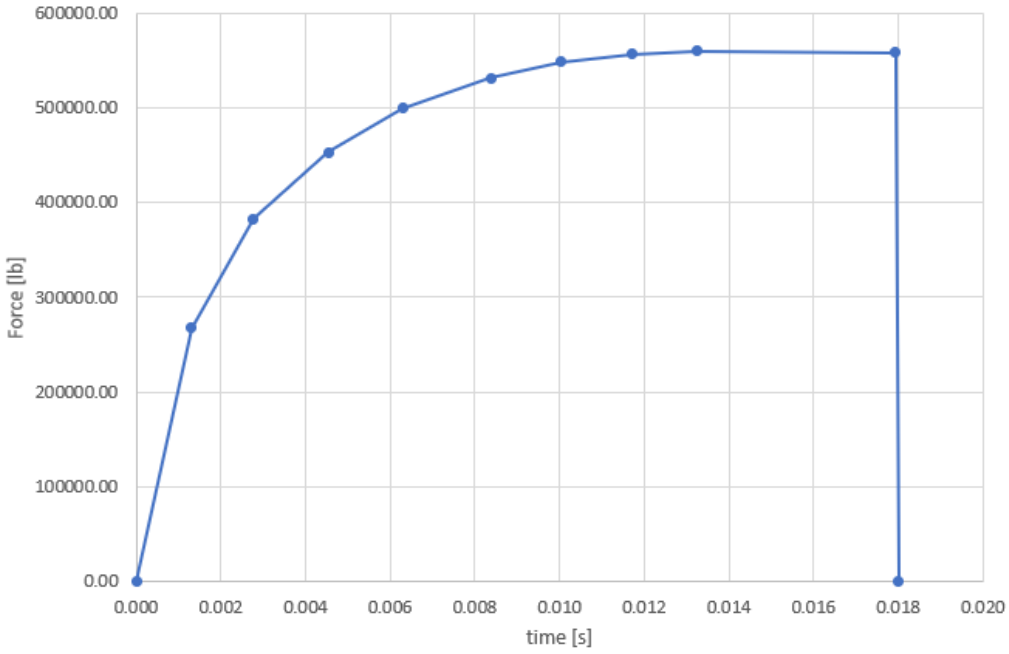

Figure 29: Response-history curve for a Cessna Skyhawk 172, $m = 2,300$lbs, and $V = 150$ft/s

Simulation results: Simulation were run for a 30cm-thick wall and a 50cm-thick wall. The reinforcement is modeled as steel plates, with Johnson-Cook plasticity behavior. The thickness of the plates was chosen to conserve a flexural steel reinforcement ratio of 0.365%. The Concrete Damage Plasticity (CDP) model was adopted for the concrete. Further details can be found in Section 6. The simulations are run for 100ms after the impact, with data saved every 0.5ms. The results for the 30-cm thick wall 100ms after the impact are displayed in Figure 30:

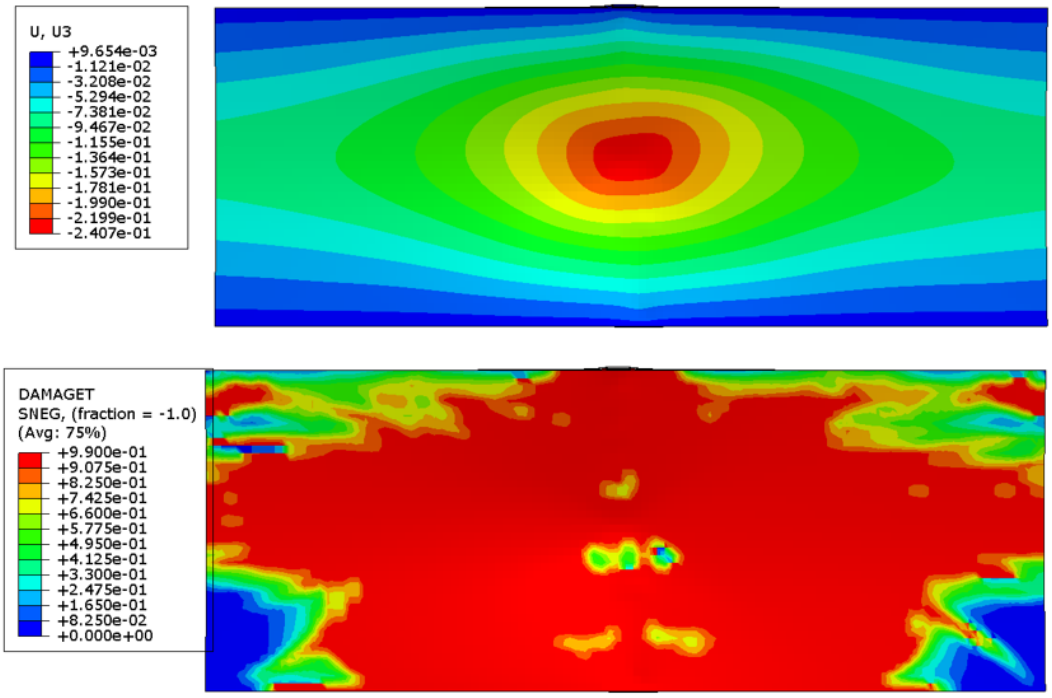

Figure 30: Simulation results for the front face of a 30-cm-thick wall of reinforced concrete hit by a Cessna plane. Top: displacement [m] in the U3 direction (normal to the plane of display). Bottom: Tensile damage.

The predicted displacement along the impact direction is 24cm, which is greater than the collapse criterion calculated in Equation (33). Another indication of significant damage is the area of failed concrete (tensile damage > 0.9, where tensile damage is defined in Equation 34), contoured in red in the bottom panel of Figure 30.

The energy-balance calculations above indicated that a 50-cm-thick concrete wall with a flexural reinforcement ratio $\rho = 0.365\%$, should withstand the impact without collapse. A simulation was run using the Riera method to compare results, which are displayed in Figure 31. The maximum predicted displacement is 2.4cm, well below the collapse displacement of $10.5cm$ yielded by Equation (33). Moreover, local material failure is not widely spread on the wall, as it was for the 30cm-thick wall. This result is in agreement with the energy-balance method.

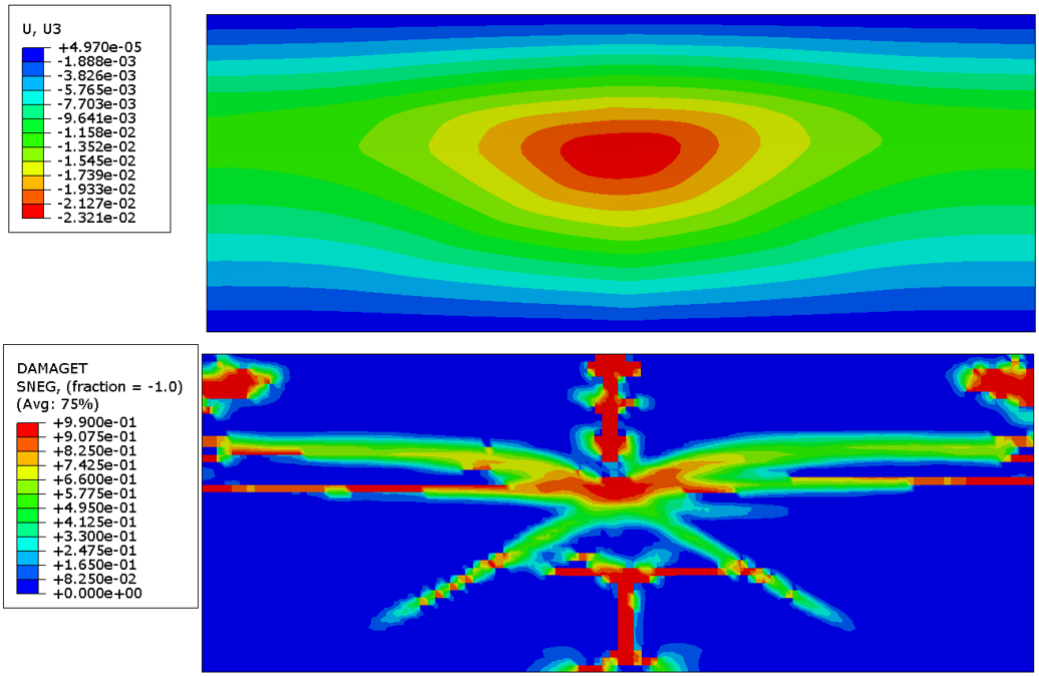

Figure 31: Simulation results for the front face of a 50-cm-thick wall of reinforced concrete hit by a Cessna plane. Top: displacement [m] in the U3 direction (normal to the plane of display). Bottom: Tensile damage.

7.3.3 • Conclusions

A global assessment was conducted for a RC vault of different wall thicknesses. The normal impact of a Cessna plane weighing 2,300lb, impacting one of the two long walls at 150ft/s, was assessed. Two NRC-recommended methods were used for analysis: the energy-balance method, which can be implemented with hand-calculations, and the response-history method, which relies on a FE software. Both methods indicate that a 50cm-thick wall with a flexural steel reinforcement ratio of 0.365% will resist to impact. The effect of the steel liner has not been taken into account.

7.4 Global assessment of a private jet impact

For the impact of a private jet, the striking aircraft will be considered to be a Falcon 7X. The maximum mass of the plane is $m_{plane} = 30,000$kg and the mass of one of its three engines is $m_{engine} = 500$kg. Reference [34] recommends for "large aircraft" taking the effective mass of the missile to be 8 times the mass of one engine as long as the result is between $30 - 100\%$ of the total aircraft mass. For a Falcon 7X, $8 \times m_{engine} < 30\% \times m_{plane}$ therefore the effective mass m is taken to be $m = 0.3 m_{plane} = 9,000$kg. Reference [34] does not define a "large aircraft" but the reference used is Chelapati's report [36], which defines a large aircraft as one weighing more than 12,000lb (= 5400kg), which therefore applies to the Falcon 7X but not not the Cessna. The speed before impact is the maximum cruise speed 250m/s. The impact is assumed to be normal to the vault wall, as displayed in Figure 32; such an impact is virtually impossible.

The impacted surface S is identified by the black lines, while the extended impacted surface S_e is

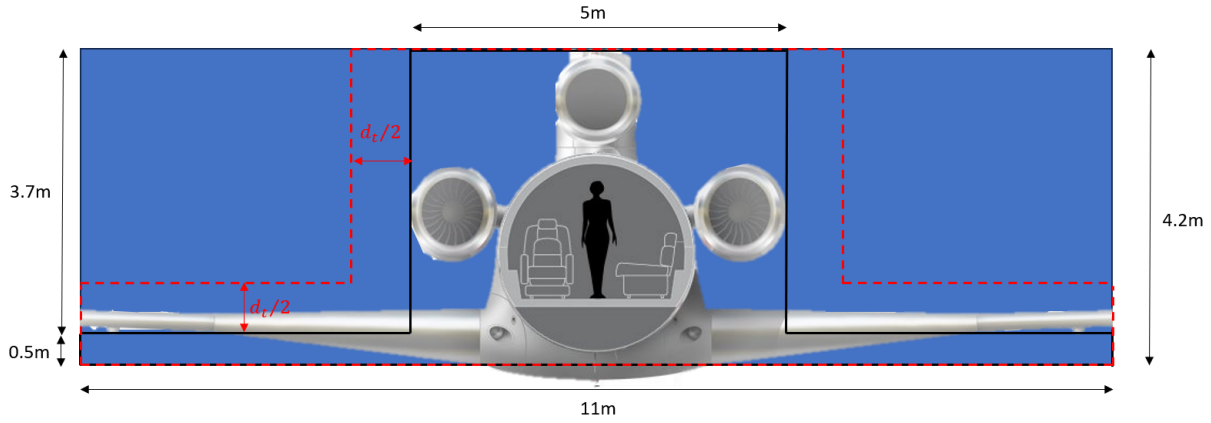

Figure 32: Falcon 7X impact on the vault, on scale.

identified by the red discontinuous lines. Using the Falcon 7X and the wall dimensions,

$$S = 4.2 \times 5 + 0.5 \times (11 - 5) = 24m^2 \tag{63}$$

$$S_e = S + \frac{d_t}{2} \times (11 - 5) + \frac{d_t}{2} \times (4.2 - \frac{d_t}{2} - 0.5) \times 2 = S + d_t(6.7 - \frac{d_t}{2}) \tag{64}$$

The energy-based analysis is repeated for the Falcon 7X and results presented in Table 17. The Room A wall, which is 2m-thick, should not collapse following a private jet impact. The intrusion of parts of the plane into room B may ignite a sodium fire that could release part of the MAR contained in the activated coolant. Again, the steel liner is ignored in this analysis.

Table 17: Falcon 7X impact, energy absorption capability, and imparted energy for different wall thicknesses. The thicknesses for which collapse may occur/cannot occur are colored in red/green.

d_t **[cm]**	10	20	30	40	50	60	70
SE **[lb-in]**	4,02E+04	4,25E+05	9,79E+05	1,59E+06	2,23E+06	2,89E+06	3,55E+06
E_a **[lb-in]**	5,83E+07	4,24E+07	3,27E+07	2,63E+07	2,19E+07	1,86E+07	1,61E+07
d_t **[cm]**	80	90	100	110	120	130	140
SE **[lb-in]**	4,22E+06	4,89E+06	5,57E+06	6,24E+06	6,92E+06	7,60E+06	8,28E+06
E_a **[lb-in]**	1,41E+07	1,25E+07	1,12E+07	1,01E+07	9,23E+06	8,45E+06	7,77E+06
d_t **[cm]**	150	160	170	180	190	200	210
SE **[lb-in]**	8,96E+06	9,64E+06	1,03E+07	1,10E+07	1,17E+07	1,24E+07	1,31E+07
E_a **[lb-in]**	7,18E+06	6,67E+06	6,21E+06	5,81E+06	5,45E+06	5,12E+06	4,83E+06

7.5 Discussion on jet-fuel fire

Another aircraft crash effect that must be assessed is the fire produced by the combustible material brought by the plane. A report from IAEA [24] shows that jet fuel represents between 70% and 90% of this combustible material. Therefore *"the amount of jet-fuel at take-off is the relevant fuel load for fire investigations"*. In this subsection, the fire hazard induced by a leisure plane impact and a private jet impact are assessed. It should be noted that only the jet fuel combustion is considered: the heat generated by a potential sodium fire inside of the SGTR's vault is not accounted for. However the thermal energy generated by a sodium fire in SGTR is very small compared to what comes from the jet-fuel fire. Indeed in the case of sodium reacting with water to form sodium hydroxide, the thermal energy released by 1L of liquid sodium is 13.3MJ to be compared to 46MJ for 1L of kerosene. Moreover, the total volume of sodium (primary and secondary loops) is estimated to be 340L which can be compared to the jet-fuel volumes mentioned below: (200L-30,000L).

The jet fuel volume carried by a small leisure plane is taken as $V = 200L$, with a density of $\rho = 0.8$ kg/L. The total mass of fuel is therefore $m_{tot} = 160$ kg. For a private jet, the fuel tank volume varies significantly with the size of the aircraft. Most private jet range around 4000 L, but it should be noted that some private jet have a tank capacity up to $30,000$ L which will be the value selected for this section's calculations. At the moment of the impact, some of this fuel is instantaneously burnt in the form of a fireball, while the rest of it forms a pond that burns on the nearest horizontal surface. When the distance between the impact location and the closest horizontal surface is small (which is the case for both an impact on the vault roof or a wall) it is estimated that about 50% of the jet fuel mass burns in the fireball [24], and the rest in the pool fire.

Pool fire For further details on pool fires, see Section 4. An impact on the roof of the vault is considered, so that the fuel spills on the roof and walls. The maximum volume of fuel which can effectively cover the vault has been estimated around 640 L. For a Cessna impact, the jet fuel volume contributing to the pool fire is $m = \frac{m_{tot}}{2} = 100$ L$<$ 640 L. For the private jet impact, the pool fire volume is $m = \frac{30{,}000}{2} = 15,000$ L. However most of this fuel will flow out of the vault and the volume covering the vault will virtually be around 640 L. The heat radiated to the vault by the burning fuel that is not directly in contact with the vault is neglected. For both cases, the intruder-induced pool fire studied in Section 4 is worse(or equivalent) in terms of heat transferred to the core. The study conducted for this scenario shows that the temperature rise in the core does not exceed the maximal temperature for the cladding and the fuel, provided the RCCS starts to cool the reactor after the fire is over. It should be noted that even in case of penetration of the aircraft into Room B (which could happen for a private jet impact or even a Cessna impact if Room B walls are less than 30cm thick), the pool fire which could occur inside room B consequently would still be separated from the core by the interior wall of the vault (which is part of the reinforced concrete shield). Therefore the study carried out in Section 4 is still a good estimation of the heat radiated to the core.

Fireball When an aircraft hits a structure, instantaneously part of its fuel is released and ignited in the form of a fireball. This phenomenon can generally be divided into three stages [24]: formation of the combustible mixture cloud, burning associated with a spherical or hemispherical fireball, and uplift of the mushroom plume. Given the small dimensions of the vault, it is estimated that 50% of the total fuel mass m_{tot} transported by the aircraft will contribute to the fire ball. Hence $m = \frac{m_{tot}}{2} = 80$

kg for a leisure aircraft. The diameter D_{fb} (in m) of the fireball is given by the following equation:

$$D_{fb} = 5.8m^{1/3} \tag{65}$$

For a leisure plane, D_{fb}=25 m. This value shows that the fireball even for the smallest class of aircraft should cover the whole vault (whose longest dimension is 11 m). For a private jet transporting 30,000 L of fuel, the fireball is expected to have a diameter around 130 m. Tests have been conducted to determine the emissive power (that is the radiated power) of a fireball. The emissive power is reported to range between 80 kW/m^2 and 200 kW/m^2 for kerosene masses between 100 kg and 100,000 kg [37]. The recommended value for fire hazard studies for fireballs involving more than 1,000 kg of fuel is however 350 kW/m^2. We can conservatively assume that this surface emissive power is fully received by the vault without attenuation. This power is received by the vault as long as the fireball lasts. The duration of the fireball Δt is given by the following equation [24]:

$$\Delta t = 0.45m^{1/3} \text{ if } m < 30,000 \text{ kg} \tag{66}$$

Thus the fireball lasts around 2s for a leisure aircraft and 10s for a private jet. As a consequence, the vault undergoes:

- 200 kW/m^2 applied on its whole surface for 2s in the case of a fireball generated by a leisure plane aircraft.
- 350 kW/m^2 applied on its whole surface for 10s in the case of a fireball generated by a private jet.

Given the fact that the pool fire study has demonstrated that the reactor can withstand a power per unit of surface of 120 kW/m^2 during 82s, given the fact that during a fireball the total thermal energy received is less than for a pool fire, given the fact that the the sodium coolant for the SGTR have no time to be drained and contribute to increase the thermal inertia of the reactor, it is concluded that the heat generated by the fireball and absorbed by the vault is not a serious concern and could not induce a radioactive release. The last danger of the fireball is the mechanical damage associated with the shock wave generated by the sudden expansion phase, but it appears to be negligible compared to the mechanical load created by the aircraft impact itself.

Conclusion It is concluded that the fire threats induced by an aircraft impact, namely a jet-fuel pool fire and fireball, are not the primary trigger of a severe accident involving a radioactivity release. The main concern is the impact in itself and the risk to start a sodium fire (in the case of the SGTR) or cause mechanical damage to the core.

7.6 Discussion on the likelihood of aircraft impacts

In anticipation of conducting a more comprehensive Probabilistic Risk Assessment (PRA) in future studies, with the aim of selecting which attack scenarios should be considered Design-Basis, a discussion is presented here on what type of aircraft impact is a realistic scenario. For this discussion, aircraft are separated into two categories:

- Commercial aircraft: These planes which typically weight more than 150000 kg are operated by airlines and usually embark more than a hundred passengers.
- Private aircraft: These planes can be privately owned and/or piloted. This category includes leisure aircraft (e.g. Cessna type planes) and private jets.

The purpose of this section is to assess how plausible a commercial aircraft strike on a small nuclear structure is.

7.6.1 • Accidental strike

A commercial aircraft strike on a microreactor could happen by accident. Reference [36] presents a probabilistic assessment of aircraft hazard for full-scale nuclear power plants. Table 18 presents results.

Table 18: Probability of damage to an 18-inch wall due to an impact of aircraft [36].

Plant location from airport[c]	Aircraft type	Probability of strike/year	Perforation mode of damage		Collapse mode of damage	
			Conditional probability	Absolute probability	Conditional probability	Absolute probability
≤ 5 miles	Small	3.3−5[a]	0	0	0	0
	Large	1.1−6	0.52	5.7−7	0.56	6.2−7
	Total	3.4−5[b]		5.7−7[b]		6.2−7[b]
> 5 miles	Small	1.4−5	0.06	8.4−7	0	0
	Large	4.6−7	1.00	4.6−7	0.88	4.0−7
	Total	1.4−5[b]		13.0−7[b]		4.0−7[b]

(a) 3.3−5 denotes 3.3×10^{-5}.
(b) Multiply these values by 0.01 for damage probabilities for specific equigment.
(c) Actual strike probability near an airport varies approximately as $1/r^2$, where r is the distance from the airport.

The probability of strike per year depends on the plant location from airport, and the aircraft type: small refers to aircraft lighter than 12,000 lbs (5.4 t) and large to aircraft heavier than 12,000 lbs. The probabilities of damage by perforation or collapse are also presented, for a 18in-thick wall (45.72 cm).

The probability of strike per year of a full-scale nuclear power plant (NPP) within 5 miles of an airport, by a large aircraft is $p_{\text{NPP}} \approx 10^{-6}$. This probability has been calculated using the shadow

area of a full-scale NPP struck with a 10° angle to the horizontal. For a small nuclear plant such as that studied here, this probability can be divided by a factor of 100 since this shadow area is about 100 times smaller. However, the air-traffic has significantly increased (about 10 times) between the 1970s when the study was conducted and nowadays. Therefore the probability of strike per year p_{NB} by a commercial aircraft on a NB within 5 miles from an airport can be estimated to be:

$$p_{\mathrm{NB}} = p_{\mathrm{NPP}} \times 10 \div 100 \approx 10^{-7} \tag{67}$$

If there are a fleet of 10 such plants, all within 5-miles of an airport, the frequency of occurrence f of commercial aircraft crash on **one plant** can be crudely estimated to be:

$$f = 10 \times p_{\mathrm{NB}} \approx 10^{-6}/\mathrm{yr} \tag{68}$$

Such a strike on one single plant occurs roughly every 1,000,000 years. This calculation presents an order of magnitude estimate of the likelihood of such an event. The crash of a commercial aircraft on an MMR is very unlikely, which is part of the justification to rule it out as a MHA.

7.6.2 • Intentional strike

Since an accidental commercial aircraft crash on a small nuclear power plant is judged very unlikely, the question of intentional impacts must be raised. Intentional impacts could be caused by terrorists hijacking and taking the command of the plane, or a rogue pilot already having control on the aircraft. In the recent history, there is only one precedent of a "successful" hijacking of a commercial aircraft used to target structures: the terrorist attacks of September 11, 2001, in the United States. The situation nowadays is different from different perspectives:

- Since these deadly attacks, the airport and cockpit security has been dramatically increased, making it virtually impossible for terrorists to take the command of a commercial aircraft.
- Passengers aboard a hijacked commercial aircraft in the US would almost certainly aim to regain control
- The concept of jet fighters operational permanently ready to take-off and take-down a hijacked airplane believed to be on a suicide mission has been thoroughly developed in countries like the U.S. and France.
- The ability for a commercial pilot to crash a plane precisely on a small target (see Figure 26) remains questionable. In addition to the small size of the target, a commercial aircraft has a minimum speed (stall speed) of around 50 m/s. If a terrorist were piloting the plane as slow as possible (to hit the target), a mistake in heading of 10° just 10s before impact would result in the plane missing the target by 100m.

Besides, the existence of valuable targets (more valuable symbolically, economically, politically or in potential death toll) and bigger targets, easier to hit, may deter terrorists from aiming at a small nuclear plant. The authors question why an organization with the means to plan and conduct a terrorist attack would choose a small nuclear plant as a target, with all the drawbacks and uncertainties.

7.6.3 • Conclusion on commercial aircraft strikes

Since an accidental commercial aircraft strike is highly unlikely, and an intentional strike is considered extremely unlikely for the reasons mentioned above, this threat will not be selected as a MHA, and will not influence the determination of the site boundaries. Moreover, given the size of a commercial aircraft compared to the vault (*cf* Figure 26), if an impact were to occur, only one engine could hit the vault. It has been calculated and reported in Figure 15 that the thickness to prevent perforation by a commercial plane engine ranges between 50cm and 80cm. Therefore no penetration of Room A should occur if struck by a commercial aircraft, and a direct hit on the core is impossible.

7.6.4 • Modes of damage

The damage results for small aircraft impacts are in agreement with the conclusion yielded by the global and local studies of this report for a Cessna impact. For a Cessna, the calculation presented in this report shows that collapse of the struck wall is avoided for a wall thicker than 50 cm (20 in) approximately. Such a plane falls under the characterization by [36] as a small aircraft, and collapse never occurs according to Table 18 for a 18in-thick RC wall.

Moreover, for impact by a Cessna, perforation by the engine has been estimated in this report to be avoided for a reinforced concrete wall thicker than 12 cm (*cf* Table 15). For a 18in-thick (45.72 cm) RC wall, Table 18 shows that the probability of perforation is zero.

Finally, perforation by a regional aircraft or an even bigger plane like a A320 was estimated to be avoided for a wall thicker than 50 cm (see Table 15). Per Chelapati *et al.* [36], for a large aircraft, the most likely outcome in case of an impact is the collapse of the impacted structure.

7.7 Summary of possible outcomes

Figure 33 summarizes the different possible outcomes of an aircraft strike. It is assumed that if collapse of a wall occurs, the equipment inside the breached room is damaged and releases radioactivity. In real life, collapse does not imply perforation, since the thickness required to prevent perforation for each type of aircraft (Table 15) is always greater than the thickness to required to prevent collapse (Section 7.3). Therefore collapse does not imply that equipment inside the vault will suffer any direct hit. Figure 33 relies on some assumptions:

- The impact is either horizontal on a side wall, or vertical on the roof. If the vault is buried, then it can only be vertical on the roof (provided it can be seen).
- The RCCS coolant is air, meaning that the heat removal system of the reactor is not compromised by the impact (unlike a water RCCS system whose water tank could by pierced and lose its fluid).
- The steel liner is inside the radiation shield, meaning that scabbing does not damage important equipment.
- Room A wall thickness is 2m: the radiation shield. Room A is not compromised by impact by either a leisure aircraft or a private jet, and is not mentioned in the branches of the diagram.

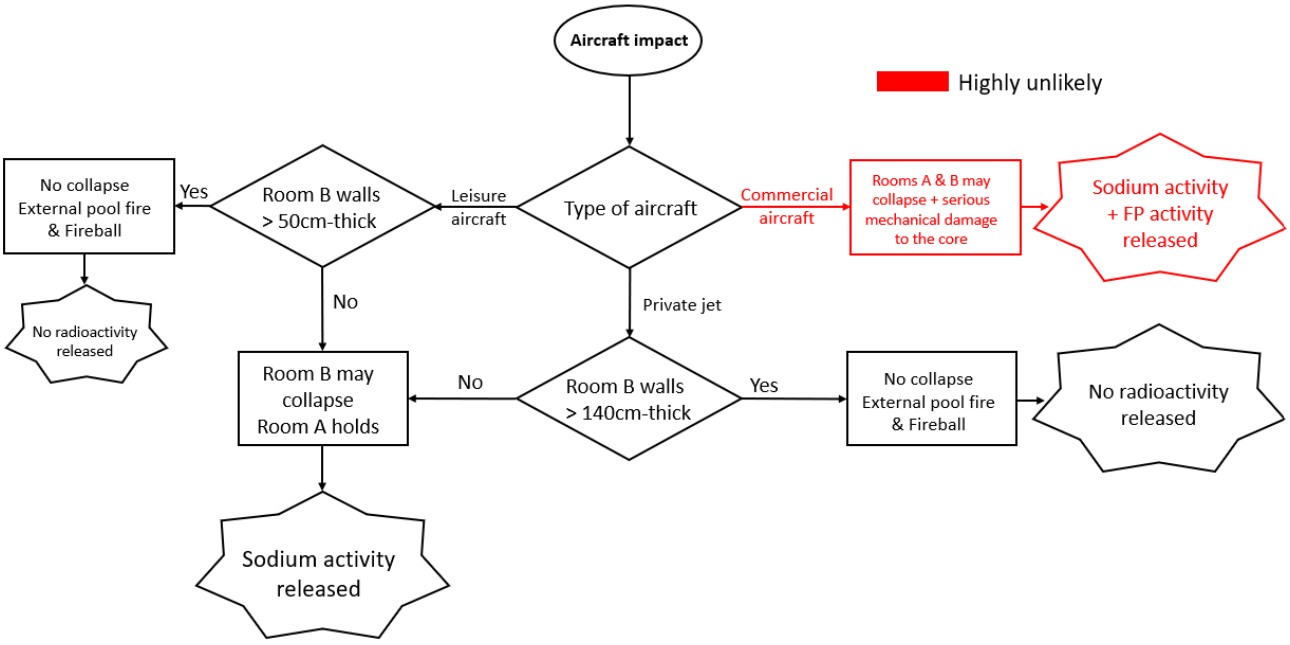

Figure 33: Summary flowchart for aircraft impacts

8
WIND-BORNE MISSILE IMPACT

8.1 Introduction

This section explores wind-borne missiles, a natural phenomenon distinct from the intentional security threats studied earlier. As wind-borne missiles are not deliberately initiated by malicious actors, this analysis primarily concerns safety rather than security. This short section is included in the discussion due to the valuable insights it provides from a physical security perspective. Building upon the examination of aircraft crashes, the study of wind-borne missiles offers a relevant comparison to assess potential impacts from ram cars and other projectiles, thus enhancing our understanding of risks to the reactor facility.

Wind-borne missiles can reach significant speeds during a tornado or a hurricane. The purpose of this section is to provide guidance regarding the required thickness to prevent perforation or scabbing, as defined in Section 7. Terranova et al. [38] summarize the types of missiles and prescribed velocities recommended in different U.S. standards and guidelines:

"Section 3.5.1.4 of the United States Nuclear Regulatory Commission (USNRC) Standard Review Plan, Missiles Generated by Extreme Winds [39] and the Department of Energy (DOE) Natural Phenomena Hazards Analysis and Design Criteria for DOE Facilities [40] point to Regulatory Guide (RG) 1.76 [41], RG 1.221 [42], and ANS-2.3 [43] for the definition of missiles and impact velocities for the design of exterior, above-grade reinforced concrete walls and roof panels. The design-basis missiles identified in RG 1.76 (tornadoes), RG 1.221 (hurricanes), and ANS-2.3 (tornadoes and hurricanes), namely, an automobile, Schedule 40 pipe, and solid steel sphere, are listed in [Table 19], including their physical dimensions and weights, and maximum impact velocities. The design-basis missiles specified by the USNRC and ANS documents are identical but the impact velocities specified in RG 1.221 are significantly greater than those specified in ANS-2.3 for hurricanes."

Table 19: Summary of design-basis missiles and impact velocities for wind-borne missile impact [38].

Missile type	Dimensions, mm (ft)	Mass, kg (lbs)	Maximum impact velocity, m/s (ft/s)			
			USNRC		DOE	
			RG 1.76	RG 1.221	ANSI/ANS-2.3-2011	
					Tornadoes	Hurricanes
Automobile[a]	5000 × 2000 × 1300 (16.4 × 6.6 × 4.3)	1810 (4000)	41 (135)	113 (372)	44.7 (147)	78.3 (257)
Schedule 40 pipe	168.2 mm diameter × 4572 mm long (0.552 ft diameter × 15 ft long)	130 (287)	41 (135)	94.2 (309)	44.7 (147)	55.9 (183)
Solid steel sphere	25.4 mm diameter (0.08 ft diameter)	0.067 (0.147)	7.9 (26)	84.7 (278)	11 (37)	55.9 (183)

[a] Alternate dimension in ANS-2.3 but mass is the same.

In this study, a particular focus will be on the Schedule 40 pipe missile and the automobile:

- Previous work [38] has shown that the Schedule 40 pipe has the potential to penetrate reinforced

concrete (RC) walls ad slabs.

- The automobile is a common heavy object, which could reach significant speeds as shown in Table 19. The risk is not penetration of a RC wall but a potential collapse (global effects as described in Section 7.3) of the impacted structure, which is the reactor building here.

8.2 Schedule 40 pipe penetration

Terranova et al. [44] have shown that none of the empirical formulae available in the literature accurately predict either the penetration depth, or the required thickness to prevent scabbing and perforation. Terranova et al. [38] simulated experiments involving steel pipes impacting reinforced concrete panels to benchmark material models, and then developed recommendations for minimum panel thickness to prevent perforation and scabbing, as a function of concrete compressive and tensile strength. Their results are reported in Tables 20 and 21 for a 4.57m-long and 276kg-heavy Schedule 40 pipe:

Table 20: Minimum panel thickness, $f'_c > 30$ MPa, $f'_t > 3$ MPa [38].

Schedule 40 pipe diameter [mm]	Impact velocity [m/s]	Prevent perforation [mm]	Prevent scabbing [mm]
152	40	305	381
	44.7	305	381
	55.9	305	460
	100	381	460
203	40	305	381
	44.7	381	460
	55.9	460	559
	100	650	838
254	40	381	460
	44.7	381	559
	55.9	460	650
	100	650	914

Table 21: Minimum panel thickness, $f'_c > 50$ MPa, $f'_t > 5$ MPa [38].

Schedule 40 pipe diameter [mm]	Impact velocity [m/s]	Prevent perforation [mm]	Prevent scabbing [mm]
152	40	305	305
	44.7	305	305
	55.9	305	305
	100	305	381
203	40	305	381
	44.7	305	381
	55.9	305	381
	100	460	460
254	40	305	381
	44.7	305	460
	55.9	381	559
	100	650	650

Using the values shown in Table 20, which corresponds to a lower grade of concrete, the most penetrating object is a Schedule 40 pipe with a diameter of 254mm flying at a speed of 100m/s. This speed corresponds roughly to the highest realistic speed that such an object could reach during a hurricane or a tornado as displayed in Table 19: 94.3m/s. The required thickness to prevent perforation is 65cm in that case. The first conclusion that can be drawn from this study is that this kind of wind-borne missile does not threaten to perforate Room A and therefore cannot directly damage the core. However, perforation of the Room B walls is possible (albeit very unlikely) and such a missile could damage equipment in this room, including the heat exchanger between the primary and secondary loops or Na-piping. Such damage associated with a breach in the vault and the presence of oxygen could result in a sodium fire, which could in turn result in the release of MAR coolant. Lastly, if a water RCCS is chosen to be the emergency heat removal system, the water tank feeding the RCCS could be perforated, disabling it. The perforation of the tank has not been studied but it is noted that the exit velocity of the perforating missiles are low, see [38] for details.

8.3 Automobile impact global assessment

Herein, the impact of an automobile on the wall of the reactor building is studied, to judge whether it might result in building collapse. Unlike an aircraft, an automobile does not have a long steel shaft as part of the engine, which considerably decreases its perforation potential. The most damaging missile in this category is prescribed in [42]: a 1810kg automobile, $5m \times 2m \times 1.3m$, at 113m/s.
To estimate the damage that could be caused by this missile, the energy-balance method used in Section 7.3.1 for the global assessment of a Cessna impact is used. The energy absorption capability SE does not depend on the missile nature and has already been calculated, and displayed in Figure 28. The imparted energy E_a will be calculated following the same method as for the Cessna impact. A 30-cm-thick wall is considered: Room B. The most damaging impact is normal, and when the projected surface of the car on the wall is minimal. This surface is the rectangle $2m \times 1.3m$ in Figure 34.

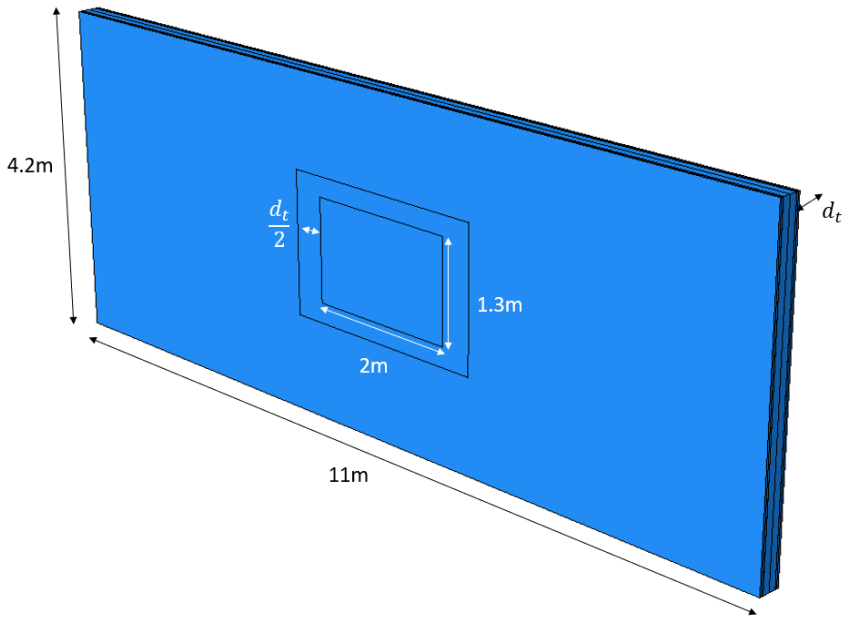

Figure 34: Shape of the impact area on the targeted wall.

The extended impact surface S_e is derived the following way:

$$S_e = 2 \times \left(\frac{2\text{m}}{2} + \frac{d_t}{2}\right) \times 2 \times \left(\frac{1.3\text{m}}{2} + \frac{d_t}{2}\right) \tag{69}$$

The effective mass of the target M_e is therefore given by:

$$M_e = \rho_c S_e d_t = 2760 \text{ kg} \tag{70}$$

where $\rho_c = 2500$ kg/m^3 is the concrete density and d_t is the total thickness of the wall. But because this value is below 10% of the total mass of the wall, the retained value of the effective mass is $M_e = 10\% \times 4.2 \times 11 \times d_t \times \rho_c = 3465$ kg. We then apply Equations (58) and (59) with $V = 113$m/s, $m = 1810$kg and M_e as just calculated to get:

$$E_a = 6.4 \times 10^6 \text{ J } = 5.7 \times 10^7 \text{ lb-in} > SE(30\text{cm}) \quad (71)$$

Since $E_a > SE$, it can be concluded that a 30cm-thick wall with #6 at 12in each face, each way, would be badly damaged, and potentially collapse following the impact of the automobile missile. Solutions include increased reinforcement, increased wall thickness, and a greater value of μ. This calculation was performed for different thicknesses: results are presented in Table 22:

Table 22: Automobile impact, energy absorption capability, and the imparted energy for different wall thicknesses. The thicknesses for which collapse may occur/cannot occur are colored in red/green.

d_t **[cm]**	10	20	30	40	50	60	70
SE **[lb-in]**	4,02E+04	4,25E+05	9,79E+05	1,59E+06	2,23E+06	2,89E+06	3,55E+06
E_a **[lb-in]**	7,79E+07	6,73E+07	5,69E+07	4,88E+07	4,26E+07	3,60E+07	3,01E+07
d_t **[cm]**	80	90	100	110	120	130	140
SE **[lb-in]**	4,22E+06	4,89E+06	5,57E+06	6,24E+06	6,92E+06	7,60E+06	8,28E+06
E_a **[lb-in]**	2,54E+07	2,16E+07	1,85E+07	1,59E+07	1,38E+07	1,21E+07	1,06E+07
d_t **[cm]**	150	160	170	180	190	200	210
SE **[lb-in]**	8,96E+06	9,64E+06	1,03E+07	1,10E+07	1,17E+07	1,24E+07	1,31E+07
E_a **[lb-in]**	9,37E+06	8,32E+06	7,42E+06	6,64E+06	5,97E+06	5,39E+06	4,88E+06

This calculation shows that Room A walls which are 2m thick should withstand the impact, meaning that such a missile could not cause direct damage to the core. However, it could break into Room B since it is very likely that Room B walls will be thinner than 1.6m. The worst accident associated with such an impact is therefore a sodium fire releasing the coolant activity. Once again, it should be mentioned that the water tank for the RCCS (if it relies on a water coolant) could by pierced and emptied .

8.4 Discussion

Wind-borne missiles are not part *stricto sensu* of physical security since the scenarios discussed in this section are not initiated by humans but are natural. That being said, this side study is interesting for the safety analysis since it proves that the worst possible radioactive release initiated by a wind-borne missile is a sodium fire release, which could occur in case of penetration of Room B and damage to piping or the heat exchanger. Besides, the automobile missile study is interesting also for the physical security analysis, since it rules out a vehicle-ramming attack as a serious threat to the reactor, as the impact speed will be very small compared to 113m/s (= 253mph). It should be noted that the automobile or Schedule 40 pipe impacts results are extremely conservative, because the impacts are assumed perfectly normal to the wall surface which is highly unlikely. Terranova et al. [45] demonstrated via LS-DYNA simulations that small increases in the angle of attack (or obliquity) greatly reduced the likelihood of both scabbing and perforation for a given impacting missile and panel. It is highly likely that a 300mm-thick wall would not be perforated by a Schedule 40 pipe impacting at 100m/s. Finally, to the knowledge of the authors, there is no precedent case of such wind-borne missiles significantly damaging walls/roofs in civilian or nuclear infrastructure.

9
RADIOLOGICAL IMPACT ASSESSMENT FOR DESIGN-BASIS THREATS

This section presents calculations for the accident source term and public dose for the previously examined representative DBT scenarios, presenting them in terms of emergency zone sizes (LPZ and EPZ). To express the accident source term in terms of public Total Equivalent Dose Exposure (TEDE) and determine zone sizes for siting purposes, a 1-D Gaussian plume atmospheric dispersion model is employed. Details regarding the atmospheric model utilized are outlined in Section 9.1, while Section 9.2 elaborates on the formula employed to calculate the TEDE. The radioactive inventories utilized in these calculations are derived from the MAR evaluation conducted for reactor fuel and coolant activation, as discussed in Section 2.

Radioactivity release for these scenarios can occur either through the leakage of activated sodium coolant or through the release of fission products contained in the reactor fuel after the breach of several physical barriers separating the fuel elements from the environment. It is determined in Section 4 that reasonable external fire threats are not capable of inducing any release. Sabotage of the RCCS, addressed in Section 5, could eventually lead to the breach of several barriers, resulting in the release of reactor fission products into the atmosphere. Additionally, Design-Basis blasts and aircraft crash threats, covered in Sections 6 and 7, respectively, are likely to trigger primary sodium coolant leaks in Room B. Two models have been developed to quantify the release for these scenarios: a primary sodium coolant pool fire model described in Section 9.3 and a mechanistic source term assessment of a Prolonged Loss-of-Heat-Removal (PLHR) in Section 9.4. Section 9.4 also extensively details the methodology used for the Mechanistic Source Term (MST) assessment.

Methods used below to assess the source term of representative DBT scenarios follow the NRC requirements provided in :

- The Regulatory Guide RG 1.183 [9] This Guide provides assumptions and methods that are acceptable to the NRC staff for performing design basis radiological analyses to assess an Exclusion Boundary Area (EAB) or a Low Population Zone (LPZ).
- The Regulatory Guide RG 1.242 [8] provides assumptions and methods that are acceptable to the NRC staff for performing design basis radiological analyses of an advanced reactor and assess its Emergency Planning Zone (EPZ).

Initial Conditions (ICs) At the time of the accident, it is assumed that the reactor is operated at the "ultimate power level contemplated" (10-CFR-50.34 [2]). Once the accident is detected, it is assumed that the reactor shuts down and that the draining mechanism starts draining the primary sodium coolant from the core. Reactor Cooling Cavity System (RCCS) coolant is assumed to be air. Previously in this report, the possibility of adding additional physical barriers such as Hesco barriers to the current layout was studied. It is assumed in this section that such barriers are not implemented around the reactor.

9.1 Atmospheric dispersion

Atmospheric dispersion in the environment is assessed by using a Gaussian plume model (i.e. Pasquill diffusion) and a 1-dimensional wind. The 1-D Gaussian plume model has indeed convenient site-independent and linear properties for this study allowing to aggregate independent release sources and disregard the time-dependency of the release in the integrated result. Comparison of dispersion factors found using the Gaussian model is made with a statistical study compiling dispersion factors for 17 sites obtained with PAVAN, an NRC-issued code, using joint frequency distributions (JFDs) of wind direction, wind speed, and atmospheric stability class to estimate X/Q values for specific averaging time periods at specified distances. It was found that the simple Gaussian plume model used here provides good orders of magnitude of dispersion factors.

Examples of documents from the the U.S. Nuclear Regulatory Commission and the U.S. Department of Energy in which the Gaussian plume model is used are NUREG-0396 [46] and DOE-HDBK-1224-2018 [16]. The Gaussian puff dipersion factor equations are derived from the model developed by H. A. Panofsky and J.A. Dutton [47]. Gaussian plume equations and refinements of the Gaussian plume models used here are based on discussion and documents availaible from the 7th IAEA MEREIA Webinar on *Basic Concepts - Introduction to atmospheric dispersion process and models* that took place in March 2023. [48].

9.1.1 • Atmospheric conditions

Atmospheric stability class and dispersion factors Atmospheric conditions can be described in terms of atmospheric stability. The most conservative assumption for the calculation is to consider dispersion when atmospheric conditions are the most stable. Therefore, Pasquill Gifford stability class is assumed to be of class "F". It is noted that applying a "F" stability class for an analysis lasting for several days is very conservative, as it is practically only reached during night-time.

Dispersion parameters used in the Gaussian plume and puff models directly depend on the Pasquill stability class. Briggs urban model described in DOE-HDBK-1224-2018 [16] is used to assess the dispersion parameters. His urban model is selected because, unlike others, it is applicable for downwind distances below 500 m and can still be conservative for longer distances (beyond 10 km). The urban dispersion parameters for a Pasquill Gifford stability class "F" given in [16] are as follows :

$$\begin{cases} \sigma_x = \sigma_y = 0.11 \times x \times (1 + 0.0004 \times x)^{-0.5} \\ \sigma_z = 0.08 \times x \times (1 + 0.0015 \times x)^{-0.5} \end{cases} \tag{72}$$

where x is the downwind distance from the release point (m).

Wind conditions In our model, the conservative assumption is made that the wind is constant in both speed and direction. It is also 1-dimensional, meaning that the the wind blows parallel to the ground and that we compute dispersion factors downwind. These constant wind properties allow the Gaussian plume model to have good summation properties, enabling emissions from independent sources to be easily aggregated in the code. However, in real life, varying winds reduce the doses received by a member of the public remaining at a fixed point for the whole period of the accident.

In terms of wind speed, the most conservative assumption in terms of maximum dose reached in a single point would be to consider no wind at all, and the model would assume the source term to pile up at the reactor site. Indeed, as noted in [48] the direct application of the Gaussian model for very small wind speed values leads to predicting very high concentration values, since the wind speed is in the denominator of the model equations. In terms of wind speed less than 2 $m.s^{-1}$, a recommendation of a IAEA Guide published in 1980 [49] is to multiply the value of the dispersion value σ_y by 4.

In the study, it is necessary to select the same conservative minimum wind speed, but large enough so that (1) the Gaussian plume model is applicable (2) the source term is transported far enough to maximise the size of the resulting Low Population Zone (LPZ) and Emergency Planning Zone (EPZ). Hence, a wind speed of $u = 2\ m.s^{-1}$ is selected in this study, which represents the minimum speed at which the IAEA's suggestion of dividing the dispersion by 4 does not apply. This choice guarantees that the resulting dispersion model effectively represents universal (site-independent) and conservative atmospheric dispersion.

9.1.2 • Gaussian puff model 1-D - instantaneous release

For an instantaneous release, the general formula giving the dispersion factor at the point in space (x,y,z) is as follows:

$$\frac{\chi(x,y,z)}{\Gamma}[s.m^{-3}] = \int_0^\infty \frac{1}{(2\pi)^{3/2}\sigma_x\sigma_y\sigma_z} e^{-\frac{(x-ut)^2}{2\sigma_x^2}} e^{-\frac{y^2}{2\sigma_y^2}} (e^{-\frac{(z-h)^2}{2\sigma_z^2}} + e^{-\frac{(z+h)^2}{2\sigma_z^2}}) dt \tag{73}$$

with :

- $\chi(x,y,z)$ the integrated activity concentration at the point in space (x,y,z) ($Bq.s.m^{-3}$),
- Γ the source term (Bq),
- u the wind speed ($m.s^{-1}$) in the x direction,
- σ_x, σ_y, σ_z the dispersion factors in all directions in space,
- h the height of release, when considering full reflection of the plume on the ground,

In the Mechanistic Source Term code, the following assumptions are made :

- Since we wish to calculate the maximum dose at any point, the dispersion factor is evaluated at the direct down wind of the radioactive effluent, i.e., $y = 0\ m$.
- Ground-level release is assumed : $h = 0\ m$.
- As the final public dose is mainly due to inhalation of radioactive material, the dispersion factor is evaluated at height $z_0 = 1.7m$, average adult height.

When applying the following assumptions to Equation (73), the final dispersion factor obtained is as follows :

$$\frac{\chi}{\Gamma}[s.m^{-3}] = \int_0^\infty \frac{1}{(2\pi)^{3/2}\sigma_x\sigma_y\sigma_z} e^{-\frac{(x-ut)^2}{2\sigma_x^2}} \times 2e^{-\frac{z_0^2}{2\sigma_z^2}} dt \tag{74}$$

9.1.3 • Gaussian plume model 1-D - continuous release

For a continuous release, the general formula giving the dispersion factor at the point in space (x,y,z) is as follows:

$$\frac{\chi(x,y,z)}{\Gamma}[s.m^{-3}] = \frac{1}{2\pi u \sigma_y \sigma_z} e^{-\frac{y^2}{2\sigma_y^2}} (e^{-\frac{(z-h)^2}{2\sigma_z^2}} + e^{-\frac{(z+h)^2}{2\sigma_z^2}}) \tag{75}$$

with :

- $\Gamma = \int_0^\infty \dot{\Gamma} dt$ the integrated source term (Bq).
- $\chi(x,y,z)$ the integrated activity concentration at the point in space (x,y,z) ($Bq.s.m^{-3}$),
- u the wind speed ($m.s^{-1}$) in the x direction,
- σ_x, σ_y, σ_z the dispersion factors in all directions in space,
- h the height of release, when considering full reflection of the plume on the ground,

In the Mechanistic Source Term code, the following assumptions are made :

- Since we wish to calculate the maximum dose at any point, the dispersion factor is evaluated at the direct down wind of the radioactive effluent, i.e., $y = 0\ m$.
- Ground-level release is assumed : $h = 0\ m$.
- As the final public dose is mainly due to inhalation of radioactive material, the dispersion factor is evaluated at height $z_0 = 1.7m$, average adult height.

When applying the following assumptions to Equation (75), the final dispersion factor obtained is as follows :

$$\frac{\chi}{\Gamma}[s.m^{-3}] = \frac{1}{\pi u \sigma_y \sigma_z} e^{-\frac{z_0^2}{2\sigma_z^2}} \tag{76}$$

with

$$\Gamma = \int_0^\infty \dot{\Gamma} dt$$

The dispersion factors depending on distance for the Gaussian puff model (Equation (74)) and the Gaussian plume model (Equation (76)) are displayed in Figure 35, in both logarithmic and semilog scales.

Time-independence of release on the dispersion factor It is noted that dispersion factors from an instantaneous or continuous release are almost equal. Actually, it would be expected that the curves would be exactly equal as time-dependance of the release is not expected to influence the dispersion factor. The only difference between the curves comes from an approximation made in the case of a plume, where diffusion in the x direction is neglected, which makes it possible to integrate analytically Equation (73) to obtain Equation (75).

This time-independance of release only holds here because the wind is considered to be constant. Conceptually, this property is equivalent to the fact that the sum of independent Gaussian random

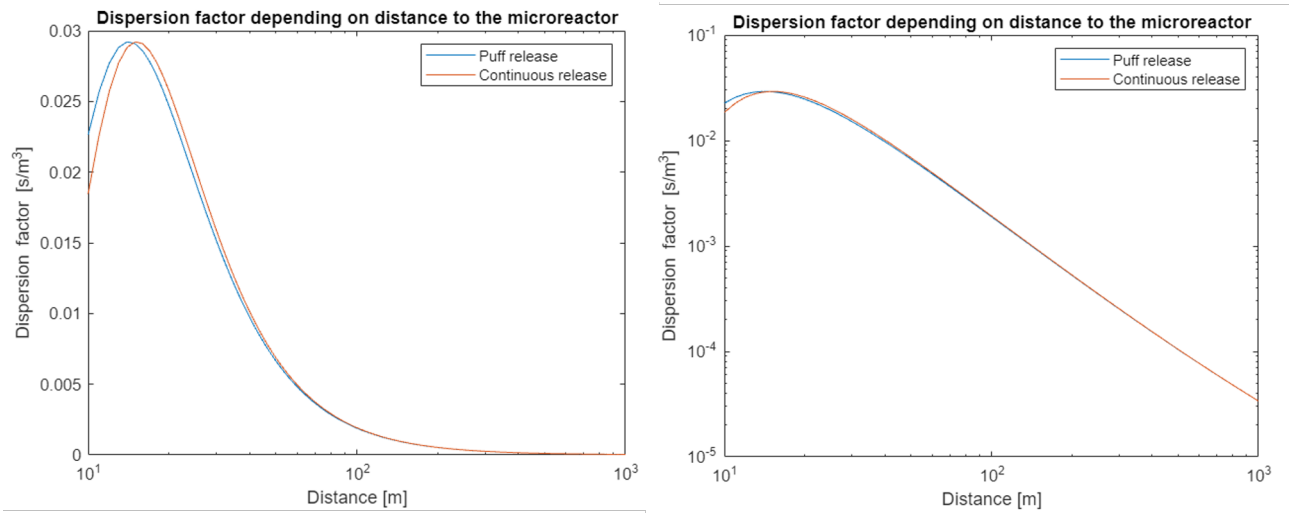

Figure 35: Comparison between the Gaussian puff and Gaussian plume models

variables is Gaussian. More pragmatically, this property can be proven by representing the plume as a sequence of infinitesimal puffs, with each released puff having an independent impact in term of public dose exposure at a given distance (assuming other factors like the breathing rate as constant) :

$$\chi(x, y, z, t) = \sum_{i=0}^{\infty} \chi_i(x, y, z, t) \tag{77}$$

Generally speaking, this linearity property means that independent releases aggregate. This property is used several times in the code, and is used in the study to break down the impact of different release sources.

The atmospheric dispersion model finally implemented in the code is the *Gaussian plume model*, which saves computing time due to the simplicity of the equation.

An inherent minimal site boundary ? It is noted that with the considered atmospheric model, the maximum dispersion factor is attained at a distance of 15m from the reactor. Therefore, there is to be a Low Population zone LPZ or an Emergency Planning Zone EPZ, which stands in our model at at least 15 m of the microreactor. In other words, the probability distribution of zones in siting is discontinuous : between 0 and 15m, the zone in siting probability distribution is null.

9.1.4 • Comparison with PAVAN results

PAVAN is a computer code developed by the U.S. NRC, which uses joint frequency distributions (JFDs) of wind direction, wind speed, and atmospheric stability class to estimate $\frac{\chi}{Q}$ values for specific averaging time periods at specified distances. The model is based on a straight-line Gaussian model that assumes the release rate is constant for the entire period of the release. PAVAN implements all the NRC requirements listed in Regulatory Guide 1.145 *Atmospheric dispersion models for potential*

accident consequence assessments at nuclear power plants.

The study *Engineering Evaluation of $\frac{\chi}{Q}$ Values Consistent with Regulatory Guide 1.145.* [50] evaluates $\frac{\chi}{Q}$ values at defined downwind distances from hypothetical ground-level and elevated releases using meteorological data from 17 nuclear sites. An average of the site's instantaneous maximum dispersion factor and elevated 95% percentile dispersion factors for a release of 4 to 30 days is compared to the Gaussian Plume model in Table 23.

Table 23: Comparison between Gaussian plume and PAVAN dispersion factors [50]

Distance	**Gaussian Plume** Dispersion factor $\frac{\chi}{Q}$ $(s.m^{-3})$	**PAVAN** Dispersion factor $\frac{\chi}{Q}$ $(s.m^{-3})$ Elevated 95% percentile 4 - 30 days release	**PAVAN** Dispersion factor $\frac{\chi}{Q}$ $(s.m^{-3})$ maximum site value
400 m	1.5×10^{-4}	1.2×10^{-4}	3.35×10^{-3}
800 m	4.81×10^{-5}	-	1.05×10^{-3}

Traditionally criticized within the nuclear community for its excessive conservatism, the Gaussian plume model exhibits dispersion factor values at 400m and 800m that are, nonetheless, lower than the instantaneous maximum values obtained in PAVAN's study across 17 nuclear sites. The Gaussian plume model however yields values that align closely with the conservative estimates (95% confidence margin) of dispersion factor averaged over 4 to 30 days for these sites, supporting the coherence of the model used in simulating a mechanistic source term over one month.

While the Gaussian plume model's dispersion factor values remain comparable with PAVAN results beyond 400m, it is essential to note that advanced site-specific atmospheric dispersion codes like PAVAN, MACCS, or ARCON96 have become industry standards in licensing processes. These advanced codes, designed to better capture Brownian motion and wind variability, can produce lower dispersion factors closer to the reactor compared to the Gaussian model's peak dispersion factor, which reaches 0.029 $s.m^{-3}$, 15m away from the release point. In the pursuit of avoiding the surpassing of radioactivity release thresholds that define emergency zones (EPZ and LPZ), it is indeed crucial to minimize this maximum value.

9.1.5 • Dry deposition

For the determination of the exclusive area boundary (EAB) and low population zone (LPZ), RG 1.183 [9] states that *"no correction should be made for depletion of the effluent plume by deposition on the ground"*. However, concerning the Emergency planning zone (EPZ), the newly adopted RG 1.242 [8] accepts the implementation of *"corrections for radioactive decay and ingrowth, wet or dry deposition (or both), and plume rise due to buoyancy or momentum (or both), as appropriate"*.

The dry deposition model implemented is derived from documents issued for the 7th MEREIA Webinar on *Basic Concepts - Introduction to atmospheric dispersion process and models* that took place in March 2023. [48].

Ground contamination due to dry deposition is proportional to the activity concentration near ground $\chi(x, y, 0)$ $(Bq.s.m^{-3})$. The proportionality constant is called deposition velocity or precipita-

tion rate ν_d $(m.s^{-1})$. According to [48], Brenk et al. provided the best estimates of the deposition velocity ν_d $(m.s^{-1})$ for effluents from nuclear facilities which are summed up in Table 24. This value is determinated experimentally by measuring ground contamination after the passage of a contaminating cloud and comparing it to the integrated concentration.

Table 24: Deposition velocity $(m.s^{-1})$ for each transport group [48]

Transport group	**Deposition velocity ν_d $(m.s^{-1})$**
1. Noble gases	0
2. Elemental iodine (reactive gas)	10^{-2}
2. Organic iodine (unreactive gas)	10^{-4}
2. Aerosols	10^{-3}

The reasoning to determine the correction factor to be applied to the source term to account for dry deposition is described in [48]. To ground coordinates (x,y), the amount deposited is thus equal to $\nu_d\ \chi(x,y,0)$ $(Bq.m^{-2})$. The differential equation reflecting the impact of dry deposition on the source is given in Equation (78) :

$$\frac{d\Gamma(x)}{dx} = -\int_0^x \int_0^\infty \nu_d\ \chi(x,y,0)dydx \tag{78}$$

With :

$$\chi(x,y,0) = \frac{\Gamma(x)}{\pi u \sigma_y \sigma_z} e^{-\frac{y^2}{2\sigma_y^2}} e^{-\frac{h^2}{2\sigma_z^2}} \tag{79}$$

By substituting Equation (79) - obtained through the Gaussian plume model 1-D described in Equation (75) - in Equation (78), and after integration, the correction factor given in Equation (80) is obtained.

$$\frac{\Gamma(x)}{\Gamma(0)} = exp(-\sqrt{\frac{2}{\pi}}\frac{\nu_d}{u}\int_0^x \frac{1}{\sigma_z} exp(-\frac{h^2}{2\sigma_z^2}dx)) \tag{80}$$

9.2 Public Dose Exposure Formula

The requirements, methodology and relevant references to compute the dose exposure for a member of the public are described in RG 1.183 [9] Part 4, *Dose Calculational Methodology* for the Low Population Zone (LPZ) and in RG 1.242 [8] for the Emergency Planning Zone (EPZ). Both Regulatory Guides establish the **Total Effective Dose Equivalent (TEDE)** as the acceptance criteria. the TEDE is the sum of the committed effective dose equivalent (CEDE) from inhalation and the deep dose equivalent (DDE) from external exposure.

The Dose Conversion Factors (DCF) to account for the CEDE (inhalation of radioactive material) should be derived from the data provided in ICRP Publication 30, *"Limits for Intakes of Radionuclides by Workers"* [51]. The DDE (external exposure) is nominally equivalent to the effective dose equivalent (EDE) if the whole body is irradiated uniformly. It should be calculated assuming submergence in semi-infinite cloud and using the EDE conversion factors from Table III.1 of Federal Guidance Report 12, "External Exposure to Radionuclides in Air, Water, and Soil" [52].

The formula used to calculate CEDE, DDE and TEDE are respectively shown in Equations (81), (82) and (83).

$$CEDE = \sum_{nuclide\ i} \Gamma_i \times DCF_i \times BR \times \frac{\chi}{\Gamma} \tag{81}$$

$$DDE = \sum_{nuclide\ i} \Gamma_i \times h_E^i \times \frac{\chi}{\Gamma} \tag{82}$$

$$TEDE = CEDE + DDE = \sum_{nuclide\ i} \Gamma_i \times (DCF_i \times BR + h_E^i) \times \frac{\chi}{\Gamma} \tag{83}$$

with :

- $CEDE$ (Sv), DDE (Sv) and $TEDE$ (Sv) the Committed Effective Dose Equivalent, the Deep Dose Equivalent and the Total Effective Dose Equivalent respectively.
- Γ_i the source term of nuclide i (Bq)
- DCF_i the dose conversion factor of nuclide i taken from ICRP publication 119 [51] $(Sv.Bq^{-1})$
- h_E^i the effective dose equivalent coefficient of nuclide i $(Sv.Bq^{-1}.s^{-1}.m^3)$, i.e., the effective dose equivalent per unit time-integrated exposure to the radionuclide i, extracted from Table III.1 of [52],
- $\frac{\chi}{\Gamma}$ the dispersion factor $(s.m^{-3})$
- BR the breathing rate $(m^3.s^{-1})$

For a time-dependent release, RG 1.183 [9] indicates that the following breathing rates should be considered :

- $BR = 3.5 \times 10^{-4}\ m^3.s^{-1}$ for the first 8 hours of the accident
- $BR = 1.8 \times 10^{-4}\ m^3.s^{-1}$ from 8 to 24 h following the accident
- $BR = 2.3 \times 10^{-4}\ m^3.s^{-1}$ for the rest of the duration of the accident

For a member of the public facing an instantaneous release, the considered breathing rate is $BR = 3.3 \times 10^{-4}\ m^3.s^{-1}$ which corresponds to light activity breathing rate for adults (20 liters of air per minute) and corresponds to the requirements of DOE-STD-3009-2014, Section 3.2.4.2.

9.3 Primary sodium coolant fire model

9.3.1 • Synthesizing Previous Findings: Potential of Blast and Aircraft Crash events to induce Primary Coolant Leaks

The blast and aircraft crash scenarios, detailed in Sections 6 and 7 respectively, were analyzed to assess their potential impact on the primary sodium coolant system.

In the case of distant blasts, the study established that, while these events could trigger cracks and potential collapse in reinforced concrete walls, such as those in Room B, the likelihood of inducing significant sodium leaks was deemed negligible in comparison to other scenarios under consideration.

Even if sodium leaks were to occur due to wall damage, the limited oxygen supply through resulting cracks would likely prevent sustained sodium combustion. A substantial explosion equivalent to at least 450 kg of TNT would be required to trigger wall collapse and partial release of primary sodium coolant activity.

Regarding contact blasts, it was determined that a minimum of 2 kg of TNT is necessary to breach Room B's 30 cm-thick wall, potentially leaving primary circuit piping vulnerable to sabotage. For breaches in Room A's 2m-thick reinforced concrete wall, a contact blast of at least 150 kg of TNT is required, classified as Beyond Design-Basis.

Aircraft crashes, examined in detail, differentiate between local and global effects on the targeted structure. While Room B with a 30cm-thick wall is vulnerable to collapse due to both local and global effects of certain aircraft crashes, Room A with its 2m-thick wall can withstand such impacts. The potential fire hazard posed by jet fuel post-crash is to be considered in conjunction with sodium leaks from the reactor's primary and secondary circuits in Room B.

The impact of jet fuel is also to be taken into account in the event sequence following an aircraft crash. It is estimated that about 50% of the jet fuel mass burns in the fireball, outsite of the containment building, and the rest in the pool fire, with fuel potentially reaching the "inside" of what is left of the building. This additional flammable substance is later to consider in tandem with the fire hazard posed by sodium leaks from the reactor's primary and secondary circuits in Room B.

9.3.2 • NRC Guidelines for Assessing Primary Coolant Radioactivity Release

Assumptions for evaluating the consequences of radioactivity release from the primary sodium coolant follows the instructions provided in NRC's Regulatory Guide 1.183, Appendix E [9] relating to a PWR main steam line break accident. Assumptions made are summarized in Table 25 below. It is noted that assumptions in Table 25 are quoted directly from the regulatory document without alteration. It might be argued that the regulation for PWRs is overly conservative and not appropriate for advanced reactors. Namely, assumptions are made to neglect sodium aerosol deposition in Room B debris, and elevation of the plume due to the sodium fire projection, which would result in a significantly lower dispersion factor (which should be reduced by several orders of magnitude). However, without being able to describe fully the scenario's event sequence and the amount of damage caused to Room B (varying from minor to complete wall collapse), RG 1.183's assumptions are conservative and generic assumptions are to be applied.

Table 25: Assumptions for evaluating the radiological consequences of a PWR main steam line break accident [9]

PWR Main Steam Line Break Accident	
Dose Criteria	25 rem TEDE
Analysis Release Duration	Instantaneous puff
Assumptions	• The total mass of coolant released should be assumed to be that amount in the steam line and connecting lines at the time of the break plus the amount that passes through the valves prior to closure. • All the radioactivity in the released coolant should be assumed to be released to the atmosphere instantaneously as a ground-level release. No credit should be assumed for plateout, holdup, or dilution within facility buildings.

9.3.3 • Radioactive Release from Sodium Pool Fires

In the context of a security scenario important enough to provoke a significant breach in Room B (partial or complete wall collapse) as previously described, the amplitude of the impact and the ejection of debris is likely to cause sodium leaks in some of the pipes of the Na/Na heat exchanger between the first and second loops. Knowing that the temperature of sodium in the first loop varies in the range 300 - 510 °C as described in Table 2 and that sodium self-ignition temperature in air is around 200°C, such a scenario would result in a sodium fire in Room B, releasing primary coolant radioactivity in the atmosphere.

Sodium fires being a focal point of safety analysis for Sodium Fast Reactors, the state of knowledge on release of radioactivity from a primary sodium coolant is summarized in the Argonne National Laboratory Mechanistic Source Term development plan [10]. The experimental results provided in this reference are used to quantify the transport of sodium activity and fission products (if fission products are present in the sodium coolant) from the primary reactor coolant to the containment atmosphere during a sodium fire.

In the case of partial or targeted leaks, these scenarios could lead to a sodium jet fire. In the event of a more sustained leak, a sodium pool fire should occur. These types of fire have very different kinetics, and might lead to different amounts radioactivity release from the coolant. As we are focusing on the worst maximum accidents and that a sodium pool fire involves more coolant, a sodium pool fire will be assumed in this section.

Much of what is known about sodium pool fires is described in previous work by Newman [53]. During a sodium pool fire, only a fraction of the products of the combustion process, sodium oxides, leave the pool surface as smoke. Newman measured the smoke fraction of sodium pool fires depending on the pool temperature, which is displayed in Figure 36(a). From 250°C to 600°C, the smoke fraction is relatively constant at approximately 0.11. A significant increase in the smoke fraction is observed from 600°C to 750°C, with the smoke fraction being 0.18 at 650°C, 0.25 at 700°C, and 0.34 at 750°C. Reasons for such an increase are provided in [10]. The release fraction of activated sodium (^{24}Na and ^{22}Na) would be the same as the non-activated sodium smoke fraction.

By considering the steady state temperature reached with a balance between the heat generated during the combustion process and the heat losses to the sodium pool and the surroundings, the maximum temperature of an unconfined burning sodium pool with unlimited oxygen is stated to be approximately 730°C [10]. In the experimental tests, sodium pool temperatures exceeding 730°C are maintained by external heating [53]. Not being aware of the specific geometry and conditions of the pool fire in our specific case, a conservative assumption is made that the pool temperature reaches 730°C, which is an unlikely outcome applied for a spill of sodium liquid coming from a leak, however large. The decision to stand at the limit of available experimental results in terms of sodium fire temperature also constitutes a necessary margin in taking into account the fact that additional flammable material, such as the fuel stored in the aircraft's tanks, might be involved in the event sequence.

Depending on the scenario, estimating the release fraction of additional isotopes, including sodium coolant activated impurities and fission products that might have migrated from the fuel to the primary coolant (in case of cladding breach for example), may be necessary. The current state of knowledge of the transport of isotopes other than ^{24}Na and ^{22}Na during a sodium pool fire focuses on ^{131}I, ^{137}I and

^{134}Cs, which accounted for the majority of activity found in the primary sodium of EBR-II and FFTF subsequent to pin failures. Experimental work by Sahoo et al. [54] and Kawahara et al. [55] provide release fractions of these isotopes depending on sodium pool temperature, oxygen concentrations and relative humidity of the atmosphere (21% oxygen and 70% relative humidity for Sahoo et al. [54] and 10% oxygen and 0% relative humidity for Kawahara et al. [55]). The results of release fractions from Kawahara et al. are shown in Figure 36(b). At 400°C, the cesium release fraction is approximately 40% and monotonically increases to approximately 70% at 600°C. It is important to note that the authors of these experiments only tested sodium temperatures up to 600°C, which is below the sodium pool temperature assumption made in the previous paragraph. If they had performed experiments at higher sodium pool temperatures, they may have seen similar behavior to that observed by Newman [53] where the release fraction dramatically increased at sodium pool temperatures exceeding 600°C.

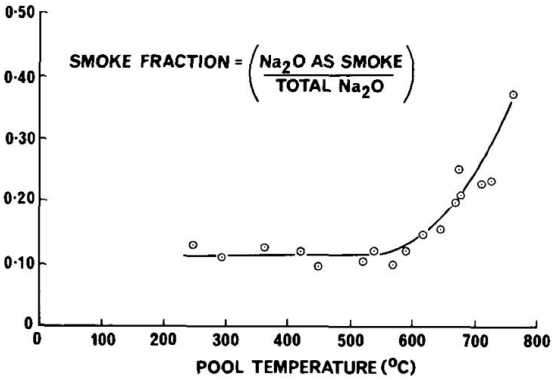

(a) Sodium fire smoke fraction depending on fire temperature, Newman [53]

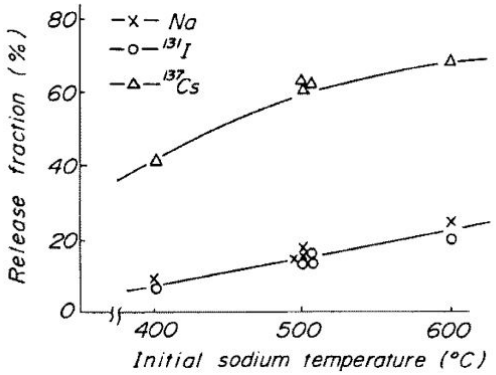

(b) Sodium fire release fraction depending of fire temperature, Kawahara et al. [55]

Figure 36: Sodium fire release fractions

In this specific sequence of events, and with the reactor operating under normal conditions before the attack, there is no indication that a breach in the cladding could have occurred in this scenario. Additional isotopes may originate from the filters of the first loop purification system. However, due to the limitations in accurately modeling this system, the potential release of radioactive products and activated products stores in the purifying system is neglected here.

Refinements on sodium fire dynamics The thermodynamics and release of a sodium fire are only roughly estimated here. In pool fires, phenomena like sodium oxides deposition on the sodium pool surface can be modeled and have self-extinguishing properties. This phenomenon is not expected for a sodium leak and would apply more to a fire in a pool, but it is difficult to draw conclusions at this stage. Codes to simulate sodium pool fires were developed in the past. More in-depth work is expected to be carried on this subject, with codes like SOFIRE II or NACOM.

9.3.4 • Primary Coolant Pool Fire: TEDE and Emergency Zones

In a worst-case scenario where the entire primary coolant inventory of Room B is involved in a large pool fire (approximately 170 L with an activity of 3×10^15 Bq, cf Section 2), and assuming an instantaneous release (using the Gaussian puff mode of Section 9.1.2) with a conservative smoke fraction of 0.3, the Total Equivalent Dose Exposure (TEDE) for a member of the public reaches a peak of 800 rem at a distance of 15 m from the reactor. The resulting TEDE at various distances from the reactor is illustrated in Figure 37, which also highlights the positions of the boundaries for the Low Population Zone (LPZ) and the Emergency Planning Zone (EPZ) by indicating when the dose falls below the threshold limits of 25 rem and 1 rem, respectively. The final sizes of the LPZ and EPZ zones are provided in Table 26.

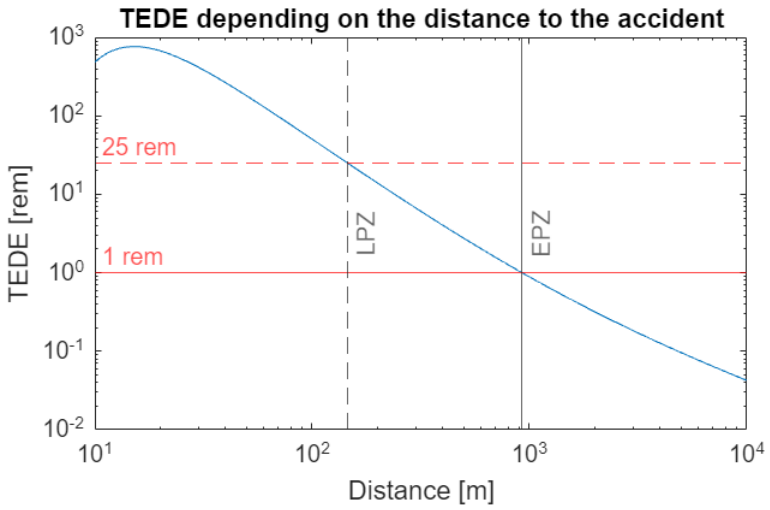

Figure 37: Public dose exposure to a primary sodium fire in Room B

Table 26: Site boundaries and time response for a primary sodium coolant fire scenario

Low Population Zone (LPZ) 25 rem dose limit	$146m$
Emergency Planning Zone (EPZ) 1 rem dose limit	$925m$
Maximal expected Intervention time	Not studied

It is noteworthy that both the Low Population Zone (LPZ) and the Emergency Planning Zone (EPZ) extend over considerable distances, spanning hundreds of meters (146m for the LPZ and 925m for the EPZ). The significant expansion of these zones, attributed to a seemingly minor event such as a coolant leak, underscores the substantial impact of high coolant activation, as previously highlighted as a key vulnerability of the reactor described in Section 2. However, it may be contended that the guidelines provided by the NRC for assessing the radiological consequences of such accidents are overly conservative, as they do not consider potential deposition in building debris or the elevation of the

plume due to generated heat, which could lead to a reduction in resulting dose by several orders of magnitude. Additionally, given the presence of a draining mechanism, it is improbable that a sodium fire would involve the entire primary coolant inventory in Room B.

In light of the extensive reach of the LPZ, there arises a fundamental challenge regarding the viability of deploying the SGTR in urban settings. However, addressing the vulnerability associated with coolant activation is feasible by relocating the primary heat exchanger to Room A, shielded behind a robust 2m reinforced concrete wall, effectively eliminating the risk of leakage triggered by any DBT. To optimize spatial constraints, integration of the primary heat exchanger with the reactor vessel structure could be explored. Alternatively, reinforcing Room B's structure or the exchanger piping, or introducing additional physical barriers, could mitigate the risk of DBTs causing substantial primary sodium leaks. While these proposed configurations entail additional costs, the findings underscore the importance of early consideration of consequence-based security in the design phase.

Given the current assumption that coolant activity is promptly released into the atmosphere, setting a maximal intervention time to restrict radioactivity release below 1 rem becomes irrelevant. To practically define a minimum intervention time, a much more precise and detailed analysis to quantify the various systems' leaks and sodium fire dynamics should be conducted. Besides, the ability of an intervention team to intervene on a radioactive sodium fire caused by an explosion or an aircraft crash in a matter of tens of minutes would require to be studied in more details.

9.4 Mechanistic Source Term (MST) assessment for a Prolonged Loss-of-Heat-Removal (PLHR)

As outlined in Section 5, the occurrence of a Prolonged Loss-of-Heat-Removal (PLHR) scenario can result from deliberate sabotage targeting the Reactor Cavity Cooling System (RCCS), such as obstructing air pipes or RCCS air inlet chimneys. This Section presents a detailed mechanistic assessment of the accident source term in case of a PLHR. Using a Mechanistic Source Term (MST) analysis, the objective is to realistically model the release and dispersion of radionuclides from the source to the surrounding environment during the various accident phases. This analysis is a crucial component expected to be included in the licensing process for advanced reactor designs.

9.4.1 • NRC Guidelines for a Mechanistic Assessment of LOCA Radioactivity Release

Assumptions for evaluating the radioactivity release of a PLHR follow the instructions provided in NRC's Regulatory Guide 1.183 Appendix A, relating specifically to a PWR loss-of-coolant (LOCA) accident [9]. The choice of relying to these assumptions stems from the fact that, as the reactor uses the same fuel as a PWR (UO_2), a certain number of assumptions are applicable to both studies. In particular, the requirement in terms of analysis duration derives from the half-life of ^{131}I, whose release plays a major role in determining the accident source term. The assumptions relevant to an advanced-reactor study are summarized in Table 27 below. It is noted that assumptions in Table 27 are quoted directly from the regulatory document without alteration. In particular, the NRC stipulates that the analysis of the release duration of a PLHR should extend to one month.

Table 27: Assumptions for evaluating the radiological consequences of a PWR LOCA accident [9]

PWR LOCA Accident	
Dose Criteria	25 rem TEDE
Analysis Release Duration	30 days for containment leakage
Assumptions	• Reduction in airborne radioactivity in the containment by natural deposition within the containment may be credited. • The primary containment should be assumed to leak at the peak pressure technical specification leak rate for the first 24 hours.

9.4.2 • PLHR Temperatures and Initial Conditions (ICs)

The evolution of reactor temperatures during a PLHR event (resulting in the incapacitation of the RCCS) has been analyzed by Kallieros et al. [11], with findings depicted up to one month in Figure 38. Following reactor shutdown, fuel temperature initially drops by 100K within a minute, then gradually increases due to the decay of short-lived fission products. Subsequently, an intermediate peak fuel temperature of 1350K is reached after 15 minutes, followed by a decrease over the next day. However, as the decay of longer-lived fission products advances, there is a global increase in reactor temperatures, with peak temperatures occurring approximately 40 days later, reaching approximately 1500 K for the fuel. For further details on the temperature evolution up to 60 days, refer to Figure 6

in Section 5.

It is assumed that the intrusion is detected: the reactor shuts down, the sodium coolant is fully drained from the vessel and replaced with inert gas. Initial conditions used in the analysis, along with default parameters of the code, are listed in Table 28.

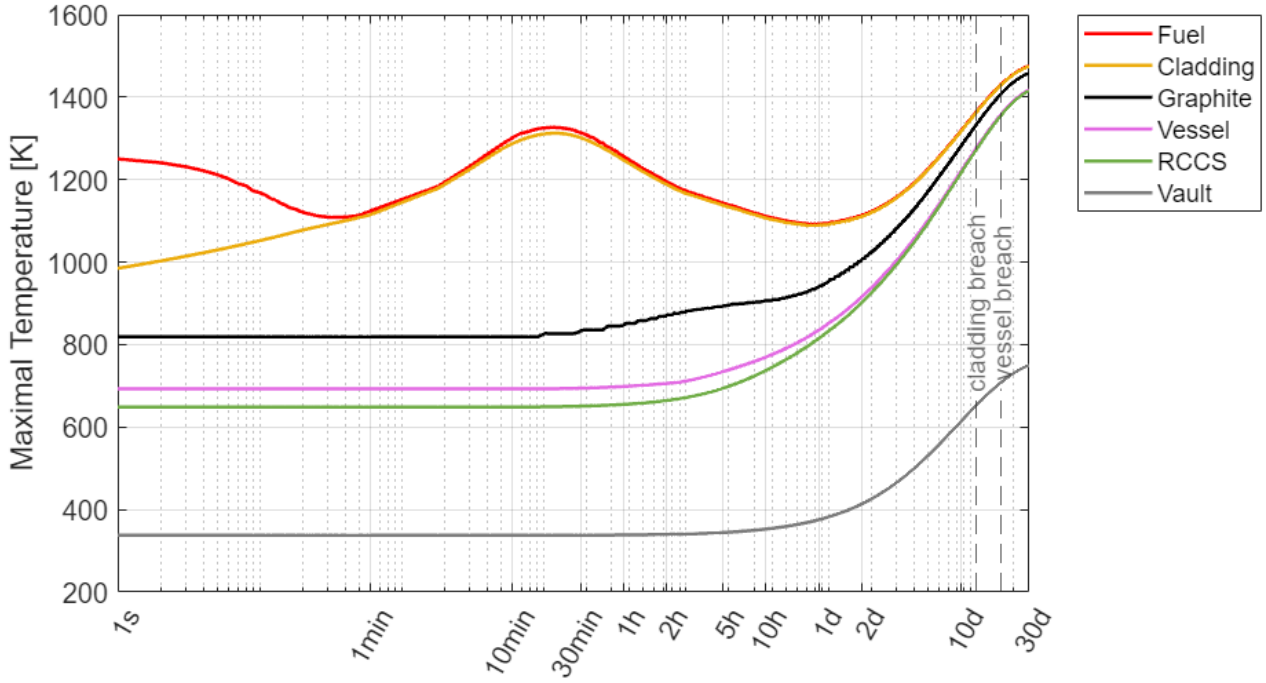

Figure 38: SGTR PLHR 1-month Temperatures Evolution

Table 28: MST Reference parameters and Initial operating conditions (ICs)

Parameter	**Reference Value**	**Reference**
Simulation time	1 month	RG 1.183 [9]
Cladding Strain to failure	2%	Section 9.4.7.1
Vessel Strain to failure	2%	Section 9.4.7.2
Vessel Design-Basis Leakage rate	0.1 vol%/day	Section 9.4.8.1
Containment Design-Basis Leakage rate	1 vol%/day	Section 9.4.8.2
Cladding internal initial pressure	0.4 $MPa = 4$ $bars$	
Vessel initial pressure	0.2 $MPa = 2$ $bars$	
Vault initial pressure	0.1 $MPa = 1$ bar	

9.4.3 • MST Analysis Code: Framework and User Manual

The MST analysis for a PLHR scenario involving the SGTR was conducted using the code described below. In an MST, a reactor is represented as a set of nested "compartments", modelling

the physical barriers separating the environment from radioactive sources. Nuclides are assumed to mix instantaneously and homogeneously throughout the volume of each compartment. Leakage rates simulate a cascade flow of radionuclides across these compartments towards the environment. If a compartment breaches, its radioactive inventory is automatically and fully discharged into the next one. At the end of the cascade, the resulting time-dependent source term released in the environment is finally translated into public dose exposure for a member of the public through an atmospheric dispersion model. The conceptual model describing the SGTR model for the MST assessment is described in Figure 39.

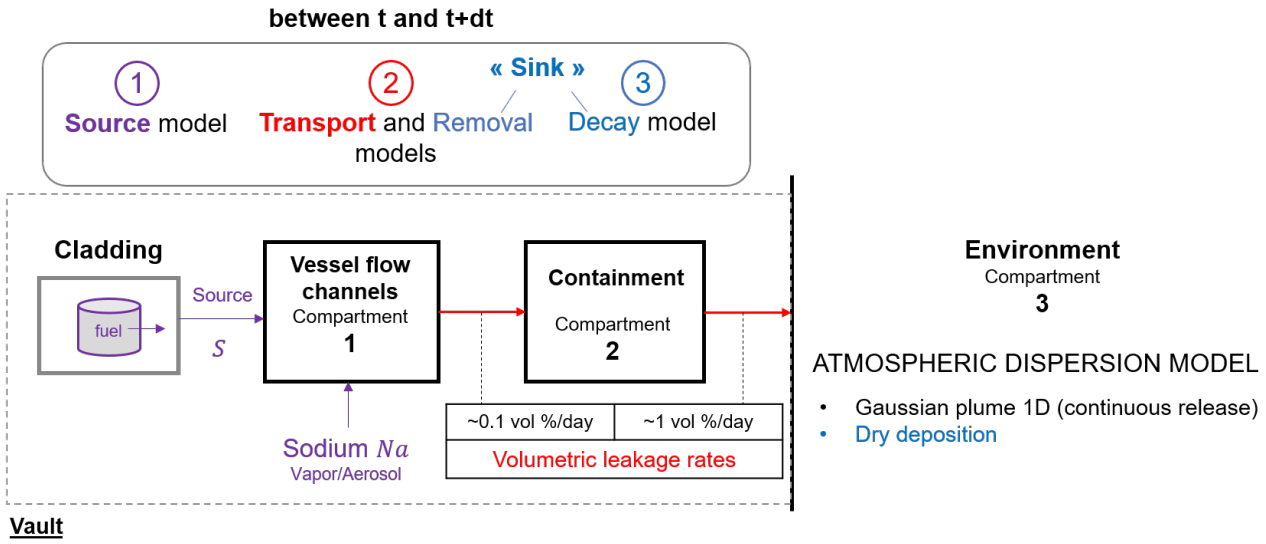

Figure 39: SGTR Compartments' modelisation

As illustrated in the flowchart, the three main processes to model in an MST are a **"Source"**, portraying the release of radionuclides in the reactor compartments, the pure **"Transport"** of nuclides from compartment to compartment, and a **"Sink"**, including various removal processes such as radioactive decay, deposition or adsorption. A "Sink" should take into account the possibility of re-volatilization of deposited or adsorbed nuclides depending on the constituents physical properties and of the current running conditions of the reactor. For each phenomenon simulated, conservative margins and uncertainties should either be taken into account in a qualitative or quantitative way. Determining an MST for transient event sequences involving complex phenomena requires therefore significant knowledge and modeling capabilities to accurately describe the chemical and physical interactions taking place in each compartment. Each of these phenomenon depends on chemical and physical conditions, and the reactor technology.

The modeling effort extensively leverages the existing documentation of the NRC codes RADTRAD [56] and MELCOR [57]. The Simplified Radionuclide Transport (SRT) code [58], developed by Argonne National Laboratory (ANL), and designed for MST assessment for pool-type, metal fuel sodium fast reactor (SFR), was also a major source of inspiration, particularly when it comes to interactions specific to a sodium environment.

The MST assessment code was developed in Matlab. The code folder structure is displayed in Figure 40. The folder *Initialisation* can be used to translate SERPENT depletion studies into a large table detailing the initial radionuclide inventories in the various reactor compartments. The table is later used in Transport and Decay equations, as explained in Section 9.4.6. The script *Mechanistic_Source_Term_Analysis.m* calls the set of functions from the folders *Functions* and models from the folder *Files* to carry out a deterministic MST with reference parameters. The list of default parameters is displayed in Table 28. Most of the code options are adjustable via the variable *opts*, and an overview of the options available is listed in Table 29. The script returns the plots displayed in the deterministic result Section 9.4.10. The script *Statistical_Analysis.m* conducts the same MST analysis several times, by considering the code inputs are random variables whose probability distributions are assessed in Section 9.4.11. The probability distributions of resulting zones in siting are assessed and the script returns 90% and 95% confidence intervals of EPZ and LPZ values along with the plots displayed in Section 9.4.11.

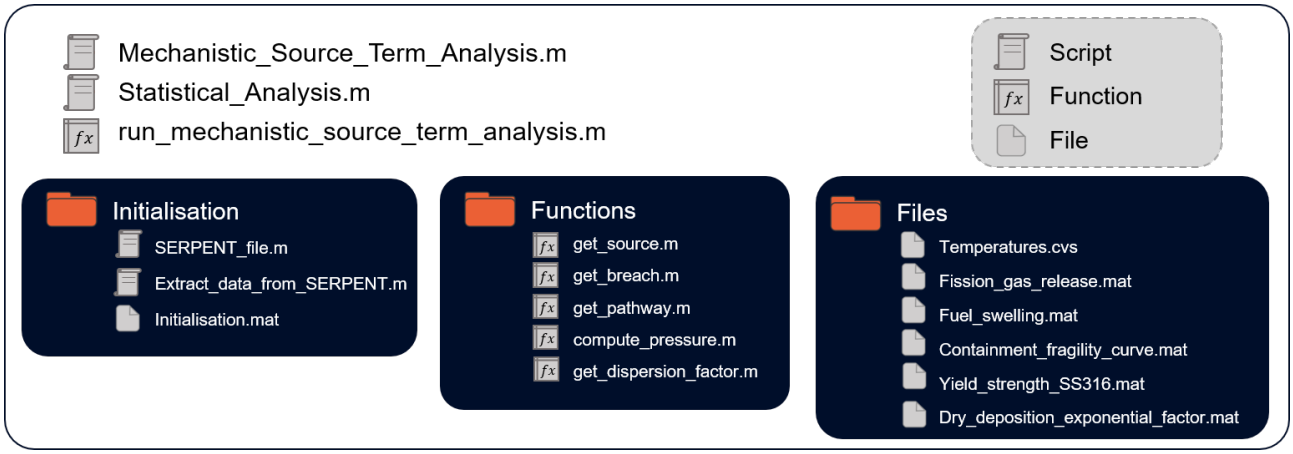

Figure 40: Mechanistic Source Term Analysis Code Structure

Table 29: MST code options

Option	**Variable**	**Value / Unit**
Simulation time	opts.T	seconds (s)
Simulation time-step	opts.dt1 - opts.T1 opts.dt2 - opts.T2 ...	seconds (s)
Decay	opts.decay opts.daugther_ingrowth	true - false true-false
Aerosol deposition	opts.aerosol_deposition	true - false
Dry deposition	opts.dry_deposition	true - false

9.4.4 • Time marching Method and Precision

The code developed utilizes Explicit Time Integration, solving Differential Equations by computing the solution at the next time step based explicitly on system conditions at the current time. The time

step varies, and the required precision for a selected period is determined manually at the beginning of the code.

The desired precision is achieved by manually adjusting the time step for different segments of the analysis, with smaller time steps chosen particularly for periods characterized by high temperature gradients. Smaller time-steps are also employed to better capture variations around singularities, such as cladding or vessel breach events. Additionally, a small time-step is essential for modeling the steel liner yield and resulting increased leakage rate of the containment building. The analysis involves time steps ranging from seconds near singular points to hours when system physical evolutions are slow.

To ensure the accuracy of a sample of simulations, a recommended approach is to run a default simulation with great precision and evaluate the gap with the corresponding sample simulation, which should remain acceptable. Coarse time-stepping can also be effectively identified by monitoring the concentrations of specific isotopes known for their sensitivity to decay. The discretization of differential equations may indeed lead to negative isotope inventories.

More advanced techniques exist to implement adaptative time-steps in MST codes. For instance, in the process of running a simulation at time t, RADTRAD [56] has the ability to calculate two solutions at t + dt : The first solution calculates the variations of physical values after an infinitesimal time dt, and the second solution uses two increments of dt/2. Precision levels can be quantified by comparing the relative differences between the two solutions calculated at t+dt and the time-step can therefore be tuned accordingly. This adaptation can be performed at every time step or at specified intervals, such as once every ten time steps. Although it ensures precision levels, such a solution is complex to implement and substantially increases computational times.

9.4.5 • Nuclide inventories, chemical and transport groups

The inventories of SGTR radionuclides have been assessed through SERPENT depletion studies and models for assessing the MAR in Section 2. The list of the 46 isotopes considered in the code, presented in Figure 41, follows the same assumptions made when assessing the MAR. More precisely, the considered isotopes include :

- All the isotoped listed in NUREG-1887, referred as the most important radionuclides in terms of health effects [12].
- Major contributors to the MAR according to SERPENT depletion results (meaning isotopes with activity larger than $10^5\ Ci = 3.7 \times 10^{15}\ Bq$), with a half-life screening of 0.5 day. With a cladding breach time estimated at approximately 10 days, this half-life screening of 0.5 days is justified. [6]
- Relevant isotopes necessary to model coolant activity.

[6] Even if it could be argued that decay is accounted for in the compartments and that a half-life screening should not be applied to the initial set of nuclides, the half-life screening first saves calculation time and it is added that as decay is not taken into account in the plume (meaning in the last compartment - the Environment), it would be unrealistic to simulate the dispersion of short-lived isotopes in the atmosphere. It is therefore concluded that a half-life screening process is necessary for this study.

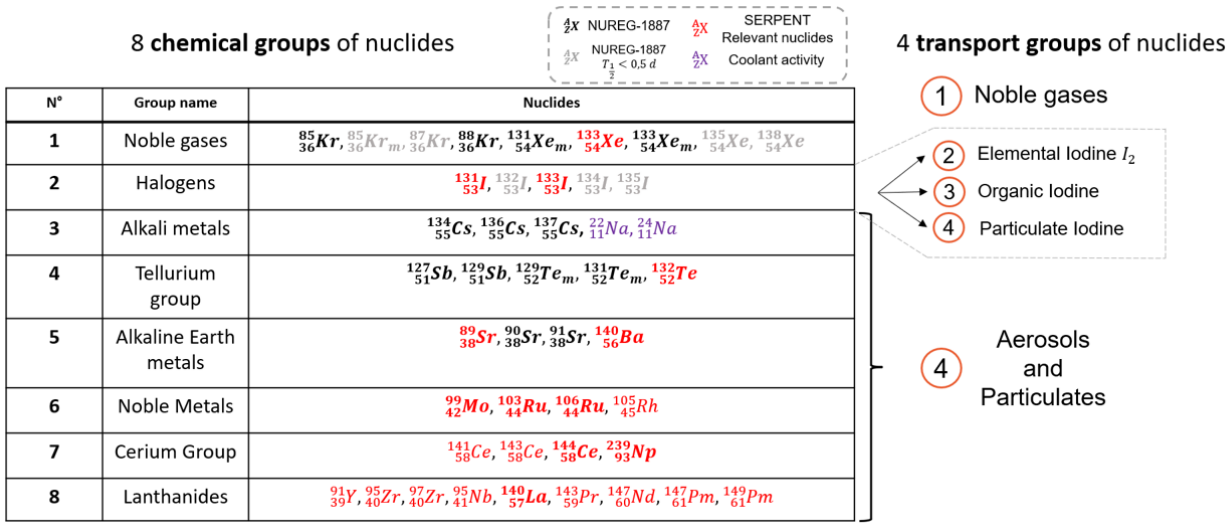

N°	Group name	Nuclides
1	Noble gases	$^{85}_{36}Kr$, $^{85}_{36}Kr_m$, $^{87}_{36}Kr$, $^{88}_{36}Kr$, $^{131}_{54}Xe_m$, $^{133}_{54}Xe$, $^{133}_{54}Xe_m$, $^{135}_{54}Xe$, $^{138}_{54}Xe$
2	Halogens	$^{131}_{53}I$, $^{132}_{53}I$, $^{133}_{53}I$, $^{134}_{53}I$, $^{135}_{53}I$
3	Alkali metals	$^{134}_{55}Cs$, $^{136}_{55}Cs$, $^{137}_{55}Cs$, $^{22}_{11}Na$, $^{24}_{11}Na$
4	Tellurium group	$^{127}_{51}Sb$, $^{129}_{51}Sb$, $^{129}_{52}Te_m$, $^{131}_{52}Te_m$, $^{132}_{52}Te$
5	Alkaline Earth metals	$^{89}_{38}Sr$, $^{90}_{38}Sr$, $^{91}_{38}Sr$, $^{140}_{56}Ba$
6	Noble Metals	$^{99}_{42}Mo$, $^{103}_{44}Ru$, $^{106}_{44}Ru$, $^{105}_{45}Rh$
7	Cerium Group	$^{141}_{58}Ce$, $^{143}_{58}Ce$, $^{144}_{58}Ce$, $^{239}_{93}Np$
8	Lanthanides	$^{91}_{39}Y$, $^{95}_{40}Zr$, $^{97}_{40}Zr$, $^{95}_{41}Nb$, $^{140}_{57}La$, $^{143}_{59}Pr$, $^{147}_{60}Nd$, $^{147}_{61}Pm$, $^{149}_{61}Pm$

Figure 41: Nuclide Inventory - Chemical and Transport groups

Figure 41 associates each isotope with a chemical and a transport group, depending on physico-chemical properties of the latter. The distribution of isotopes between chemical and transport groups is derived from RADTRAD [56]. As required by RG 1.183 [9], with the exception of elemental and organic iodine and noble gases, fission products are assumed to be in particulate form.

The nuclide inventory assessed by SERPENT depletion results is extracted and arranged in the form of a table displayed in Figure 42 which is the central object on which the code performs all its operations.

9.4.6 • Source, Transport and Decay equations

Every time-step, a source, transport, and decay model are applied to a singular "Nuclides" table, extracted from SERPENT depletion results and displayed in Figure 42. The source releases isotopes stored in radioactivity "storage" (such as the fuel or the activated coolant) to a set of compartments. Transport push them out of the system, towards the environment, and accounts for removal (meaning deposition) in each compartment. Radioactive decay is finally applied to every compartment. Decay and removal system form together the **"Sink"** described in the introduction of this section.

9.4.6.1 Source model

Fission products release rate NUREG-1465, "Accident Source Terms for Light-Water Nuclear Power Plants" [59] was published in 1995 by the NRC. NUREG-1465 presents a representative accident source term for a Design-Basis Loss of Coolant Accident (LOCA) for a boiling-water reactor (BWR) and for a pressurized-water reactor (PWR). These source terms are characterized by the composition and magnitude of the radioactive material, the chemical and physical properties of the material, and the timing of the release to the containment.

The core inventory release fractions, by radionuclide groups, for the gap release, early and late in-vessel damage phases are listed in Figure 43 for BWRs.

The partial applicability of these results to SGTR stems from the use of the same fuel (UO_2). Nevertheless, a number of differences must be taken into account :

- During a PLHR accident, and even with its primary coolant drained, SGTR's power level is not high enough for the decay heat to make UO_2 melt. Indeed, maximum fuel temperatures reach around 1500K, which remains below the melting point of UO_2. The possibility of a core meltdown corresponding to a "late in-vessel release" is therefore not applicable.
- Powers differing by several orders of magnitude, the temporal variations in temperature faced by the fuel, which is driving force in the diffusion of volatile fission products out of the fuel, also differ. Assuming these percentages of release coming from significantly more intense temperature slopes is therefore conservative.
- SGTR's burnup at end-of-cycle is also low compared to a BWR. Burnup, by impacting the mechanical integrity of the fuel, is also a secondary factor influencing the diffusion of fission product gases out of the fuel pellet. Once again, considering BWR release fractions at end-of-cycle is therefore conservative.

As outlined in Section 9.4.2, the peak fuel element temperature in the SGTR during a PLHR scenario is approximately 1500 K and is attained after about 40 days. Stainless steel 316 cladding breach occurs for a cladding temperature of around 1000 K. Early-in vessel release is considered to occur for a BWR at temperatures approximating 2000 K. It is assumed that for fuel temperature ranges between 1000 K and 2000 K, release rate fractions are scaled linearly between the gap-in release and the early in-vessel release.

It is noted that fuel elements, in the model, are not a classic compartment. Rather it is considered as "storage" of nuclides, which could be potentially released. In practice, it means that decay is applied to the amount of fission product stored in the fuel "storage" over time, but that when a fission product

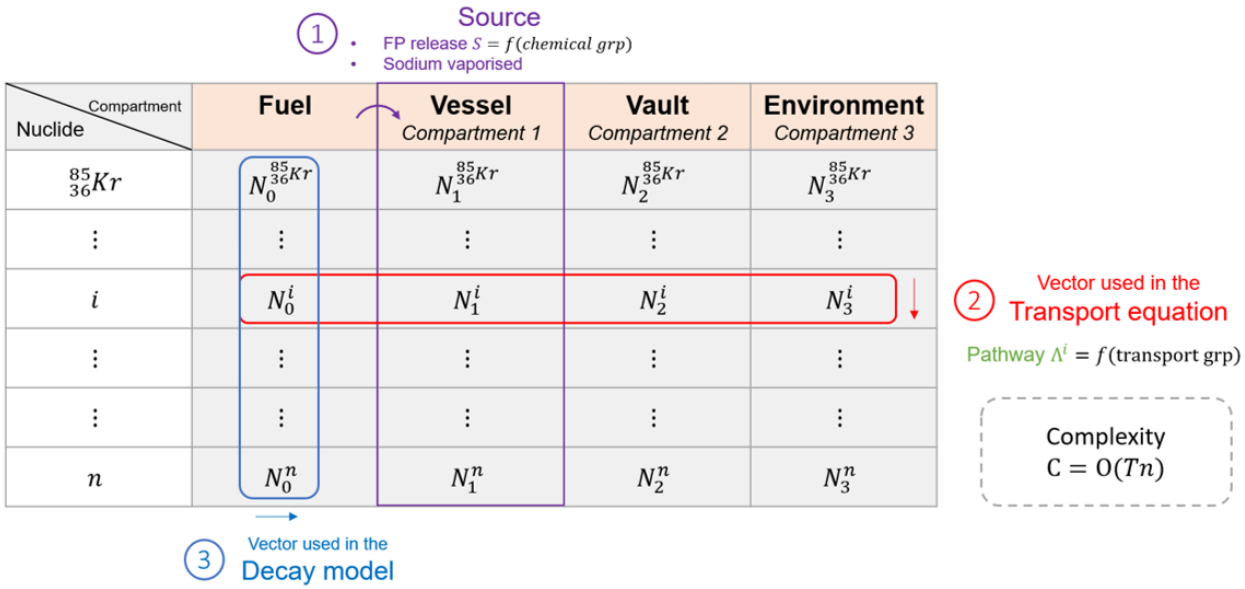

Figure 42: Nuclides' Table structure and algorithm

Table 1.3 BWR Event Timings and Fraction of Core Activity Inventory Released

Nuclide group	BWR core inventory release fraction		
	Cladding failure (gap release phase) (0.5 hr duration)	Core melt phase (in-vessel phase) (1.5 hr duration)	Post-vessel melt-through phase (ex-vessel phase) (3.0 hr duration)
Noble gases (Kr, Xe)	0.05	0.95	0
Halogens (I, Br)	0.05	0.25	0.30
Alkali metals (Cs, Rb)	0.05	0.20	0.35
Tellurium group (Te, Sb, Se)	0	0.05	0.25
Barium, strontium (Ba, Sr)	0	0.02	0.1
Noble metals (Ru, Rh, Pd, Mo, Tc, Co)	0	0.0025	0.0025
Cerium group (Ce, Pu, Np)	0	0.0005	0.005
Lanthanides (La, Zr, Nd, Eu, Nb, Pm, Pr, Sm, Y, Cm, Am)	0	0.0002	0.005

Reference: Table 3-12 from NUREG-1465 (Soffer et al. 1995)

Figure 43: Fission products (FP) releases rates for each phase of a BWR LOCA

is released to the vessel, it is not removed from that storage. Therefore, if one additional % of fission products is released from the fuel, this percentage applies to the original amount (with decay) and not to the remaining amount of nuclides.

Evaporated sodium release rate Even if it is assumed that sodium is drained (by gravity) from the vessel as described in Section 1.4, a significant amount of sodium will be retained in the vessel because of viscosity and capillarity forces. This amount of sodium will partially be vaporised in the vessel, and part of the activated sodium will leak to the atmosphere.

It is assumed that, at given pressure and temperature, sodium is at saturation level in the vessel. The partial saturation pressure of sodium depending on temperature is taken from the website Thermal Fluid Centrals [60]

$$p_{Na} = exp(-57.346 + 0.18129T - 2.2487.10^{-4}T^2 + 1.5164.10^{-7}T^3 - 5.2957.10^{-11}T^4 + 7.5006.10^{-15}T^5) \quad (84)$$

with :

- p_{Na} the partial pressure of sodium (10^2 Pa),
- T sodium temperature (K),

The amount of sodium corresponding to this saturation pressure is then computed and the share $\frac{n_{Na}}{n^i_{Na}}$ of radioactivity present in the sodium is released to the vessel.

$$n_{Na} = \frac{p_{Na} V_{Na}}{R T_{Na}} \tag{85}$$

A time dependant ^{22}Na and ^{24}Na source is computed by differentiating Equations (84) and (85). It also means that if temperatures decrease in the reactor vessel, sodium vapor condensates, and respective shares of sodium radioactive isotopes are removed from the compartment. As explained for the fuel, the liquid sodium is handled as a radioactivity "storage".

9.4.6.2 Transport and removal models

Transport equations implemented in this code are taken from RADTRAD [56].

The governing transport equations used are balance first-order linear differential equations relating to the transfer of radionuclides among compartments and the removal of radionuclides within a given compartment. As the release of nuclides is handled in a different "Source" model described above, the equations used in the Transport model alone are generic transport equations without source term, or 0-dimensional diffusion equations between scattered locations. However, with the "Source" model, the general evolution of the code follows a generic transport equation with source term, described below. It is reminded that within each compartment except the environment, the radionuclides that are airborne within that compartment are assumed to be uniformly distributed or mixed.

As shown in Figure 42, the Transport model is applied to every line of the "Nuclides" Table, meaning that one transport equation is applied to every nuclide. The coefficients used in these equations depend on the corresponding nuclide transport group, given in Figure 41, and quantify the leakage of this isotope from a compartment to another and its propensity for being deposited.

The transport of an isotope i from a compartment x to other connected compartments y is given by:

$$\forall\ nuclide\ i, \forall\ compartment\ x, \frac{dN_x^i}{dt} = S_x^i + \sum_{compartment\ y} \Pi_{x,y}^i N_y^i \tag{86}$$

with

- N_x^i the number of atoms of isotope i in compartment x ($atom$),
- $\Pi_{x,y}^i$ the transfer rate of nuclide i from compartment y to x (s^{-1}),
- S_x^i the release rate of atoms of isotope i released in compartment x ($atom.s^{-1}$), which is handled by the "Source" model.

To take transport into account in the whole structure and not only related to a single compartment, Equation (86) can be vectorised. The matrix Equation (87) is the general equation modelling the transport of one nuclide i through a set of compartments.

$$\forall\ nuclide\ i \in [\![1; n]\!], \begin{pmatrix} \dot{N}_1^i \\ \vdots \\ \dot{N}_x^i \end{pmatrix} = \begin{bmatrix} S_1^i \\ \vdots \\ S_x^i \end{bmatrix} + \begin{pmatrix} \Pi_{1,1}^i & \dots & \Pi_{1,x}^i \\ \vdots & \ddots & \vdots \\ \Pi_{x,1}^i & \dots & \Pi_{x,x}^i \end{pmatrix} \begin{pmatrix} N_1^i \\ \vdots \\ N_x^i \end{pmatrix} \tag{87}$$

In practice, with 3 compartments connected in series, radioactive sources being localised in the first one (the vessel), and by taking the conservative assumption that one nuclide once released can only by transported outwards of the reactor core, the equation applied to every line of the "Nuclides" Table is as follows :

$$\forall\ nuclide\ i \in [\![1;n]\!],\ \begin{pmatrix} \dot{N}_1^i \\ \dot{N}_2^i \\ \dot{N}_3^i \end{pmatrix} = \begin{pmatrix} S_1^i \\ 0 \\ 0 \end{pmatrix} + \underbrace{\begin{pmatrix} \Pi_{1,1}^i & 0 & 0 \\ \Pi_{2,1}^i & \Pi_{2,2}^i & 0 \\ 0 & \Pi_{3,2}^i & 0 \end{pmatrix}}_{\Pi^i} \begin{pmatrix} N_1^i \\ N_2^i \\ N_3^i \end{pmatrix} \tag{88}$$

The matrix Π is referred to as the **Pathway** matrix. Its coefficients account for both transfer from a compartment to the next one and removal models in a compartment or between two compartments (modeling a filter for example). As shown in Equation (89), Π can therefore be expressed as a sum of two matrices : One accounts for pure transport, which respects mass conservation and the other one accounting for removal models.

$$\Pi^i = \begin{pmatrix} \Pi_{1,1}^i & 0 & 0 \\ \Pi_{2,1}^i & \Pi_{2,2}^i & 0 \\ 0 & \Pi_{3,2}^i & 0 \end{pmatrix} = \underbrace{\begin{pmatrix} \Lambda_{1,1}^i & 0 & 0 \\ \Lambda_{2,1}^i & \Lambda_{2,2}^i & 0 \\ 0 & \Lambda_{3,2}^i & 0 \end{pmatrix}}_{Transport\ matrix} + \underbrace{\begin{pmatrix} -\lambda_{1,1}^i & 0 & 0 \\ 0 & -\lambda_{2,2}^i & 0 \\ 0 & -\lambda_{3,2}^i & 0 \end{pmatrix}}_{Removal\ matrix} \tag{89}$$

An actual 0-dimensional diffusion model ? Discussion was held on whether or not to implement a transport model based on a diffusion model rather than a cascade chain, where nuclides do not just move outwards. In a diffusion model, the equilibrium solution between two compartments would be for both compartments to have the same quantity of nuclides. In a cascade model, after an infinite time, the original compartment is completely emptied of nuclides. If considering a diffusion model between Compartments 1 and 2, the Transport matrix would have the following form :

$$\Lambda^i = \begin{pmatrix} \Lambda_{1,1}^i & -\Lambda_{2,1}^i & 0 \\ \Lambda_{2,1}^i & \Lambda_{2,2}^i & 0 \\ 0 & \Lambda_{3,2}^i & 0 \end{pmatrix} \tag{90}$$

However, in addition to a simple concern of conservatism, it was argued that in an accidental situation if nuclides were to leak from a compartment, it was probably because this event was driven by a physical reason (such as a pressure differential) rather than by simple diffusion, and that it would make no sense to consider that they could re-enter the original compartment. If compartments in derivation were to be added to the model, such as Room B for example, the diffusion model similar to Equation (90) would nevertheless make more sense, and in case of pressure difference, dissymmetrical diffusion coefficients can be assessed. The implementation of a cascade transport model highlights the importance of the "Sink" model in the MST : Without it, no nuclide retention is accounted for in the reactor and everything ends up at some point in the Environment.

Transport matrix Λ^i The transport matrix accounts for the transfer of nuclides between compartments. Mass conservation condition can be expressed as a condition on the column of the Transport matrix Λ^i :

$$\forall l \in [\![1;x]\!], \sum_k \Lambda_{k,l} = 0 \tag{91}$$

In practice, the set of equations describing the pure transport of nuclides in the cascade sequence from Compartment 1 to Compartment 3 is as below :

$$\begin{cases} \dot{N}_1^i = -\Lambda_{2,1} N_1^i \\ \dot{N}_2^i = \Lambda_{2,1} N_x^i - \Lambda_{3,2} N_2^i \\ \dot{N}_3^i = \Lambda_{3,2} N_x^i \end{cases} \tag{92}$$

Mass conservation in the set of equations (92) can be modeled by the two conditions given below :

$$\begin{cases} \Lambda_{1,1}^i = -\Lambda_{2,1}^i \\ \Lambda_{2,2}^i = -\Lambda_{3,2}^i \end{cases} \tag{93}$$

Indeed, mass conservation for a pathway from Compartment 1 to Compartment 2 has to ensure that the amount of nuclides leaving Compartment 1 ($-\Lambda_{1,1}^i N_1^i$) is equal to the amount of nuclides reaching Compartment 2 ($\Lambda_{2,1}^i N_1^i$).

As the primary coolant is considered to be drained and replaced by inert gas, every compartment is mainly filled by a gaseous phase, and the transfer rates from Compartment 1 to Compartment 2 $\Lambda_{2,1}$ and from Compartment 2 to Compartment 3 $\Lambda_{3,2}$ can both be expressed in terms of volumetric leakage rates, measured in *volume % / day*.

Based on orders of magnitude used in the industry and of the example provided in the presentation of the ANL SRT code [58], a conservative design-basis leakage rate from the Vessel (Compartment 1) to the Vault (Compartment 2) is assumed to $l_{1\to2} = 0.1$ *vol% / day*.

Requirements concerning the design-basis leakage rate of the nuclear containment buildings (here referred as the "Vault") and nuclear power plant control of containment leak tightness are set by the Code of Federal Regulations Appendix J. A maximum leakage rate inferior to 1 *vol% / day* is consistent with Appendix J requirements [61]. Therefore, a Design-Basis leakage rate of $l_{2\to3} = 1$ *vol% / day* is assumed from the Vault (Compartment 2) to the Environment (Compartment 3).

By solving the set of equations (92) the volumetric leakage rate can be expressed in terms of transfer rate as follows :

$$l_{x\to y} = 1 - e^{-\int_0^{1\ day} \Lambda_{y,x}(s)ds} \tag{94}$$

When assuming that the transfer rate is constant $\Lambda_{x,y} = constant$, the Transport matrix terms are finally given by Equation (95) and the mass conservation conditions in Equation (93). It is assumed here that the values of the Transport matrix do not depend of physico-chemical properties of the considered isotope : every volatile isotope is assumed to be transported in the same way accross the reactor compartments.

$$\Lambda_{y,x} = \frac{-ln(1 - l_{x\to y})}{1\ day} \tag{95}$$

Pressure and temperature dependant leakage rates The assumption $\Lambda_{x,y} = constant$ is incorrect. Indeed transfer rates vary with compartment pressures and temperatures. In practice, Equation (95) is still used in the code, but the the influence of pressures and temperatures on volumetric leakage rates is assessed. The current state of knowledge does not allow to express precisely the temperature dependency of nuclear-grade metallic seals but the assumption that $l_{1\to2} = 0.1\ \%\ /\ day$ until cladding breach, is being overly conservative so the reasoning still holds.

As for the Vault leaking rate $l_{2\to3}$, the assessment of the pressure and temperature dependency of PWRs containment building in case of severe accident has been the focus of 25 years of research and has been implemented in MELCOR [61]. This dependency presents a number of non-linearities, pointing to the breach in the containment steel liner.

Removal models λ^i The diagonal terms $\lambda_{k,k}$ in the Removal matrix account for removal models in a compartment. The non-diagonal terms $\lambda_{3,2}$ accounts for removal in the pathway between the Vault and the Environment, which can model a filter for example. Information on the filters in place and their configuration not being available, the conservative assumption $\lambda^i_{3,2} = 0$ is made.

Removal models can be assessed via a number of parameters : a decontamination factor DF, an efficiency η, or a removal coefficients λ (s^{-1}). the relationship between these coefficients and the mass fraction remaining in the volume after the removal process is as follows :

$$\frac{m(t)}{m(0)} = \frac{1}{DF} = 1 - \eta = e^{-\lambda t} \tag{96}$$

with :

- $\frac{m(t)}{m(0)}$ the mass fraction remaining in the volume after the removal process
- DF the decontamination factor
- η the removal efficiency
- λ the removal coefficient (s^{-1})

In this study, to remain consistent with the exponential form of the transport model, removal models are expressed in terms of removal coefficients.

Removal models that can be implemented in an MST include : natural deposition of aerosols and particulates, adsorption (chemisorption and physisorption), and filters.

Aerosol natural deposition is modeled upon consideration that sedimentation is the dominant phenomenon observed. Henry's correlation for aerosol deposition (Equation (97), described in RADTRAD [56]) is implemented in the code for aerosols and particulates.

$$\lambda = C_1 \frac{h_{ref}}{h} \frac{\rho_P}{\rho_{Pref}} \rho_A^K \tag{97}$$

with :

- $h_{ref} = 5\ m$,

- h the fall height (m). In the case of the Vessel, the height considered is the heights of flow channels. Concerning the Vault, the height considered is the height of the ceiling.
- $\rho_{Pref} = 2270\ kg.m^3$, the theoretical sodium oxide particle density.
- ρ_P the particle density, which should take into account porosity and potential moisture.
- ρ_A the aerosol mass in the compartment volume ($kg.m^{-3}$),
- $C1$ and K are experimentally-determined coefficients. If $\rho_A < 6.0 \times 10^{-5}\ kg.m^{-3}$, $C1 = 0.0016$ and $K = 0.33$. Else, $C1 = 0.0220$ and $K = 0.60$.

It is noted that Henry's correlation applies to an aerosol, i.e. a molecular bundle, which must be reflected in the code as a removal process applied to elemental isotopes. The precise application of Henry's correlation requires knowledge on the dominant aerosol species, which will likely dictate the overall behaviour of aerosols in the compartment. For SGTR and its compartments filled up with inert gas, the dominant aerosol species is typically pure sodium. Therefore, the density of pure sodium aerosol is used in the calculation. Sodium compounds have theoretical densities above 2,000 $kg.m^{-3}$, but their aerosol form is very porous and results in a density closer to $\rho_P = 400 kg.s^{-1}$ as assessed in [62].

Adsorption processes (chemisorption and physisorption) depend on specific interactions between molecules and the substrate. MELCOR [57] models the chemisorption of molecular forms of cesium and iodine specific to a humid environment, like CsI, $CsOH$, HI or I_2 on stainless steel. However, due to lack of data, models of chemisorption of sodium based molecules and aerosols are not available, and is therefore not treated in the analysis. That being said, according to [63], Moormann et al. have experimentally quantified adsorption of noble gases, cesium and iodine in the case of High Temperature Gas-cooled Reactors (HTGR). In that case, adsorption on stainless steel is measured to be significantly higher than on graphite. If more in-depth work is to be carried out later on adsorption, stainless steel adsorption should therefore be assessed in priority compared to graphite.

9.4.6.3 Decay model

As shown in Figure 42, the decay model is applied to every column of the "Nuclides" Table, meaning that is applied to every compartment.

In a compartment x, the decay and daughter in-growth of an isotope i is given by:

$$\forall\ compartment\ x, \forall\ nuclide\ i, \frac{dN_x^i}{dt} = \underbrace{-\lambda_i N_x^i}_{Decay} + \underbrace{\sum_{nuclide\ j} \beta_{i,j}\lambda_j N_x^j}_{Daughter in-growth} \tag{98}$$

with :

- N_x^i the number of atoms of isotope i in compartment x ($atom$),
- λ^i the decay constant of nuclide i (s^{-1}),
- $\beta_{i,j}$ the fraction of nuclide j that decays to nuclide i

- λ^j the decay constant associated with $\beta_{i,j}$ (s^{-1}),

To take all nuclides considered in the code and listed in Figure 41 into account, Equation (98) can be vectorised. the vector Equation (99) is the general equation modelling the decay and daughter in-growth of nuclides in a compartment.

$$\forall\ compartment\ x \in [\![1;3]\!],\ \begin{pmatrix} \dot{N}_x^1 \\ \vdots \\ \dot{N}_x^n \end{pmatrix} = \underbrace{-\begin{pmatrix} \lambda_1 & 0 & 0 \\ 0 & \ddots & 0 \\ 0 & 0 & \lambda_n \end{pmatrix}\begin{pmatrix} N_x^1 \\ \vdots \\ N_x^n \end{pmatrix}}_{Decay} + \underbrace{\begin{pmatrix} \beta_{1,1}\lambda_1 & \dots & \beta_{1,n}\lambda_n \\ \vdots & \ddots & \vdots \\ \beta_{n,1}\lambda_1 & \dots & \beta_{n,n}\lambda_n \end{pmatrix}\begin{pmatrix} N_x^1 \\ \vdots \\ N_x^n \end{pmatrix}}_{Daughter\ in-growth} \tag{99}$$

Daughter in-growth In this code, only the beta-linked decay of the considered fission products (FP) is taken into account, following the decay chains displayed in Figure 44. In practice, it means that in Equation (99), for nuclide j decaying in nuclide i, $\beta_{i,j} = \delta(i,j)$, with δ the Kronecker symbol. During analysis, due to daughter ingrowth, the concentration of certain isotopes increases rather than decreases. This is the case for the isotopes ^{140}La and ^{147}Pm as shown in Figure 45.

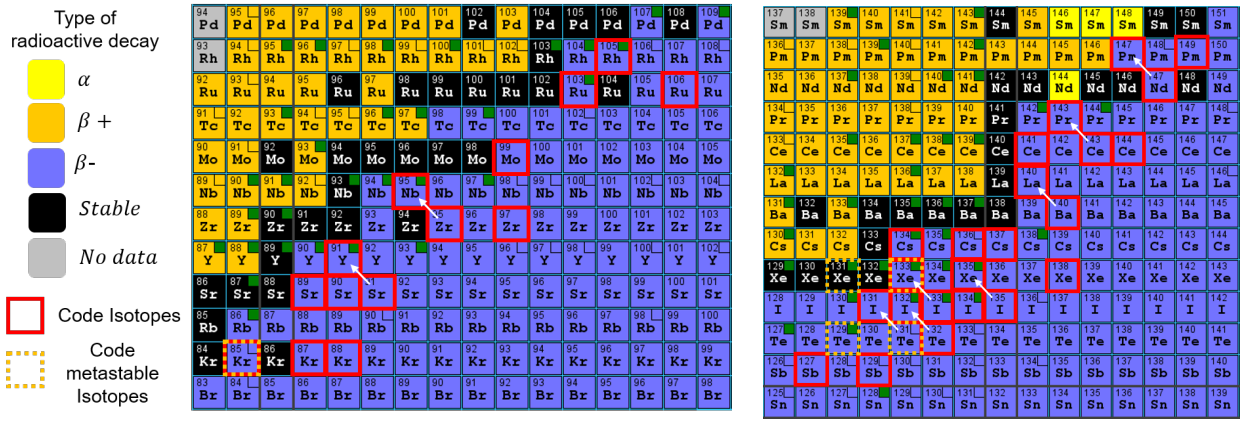

(a) (b)

Figure 44: Code considered Decay Chains

9.4.7 • Compartment breach

Physical barrier breach plays a major role in the release of radioactivity during an accident event sequence. Every time a barrier breaches, it is assumed that all nuclides contained in the associated compartment are instantly discharged to the next one. This phenomenon has a strong influence on the final release and is a major time marker defining before which external intervention must take place. For the studied scenario, creep is determined as the limiting factor dictating compartment breach time. Compartment creep rates are assessed based on their temperature and applied stress, depending on inner pressure and geometry. A compartment inner pressure is determined by using the perfect gas law expressed below, and accounting for the relevant gas release / leakage phenomena :

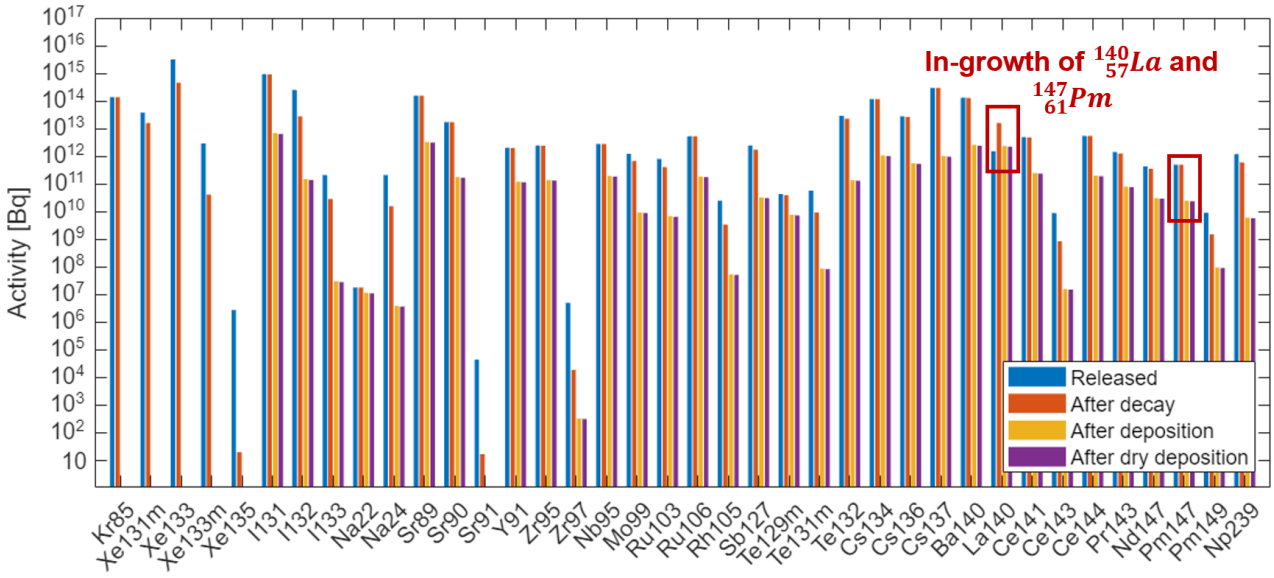

Figure 45: Notable Daughter In-growth of ^{140}La and ^{147}Pm over the PLHR analysis

$$\frac{dP}{dt} = \frac{nR}{V_s}\frac{dT}{dt} + \frac{RT}{V_s}\frac{dn}{dt} \tag{100}$$

with :

- P the compartment internal pressure (Pa),
- T the compartment internal temperature (K),
- n the amount gas in the comparment (mol),
- V_s the comparment volume,
- $R = 8.314\ J.mol^{-1}.K^{-1}$, the perfect gas constant,

9.4.7.1 Cladding breach

Cladding internal pressure rise during the accident is assessed by taking into account fission gas release from the fuel and fuel swelling. Indeed, during an accident involving loss of heat-removal, the temperature of the fuel rises, releasing fission gases trapped in the fuel, and expanding the helium contained in the cladding. The internal pressure of the cladding rises, imposing hoop and axial stresses, until the cladding ruptures as a result of the creep.

Cladding internal temperature is conservatively assumed to be equal to fuel temperature. Fission gas release and fuel swelling for UO_2 fuel depending on temperature and burnup is extracted from experimental results presented in references [64] and [65], respectively. The experimental data is extracted and interpolated to obtain maps displayed in Figures 46(a) and 46(b). Fuel swelling is first assessed depending on nominal operation temperature and burnup to compute the new gap-in volume. The conservative assumption that cladding creep does not impact the gap-in volume is made. Then

during the accident, the internal cladding pressure is assessed by accounting for temperature evolution and fission gas release (FGR) by applying the perfect gas law in Equation (100).

It is noted that, in our case, Fission gas release (FGR) and Fuel Swelling are considered as independent phenomena since, for low burnups, the fuel swelling observed is mostly due to solid fission products accumulating in the fuel pellet rather than fission gases. It is also noted that the data from Figures 46(a) and 46(b) was obtained for experiments under constant conditions and that deviation should be expected when applying them to transients.

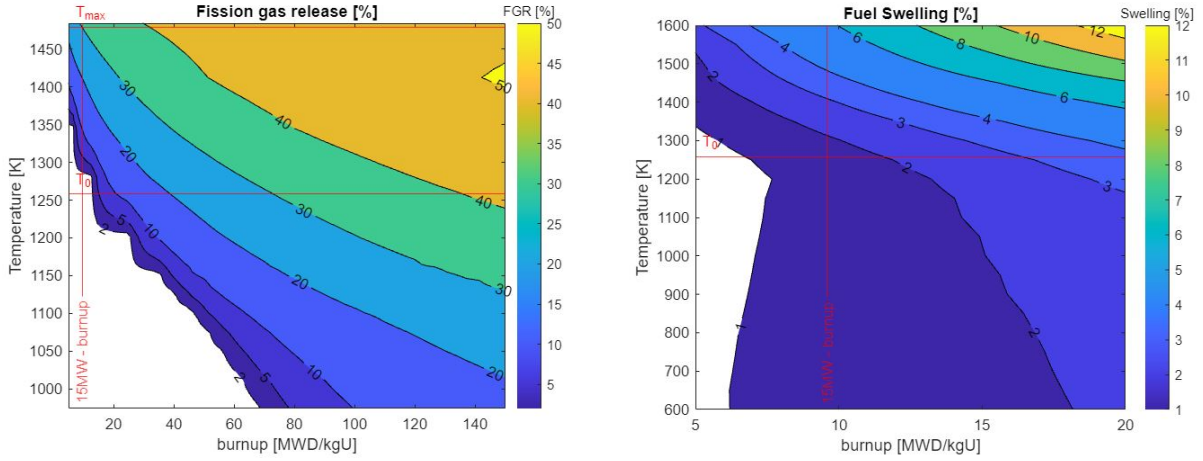

(a) Fission gas release (FGR) depending on temperature and burnup

(b) Fuel swelling depending on temperature and burnup

Figure 46: Extrapolation of experimental data : Fuel Fission gas release (FGR) and swelling

The hoop stress applied to the cladding, proportional to the pressure difference between the cladding and the flow channel, is assessed in Equation (101). The secondary creep rate of niobium stabilized 20%Cr - 25%Ni stainless steel AGR cladding is assessed in [66] and reported in Equation (102).

$$\sigma_h = (P_{cladding} - P_{vessel})\frac{r}{w} \tag{101}$$

with :

- σ_h the cladding hoop stress (MPa),
- $P_{cladding}$, P_{vessel} the cladding internal presure and the flow channels pressure respectively (MPa),
- $r = 7.03\ mm$ the cladding radius (mm),
- $w = 0.35\ mm$ the cladding thickness (mm),

$$\dot{\epsilon} = 181\ (s^{-1}.MPa^{-5}) \times \sigma^5 exp(-\frac{3.5 \times 10^5\ (J.mol^{-1})}{RT}) \tag{102}$$

with :

- $\dot{\epsilon}$ the cladding creep rate $(mm/mm.s^{-1})$,
- σ the cladding hoop stress (MPa),
- T the cladding temperature (K),
- $R = 8.314\ J.mol^{-1}.K^{-1}$,

Creep strain is calculated by integrating Equation (102). Cladding breach is determined by taking a reference creep strain to failure of $\epsilon_f = 2\%$. During a PLHR, cladding is assessed to breach after 12.6 *days*. Cladding pressure and creep strain are shown in Figure 47.

In the code, cladding breach is considered as a singular event, and the temperature used to compute it is the maximal temperature of all cladding pins. In practice, off-centered pins in the core are subjected to lower temperatures and should not be breached as fast as the ones in the center.

9.4.7.2 Vessel breach

The same procedure as for the cladding is applied to determine the breach time of the vessel. The vessel creep rate is based on the assessment of SS316 creep rate made in [67] and reported in Equation (104). Vessel internal pressure is calculated by applying the perfect gas law to a system assumed perfectly sealed and isochoric, and Vault internal pressure is conservatively assumed to remain around 1 bar. Reference creep strain to failure is also assumed to be conservatively $\epsilon_f = 2\%$. During a PLHR, vessel breach occurs after 19.1 *days*. Vessel pressure and creep strain for this analysis are displayed in Figure 47. It is noted that obtained results depend strongly on the vessel geometry (namely the diameter / thickness ratio).

The flow channels hoop stress is calculated as follows:

$$\sigma_h = (P_{vault} - P_{vessel})\frac{r}{w} \tag{103}$$

with :

- σ_h the vessel hoop stress (MPa),
- $r = 1.2\ m$ the vessel radius,
- $w = 0.04\ m$ the vessel thickness,

Depending on vessel hoop stress σ_h (MPa) and inner vessel temperature T (K), the vessel creep rate $\dot{\epsilon}$ $(mm/mm.s^{-1})$ is calculated base on the correlation developed in [67]:

$$\begin{aligned}\dot{\epsilon} =& exp(\frac{-6.885}{T^2} + \frac{136768}{T} - 77.6944) \\ & \times sinh((4.08T^2 - 7034.08T + 3077600) \times 10^{-7}\sigma_h)^{(1.17T^2 - 2498T + 1374011)\times 10^{-4}}\end{aligned} \tag{104}$$

In Figure 47, it is noted that pressure calculation has a physical sense only before compartment breach. After a vessel breach, the pressure is expected to equalize in all reactor compartments.

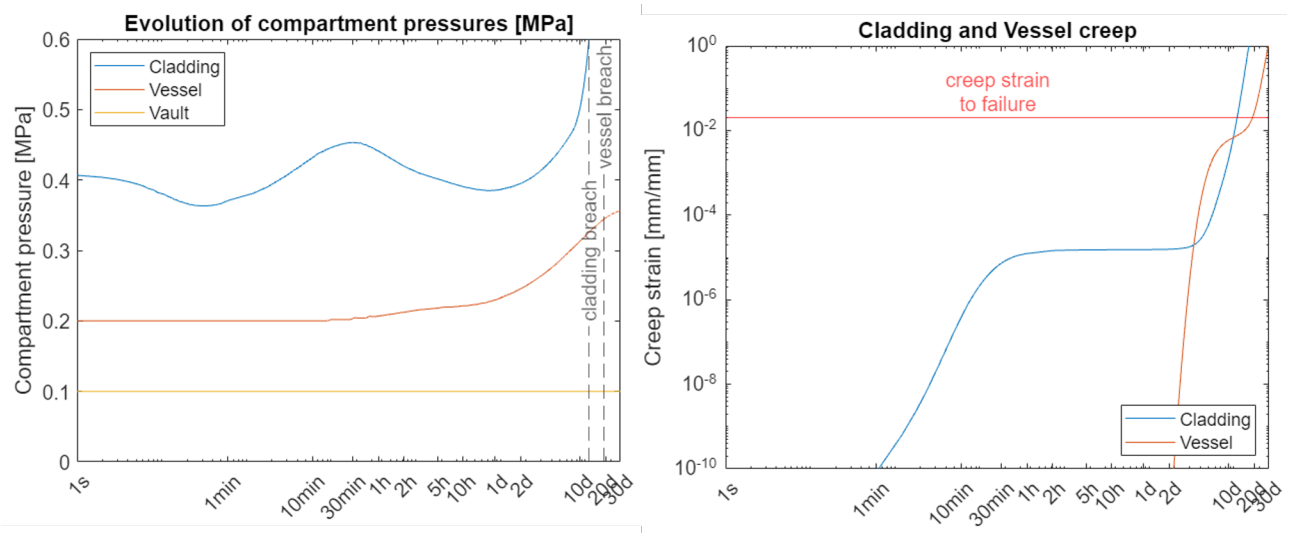

Figure 47: PLHR Compartment breach : Compartment pressures (**left**), Cladding and Vessel creep (**right**)

9.4.8 • Leakage rates

Vessel and Vault leakage rate values ($l_{1\to2}$ and $l_{2\to3}$) are justified in this section. Relevant orders of magnitude for conservative operational values of Vessel and Containment leakage rate are $0.1\%/day$ and $1\%/day$ respectively. The current state of research on the subject and the implementation of more advanced models are described below.

9.4.8.1 Vessel Leakage rate

When considering the vessel leakage rate, one has to model the leakage through gasketed joints. Gasketed joints differ in class depending on the clamping force applied. Material also influence the sealing performance of a flange joint. Models based on laminar theory and molecular flow or porous media theory have been developed with different tightness for graphite or compressed fibre gaskets [68]. However, the gaskets used to seal a reactor vessel are metal gaskets, whose sealing performance is far superior and to which these models are not applicable. Using the fractal characterization of the sealing surface of metallic gaskets, Feng et al. developed an analytical leakage model applicable to gaskets used in Nuclear vessels [69]. These models are however not widespread, and further work is needed to define more precisely the leakage regimes of a metallic ring joint. An order of magnitude of 0.1% day is a conservative approximation of the vessel leak rate and is applied as reference value by the code.

9.4.8.2 Containment Leakage rate

In the code, a containment leakage rate in nominal operation of 1 vol%/day is considered as indicated in RG 1.183 [9]. Nevertheless, a potential increase in this leakage rate is envisaged with increasing internal vault pressure and deformation applied to the containment steel liner. This model is based on leak rate measurements carried out on the Surry Pressurised water reactor and is implemented in MELCOR [61]. The initial curve shows the containment leak rate as a function of the

Internal Pressure / Containment Design Pressure ratio. Here, arguing that stress is proportional to pressure at a given temperature, the dependence of the containment leak rate is translated as a function of the maximum stress exerted on the containment steel liner. The converted Containment Fragility Curve is displayed in Figure 48 (right). Increased containment leakage occurs once the steel liner yields, and is subject to different leakage regimes depending on this initial point. The first yield point depends on the steel liner yield strength, which itself depends on temperature as illustrated in Figure 48 (left, [70]). In the analysis, the steel liner temperature is assumed to be the mean value between the RCCS and the Reinforced Shielding temperatures. It is noted that all damage undergone to the liner is irreversible: a temperature decrease does not reduce the resulting containment leakage rate.

In MELCOR's Containment Fragility model, containment leakage rates reach values of 350%/day. However, code defined containment leakage rates, expressed in Equation (94), cannot exceed 100%/day. An equivalence between the values is obtained by considering that a leakage rate of $l = 350\ vol\%/day$ means that the compartment is emptied by 50% in 6.8h and by adopting the corresponding "half-empty" time $T_{\frac{1}{2}}$ in the definition of the transfer rate:

$$\Lambda_{3,2} = \frac{ln(2)}{T_{\frac{1}{2}}} = \frac{ln(2) \times l}{3600 \times 24 \times 50\%} \tag{105}$$

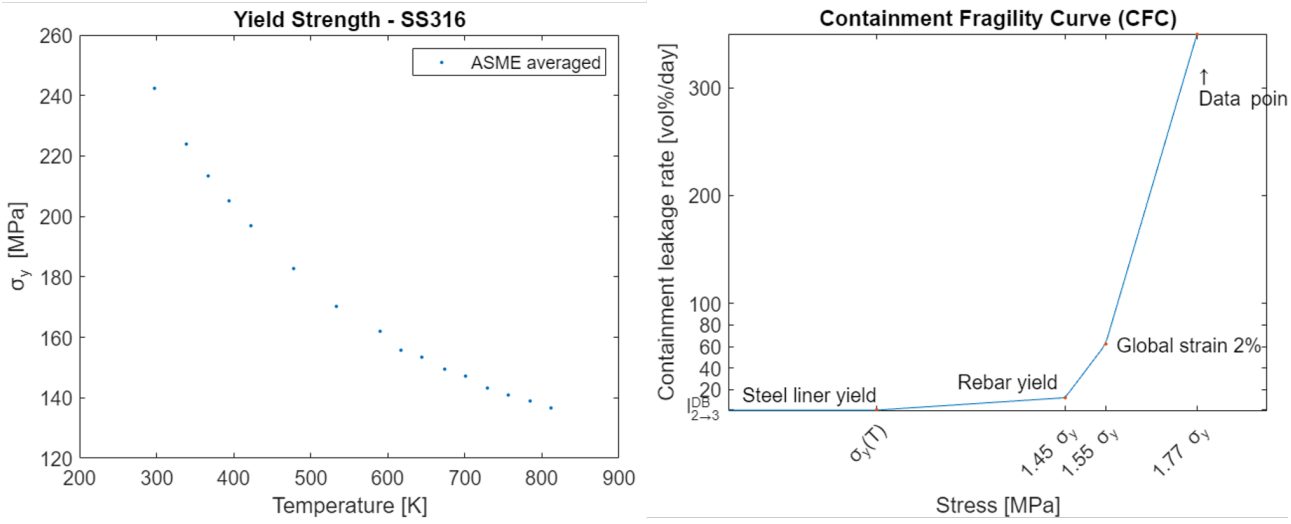

Figure 48: Containment Leakage dependence on Steel liner stress : SS316 yield strength ([70] **left**), Containment Fragility Curve (CFC [61] - **right**)

The steel liner containment is modeled as a rectangular pressurized vessel with dimensions of $a \times b \times c = 4.17 \times 4.17 \times 3.75\ m$. Resulting stress in pressurised rectangular vessels is assessed in the American Society of Mechanical Engineerins (ASME) Boiler and Pressure Vessel Code, Section VIII, whose results are reported in the *Structural Analysis and Design of Process Equipment book* [71] by Jawad et al. However, ASME Code results are criticised to be overconservative for large rectangular vessels with a width-to-length ratio of less than 4. The analytical model developed by Lee et al. [72] to determine the maximal stress in a non-stiffened pressurised rectangular vessel, is therefore adopted. The maximal stress in the rectangular pressure vessel structure in the case where $a = b > c$ is given by:

$$\sigma_{max} = \sigma_m + \sigma_b = \frac{P_{vault} P_M b}{w} + |\frac{6 P_{vault} P_B a^2}{w^2}| = 1.8 \times 10^5 \times P_{vault} \tag{106}$$

with :

- σ_{max} the maximal stress in the rectangular vessel (MPa),
- σ_m the membrane stress at the middle of the longest side (MPa),
- σ_b the maximal bending stress at the middle of the longest side (MPa),
- P_{vault} the vault inner pressure (MPa)
- $w = 0.006\ m$ the liner thickness (m)
- $a = b = 4.17\ m$ the rectangular vessel dimensions,
- P_M and P_B the bending and membrane parameters respectively, shown in Figure 49 $(\emptyset)$,

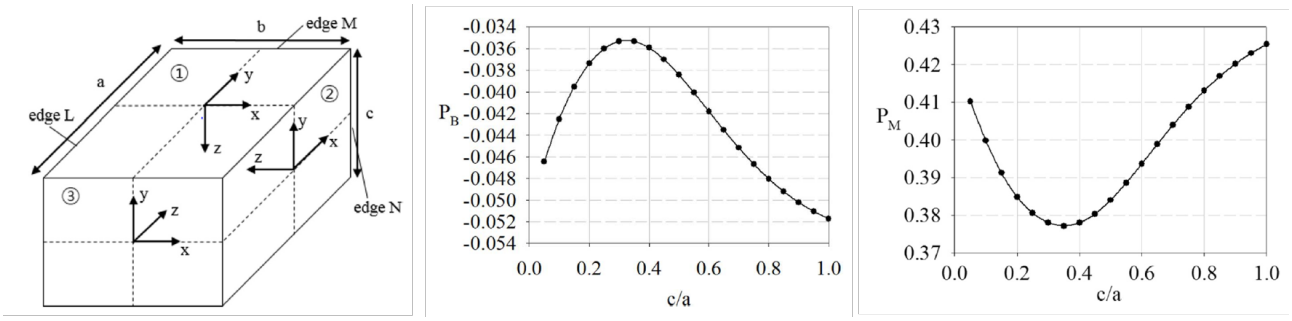

Figure 49: Non-Stiffened Pressurised rectangular Vessel bending and membrane stress parameters [72]

Considering the stress in the steel liner is that of a non-stiffened rectangular vessel is a strong conservative simplification. In practice, the steel liner structure is reinforced by 2 m of reinforced concrete. To take account of this phenomenon, it is assumed that the maximum stress calculated in Equation (106) is distributed between the liner and the concrete, considered as two materials placed in series. The resultant stress in the liner corresponds to the ratio of the Young's moduli of the steel and reinforced concrete multiplied by the total stress as expressed in Equation (107).

$$\sigma_{liner} = \frac{E_{SS316}(T)}{E_{SS316}(T) + E_{RC}} \sigma_{max} \tag{107}$$

The temperature-dependent Young's modulus of Stainless steel is taken from [70]: $E_{SS316}[GPa] = 200 - 0.08125 * (T[K] - 273.15)$. The Young's modulus of reinforced concrete depends on the relative amount of steel and concrete and of the material structure. An order of magnitude of $E_{RC} = 30\ GPa$ is assumed in the analysis.

In practice, global temperatures rise during a reactor cooling accident induces a pressure rise in the vault. This pressure rise accumulates until the resulting stress on the containment structure causes the steel liner to yield and increased leakage rates. This leakage rate grows until it compensates for

the internal gas expansion due to reactor temperature rise and containment internal pressure starts to decrease. It is noted that in the analysis, effective leakage (gas leaving the vault inducing a pressure drop) is only considered for leakage rates greater than 1 vol%/day as a conservative margin. It is also noted that finding the equilibrium containment leakage rate compensating for the containment internal gas expansion requires precision in this period of the analysis. A graph illustrating this phenomena and equilibrium is displayed in Figure 50.

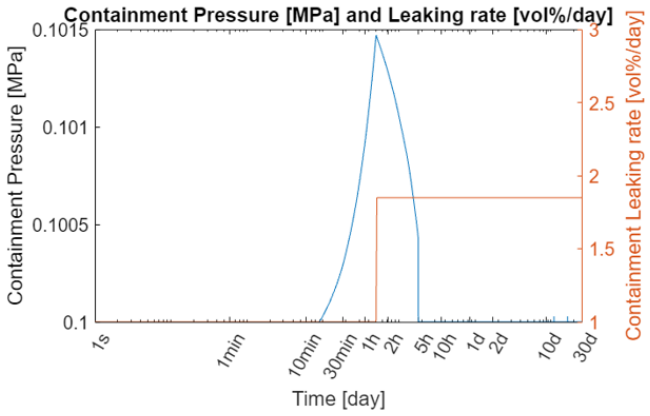

Figure 50: Steel Liner Yield and increased Leakage Equilibrium

9.4.9 • Iodine chemistry

Modelling the transport of iodine isotopes is of particular importance, since it accounts for a large proportion of volatile fission product released in terms of both source term and dose exposure. Iodine compounds are divided into 3 transport groups : Elemental iodine I_2 (reactive gas), Organic iodine (unreactive gas), and particulate iodine.

For an analysis on UO_2 fuel, RG 1.183 [9] requires to consider for iodine fuel release that 95 % is cesium iodide (CsI) in particulate form, 4.85 % elemental iodine, and 0.15 % organic iodide [7], based on the results established from NUREG-1465 [59]. However, the transport of these iodine species following release from the fuel may affect these assumed fractions.

In their MST development plan for Sodium Fast reactors (SFRs) [10], Argonne National Laboratory (ANL) assesses the evolution of sodium iodide in a sodium-based environment. CsI reacts with sodium as follows :

$$CsI + Na \longrightarrow NaI + Cs \tag{108}$$

In the case of SGTR, even with the primary sodium coolant drained before cladding breach occurs, the amount of evaporated and liquid sodium retained by capillarity still vastly exceeds the amount of CsI released by the fuel. The assumption is therefore made that in the SGTR vessel, all of cesium iodide CsI released is converted into sodium iodide NaI.

[7] RG 1.183 also prevents from considering any removal of organic iodine during the analysis.

Chemical reactions of sodium iodide NaI fumes is studied experimentally in [73]. In an inert gas (Argon) and dry atmosphere similar to the vessel and vault environment, it is assessed that 99.9 % of iodine remains in particulate form NaI and that 0.1 % converts to gaseous elemental iodine I_2. In air with relative humidity from 40 to 95 %, similar the environment's atmosphere, 98% of sodium iodide remains in particulate form and 2% is converted to gaseous elemental iodine I_2. These coefficients are applied to the original shares of iodine type at release depending on the compartment in question. The shares of each iodine type for the different compartments of the study are summarized in Table 30.

Table 30: Share (%) of each Iodine group for each compartment

Iodine type	**At release**	**Vessel - Vault**	**Environment**
2. Elemental iodine (reactive gas)	4.85	4.95	6.84
2. Organic iodine (unreactive gas)	0.15	0.15	0.15
2. Particulate Iodine	95 (CsI)	94.9 (NaI)	93.01 (NaI)

9.4.10 • Deterministic Reference MST results: TEDE and Emergency Zones

The default deterministic analysis results returned by the script *Mechanistic_Source_Term_Analysis.m*, whose process is outlined in preceding sections, are presented in this section. According to this analysis, the reactor is projected to experience a cladding breach after 12.6 days and vessel breaches after 19.1 days, based on the temperature profile depicted in Figure 38. Additionally, Figure 51 offers a comprehensive depiction of the time-dependent accident source term and public dose rate, highlighting singular events such as cladding and vessel breaches. Furthermore, Figure 52 details the transport of radionuclides through the reactor's physical barriers, accentuating the impact of removal models on the transport of each element. Finally, the TEDE at varying distances from the reactor for this reference, 1-month-long PLHR source term assessment is depicted in Figure 53. This figure also delineates the positions of the boundaries for the LPZ and the EPZ, indicating when the dose falls below the threshold limits of 25 rem and 1 rem, respectively. Notably, for the code reference parameters, the LPZ extends to 24m and the EPZ to 155m, which is significantly less (around 6 times less) than in the case of the large primary sodium coolant fire discussed in Section 9.3.

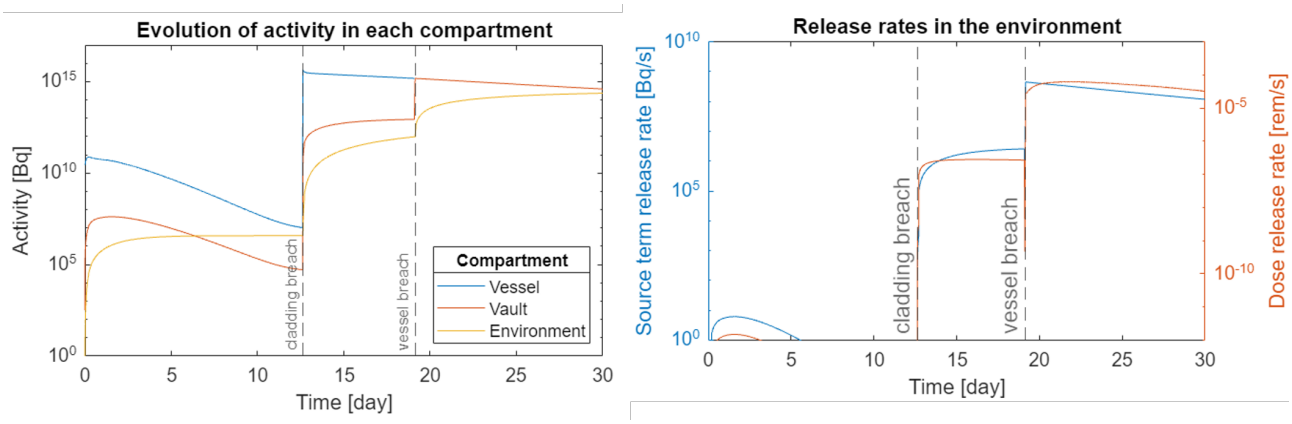

Figure 51: PLHR Compartment Activities **(left)** and Release rates in the Environment **(right)**

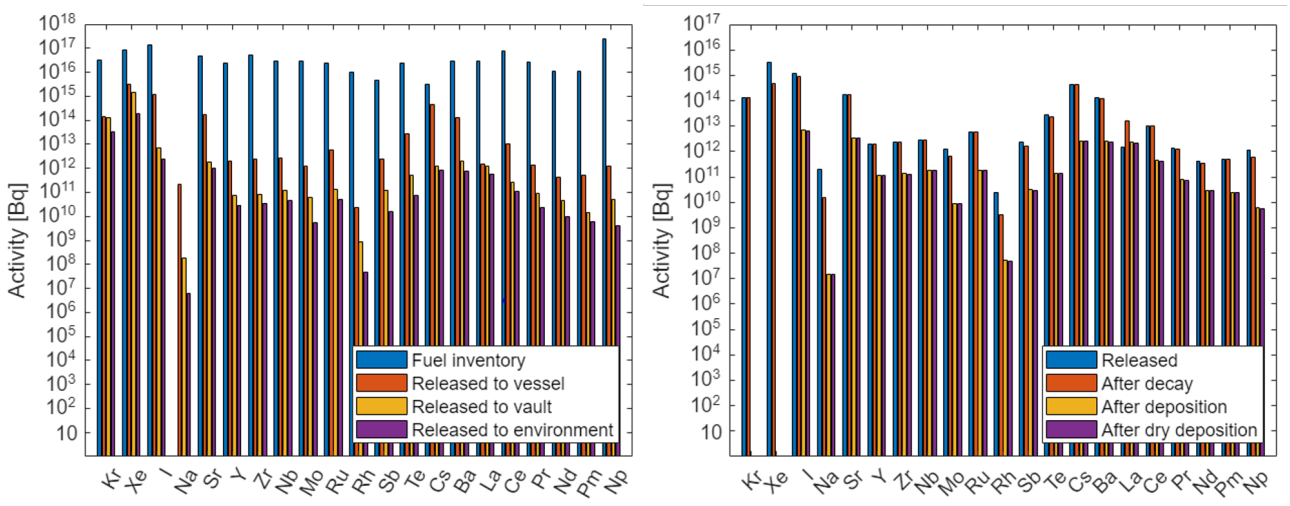

Figure 52: PLHR Radionuclide Transport through Compartments **(left)** and Removal models impact **(right)**

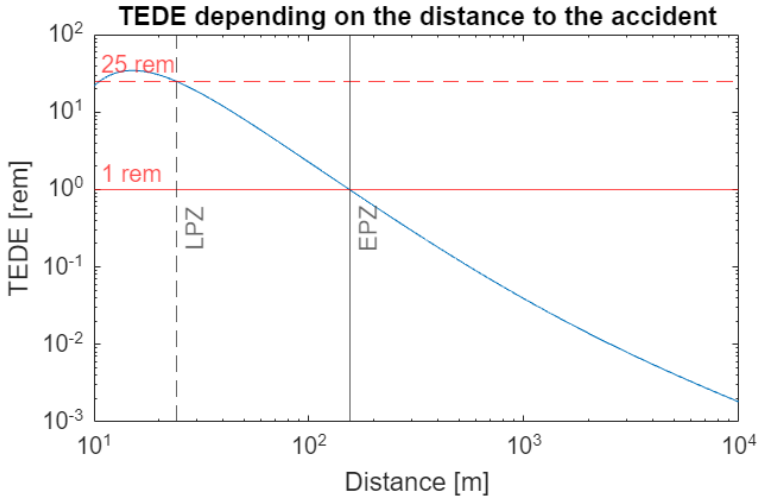

Figure 53: PLHR Reference MST simulation : Public dose exposure depending on distance to the accident

Table 31 summarizes the deterministic site boundary sizes. The LPZ and EPZ resulting from the PLHR analysis are consistent with the objective of allowing the operation of the SGTR in urban settings. Given that recovery measures to restore cooling functionality can typically be accounted for after 7 days, the sabotage of the RCCS and the PLHR incident may not necessitate the delineation of an LPZ or an EPZ. Figure 51 temporal analysis of the radiological release shows indeed that no radiological release significant enough for the TEDE to exceed the 25 rem LPZ threshold occurs before the vessel breaches after around 19 days. 19 days should therefore be considered as an important time marker before which intervention should take place for this scenario.

This analysis therefore underscores the potential for secure microreactor operation even within

Table 31: Site boundaries and time response for a PLHR scenario, deterministic result.

Low Population Zone (LPZ)	[HTML]FFFFFF24 m
Emergency Planning Zone (EPZ)	155 m
Maximal Expected Intervention Time	19 days

densely populated areas, suggesting a promising outlook for urban deployment. To further enhance security to prevent a PLHR, the focus should initially be on minimizing vulnerabilities susceptible to sabotage, such as the RCCS air pipes and inlet, during the design phase. Once operational, prioritizing the implementation of intervention protocols to restore reactor cooling emerges as the most effective mitigation strategy. Additionally, if the MST analysis confirms the performance of the current design in limiting accident progression, reinforcing physical barriers presents an opportunity to enhance resilience, although at an additional cost. Structural adjustments, such as modifying vessel thickness or fortifying containment steel liners, have the potential to delay breach and mitigate leaks in the event of an accident.

Addressing uncertainties surrounding release scenarios is essential due to the dynamic nature of nuclear security accidents. Precision in defining and quantifying these uncertainties is vital for accurate risk assessment. In the subsequent section, a probabilistic analysis provides further insights into the deterministic results by delineating a reasonable range for average and worst-case scenarios. Moreover, this analysis assesses the inherent variability in the outcomes, shedding light on potential fluctuations in results.

9.4.11 • Probabilistic study

A probabilistic study of the model is obtained by running the script *Statistical_Analysis.m*. The script conducts the same MST analysis several times, by considering the code inputs are random variables.

9.4.11.1 Uncertainties

RG 1.183 [9] states that sufficient safety margins should be maintained (qualitatively or quantitatively), including a margin to account for analysis uncertainties. The uncertainties considered for this analysis are as follows:

- Creep rate uncertainties are accounted as described in [66]. In practice, Cladding and Vessel rates calculated in Equations (102) and (104) are multiplied by a stochastic factor 10^{A1} with $A1$ following the Normal distribution : $A1 \sim \mathcal{N}(\mu, \sigma) = \mathcal{N}(0, 0.339)$.
- Creep strains to failure for cladding and vessel are assumed to follow a uniform distribution in the range 1-8% : $\epsilon_f \sim \mathcal{U}(1\%, 8\%)$. Indeed, reference 2% creep strain to failure values for the cladding and vessel are conservative ones. According to Yamada from Argonne National Laboratories [74], cladding creep strain failure depends of temperature and hoop stress conditions, giving values ranging from a few percent to approximately 30%, with most experimental results ranging above 8%. As for the vessel, Chu et al. from Sandia National Laboratories [75] carried out vessel breach experiments with different temperature and pressure conditions. Out of all experiments, the minimal vessel deformation at the time of vessel failure was 8% strain. A uniform creep strain to failure distribution of 1 to 8% for cladding and vessel is therefore both conservative and more realistic than a fixed failure limit of 2% strain.
- Uncertainties are considered in the vessel and containment Design-Basis leaking rates, meaning leakage rates in nominal operations, representative of the construction hazards and the current state of the equipment. In the case of the vessel, we consider a possible variation around the already conservative leakage rate of 0.1%/day in the form of a normal distribution: $l_{1\to2} \sim \mathcal{N}(\mu, \sigma) = \mathcal{N}(0.1\%, 0.05\%)$. The Containment Design-Basis leakage rate probability distribution is extracted from the MELCOR Containment Fragility model [61] and displayed in Figure 54. The distribution is itself based on experimental measurements and annual nuclear plant visits. The piecewise distribution joins a loguniform distribution between 0 and 1% leakage rates covering 90% of the cumulative probability, and a uniform distribution between 1% and 10% for the remaining 0.1 probability. It is noted that the Code of federal Regulations appendix J mandates that the maximal containment leakage rate should be inferior to 1 $vol\%$ / day. This means that in 10% of cases, the model considers that the reactor is defective and does not comply with the government mandate. This result is supported by historical figures from NUREG/CR-4220 [76], concluding that a 30% unavailability of the containment was due to leakage in the 1.0 to 10.0 vol%/day range. While such a high unavailability is not supported by current results, it provides an upper bound based on historical findings.
- A conservative margin is applied to the calculated steel liner stress used to determine the increased containment leakage due to the steel liner yielding. The stress conservative margin probability distribution is extracted from the MELCOR Containment Fragility model [61] and displayed in Figure 55.

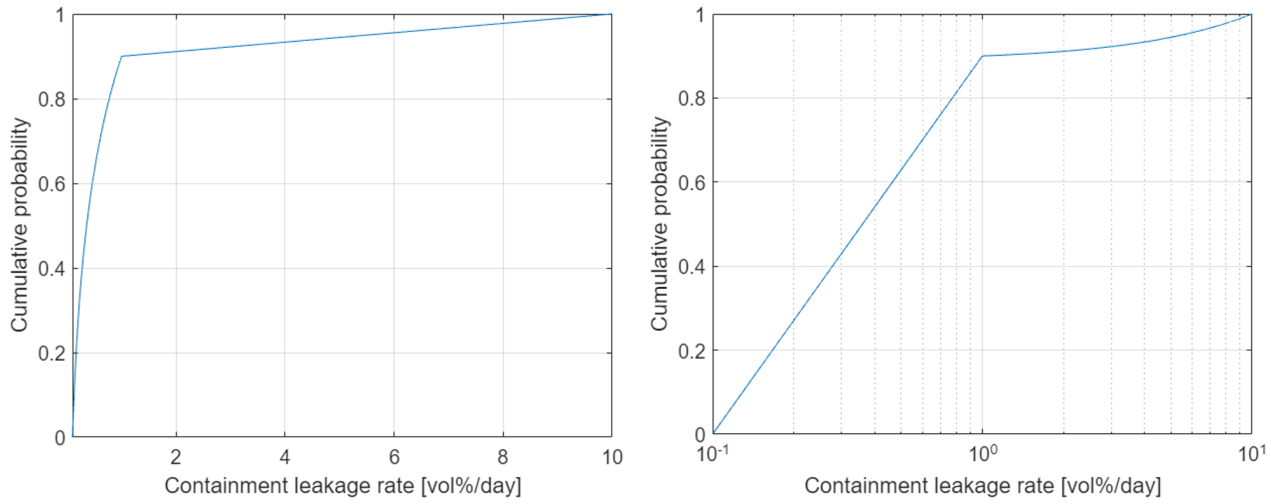

Figure 54: Design-Basis Containment Leakage rate Probability distribution [61]

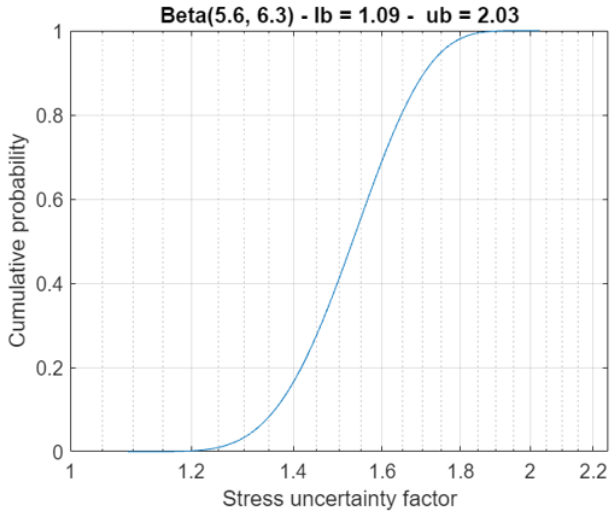

Figure 55: Steel Liner stress conservative margin probability distribution [61]

9.4.11.2 Sample size and Confidence intervals

The site boundary's probablity distribution law not being known a priori, a probabilistic analysis of the code generated results in terms of TEDE and in situ zone boundaries requires the use non-parametric statistical methods (or order statistics), which are applicable regardless of the underlying probability distribution.

By referring to Equation (109), one can employ Wilks' formula to determine the appropriate sample size for analysis, ensuring that the resulting confidence interval aligns with the boundaries of the sample. Wilks' method has already been used in the nuclear industry before. It incorporates both a tolerance limit and a confidence in its prediction, and can be applied to any random variable with a continuous probability distribution function. According to the table given in [77], a sample of size $N = 93$ ensures with a confidence level 95% that 95% of the result probability distribution is contained

within the sample boundaries. Accordingly, the script *Statistical_Analysis.m* returns the maximal site boundary value out of sample size of N = 93.

$$N\beta^{N-1} - (N-1)\beta^N = 1 - \alpha \tag{109}$$

with :

- N the sample size
- α the probability that at least β of the population will lie between the observed extremes

For further details on the shape of studied probability distributions, Kernel Distribution Estimations (KDE) are used to estimate the probability density of site boundaries (LPZ and EPZ) and 90% confidence intervals for EPZ and LPZ are returned.

To condense the results of this probabilistic study, Figure 56 in the Summary of results section shows the LPZ and EPZ probability distributions in case of a PLHR and compares it to the case of a primary sodium fire caused by an aircraft crash calculated in Section 9.3.

As mentionned in the comment in part 9.1, the site boundary distance distribution function is not continuous. Indeed, with the current atmospheric model, there is a non-null probability that the site boundary equals 0 m, and a null probability that the site boundary belongs to the interval $(0, 12m]$. Wilks formula can however only be applied to a random variable with a contiuous distribution function. The proof can be saved here by uniformly spreading the probability $\mathcal{P}(Site\ boundary = 0)$ over the interval $[0, 12m]$ and applying the Wilks formula to the corresponding random variable.

9.4.11.3 Summary of probabilistic results: TEDE and Emergency Zones

A probabilistic approach assigns probability distributions to the code inputs as described in Section 9.4.11. 93 input samples are processed, ensuring that 95% of the results probability distributions are contained within the result sample boundaries according to Wilks' formula. Kernel Density Estimations (KDE) are used to estimate more precisely the shape of probability densities of zones in siting size and provide 90% confidence intervals. TEDE and emergency zone boundaries probability distributions for the probabilistic analysis are displayed in Figure 56, and compared with the Aircraft crash primary sodium fire scenario source term determined in Section 9.3.

Table 32: Site boundaries for a PLHR scenario, probabilistic study.

	Reference Deterministic Study	*Median Statistic Value*	*90% Confidence Interval (KDE)*	*95% Confidence Interval (Wilks)*
Low Population Zone (LPZ)	[HTML]FFFFFF24 m	6 m	30 m	65 m
Emergency Planning Zone (EPZ)	155 m	113 m	185 m	375 m

Table 32 presents a summary of the LPZ and EPZ sizes derived from both deterministic and probabilistic analyses, providing median values alongside 90% and 95% confidence intervals. This

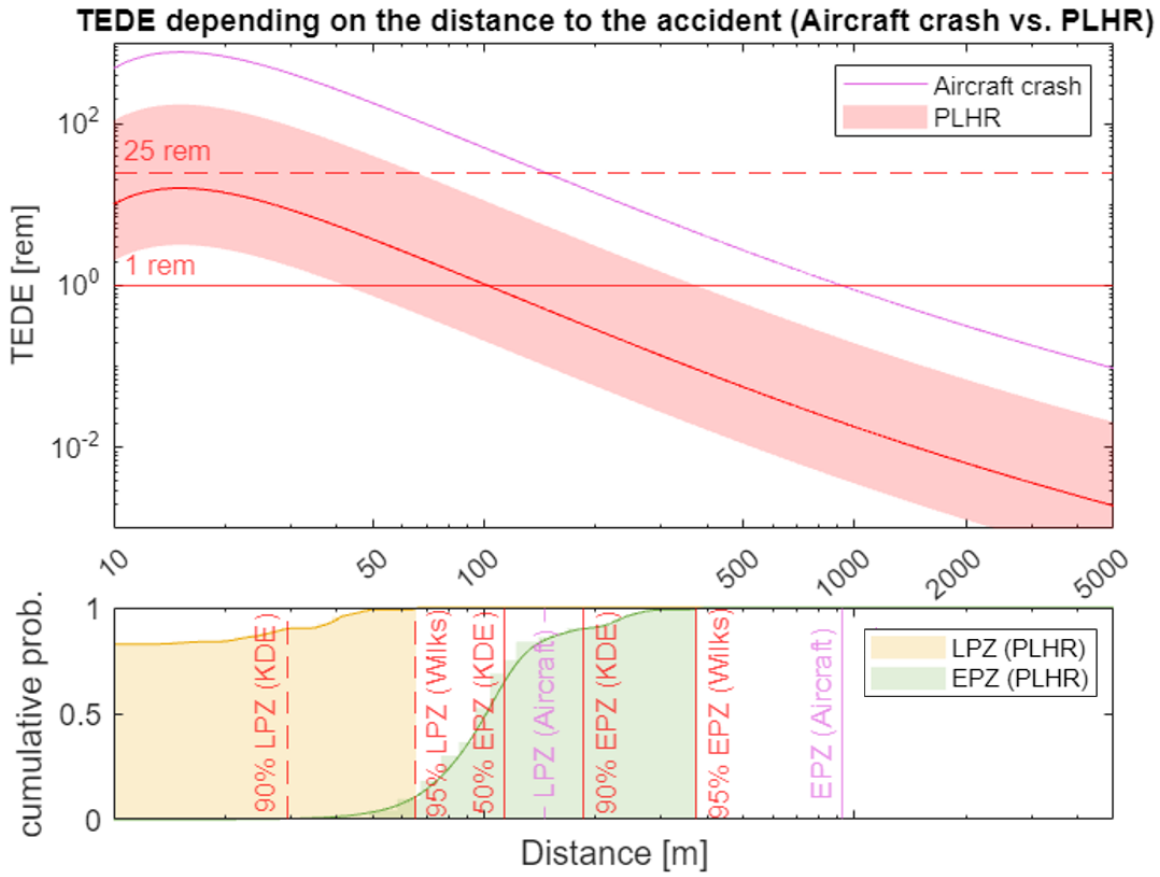

Figure 56: Public dose exposure depending on distance to the accident: Aircraft Crash vs. PLHR, and associated zones in siting size

probabilistic assessment allows to better visualise the impact of conservative margins in the reference analysis. Contrary to the deterministic reference result, the median LPZ value of 6m is reduced by a factor of 4. Additionally, the 90% and 95% confidence intervals exhibit substantial expansion compared to the deterministic reference values, reflecting the conservative nature of the probabilistic distributions. For instance, these distributions consider that legal containment leakage infrastructure standards are not met in 10% of cases in precaution for faulting equipment.

Figure 56 clearly illustrates the non-intuitive fact that a large primary sodium fire entails significantly more severe radiological impacts than the 95% confidence interval of a month-long PLHR for the microreactor. This underscores high coolant activation as the primary vulnerability for SGTR, while also highlighting Design-Basis aircraft crashes and contact blasts as the critical threats in terms of accident severity, elevating them as Maximal Hypothetical Threats (MHT) for the design.

10
CONCLUSIONS

INCLUDING USEFUL FUTURE WORK

The consequence-based analysis of SGTR emphasizes the inherent resilience of its design, revealing an already impressive capacity to withstand external assaults.

From the structural perspective, the study of several blasts, aircraft impacts and airborne missile impacts attacks on a microreactor vault reveals two significant conclusions. Firstly, restricting intruders' access to the vault is highly effective in mitigating the impact of explosive devices. While only 2kg of TNT is sufficient to breach 1ft of reinforced concrete (RC) with a contact blast, the required amount increases drastically to 450kg when the distance from the vault is just 10m. Secondly, using an RC radiation shield as a room around the vessel makes it nearly impossible for intruders to cause direct damage to the core. For a 2m-thick RC wall, roughly 150kg of TNT in contact with the wall would be required, which is highly unlikely to be achievable by intruders. Regarding aircraft impacts, the study of Cessna 172 and Falcon 7X cases indicates that preventing collapse of the impacted wall/roof requires a greater thickness compared to preventing penetration by the engines. In either case, neither a leisure aircraft nor a private jet can make its way through an RC radiation shield to cause core damage or release significant radioactivity. Furthermore, the results demonstrate that a Schedule 40 pipe cannot penetrate the core, making it an ineffective threat. Thus, this report highlights how some very serious threats (in terms of means employed and possible consequences) can be mitigated for a reasonable RC wall thickness. Using the RC structure surrounding the core as a radiation shield can be an effective and affordable way to both serve radioprotection purposes and provide the core with an extremely robust protection against external threats. Some insights about the position of the steel liner in the vault, as well as the type of RCCS system were also provided and could be used by nuclear vendors to guide their design choices from the physical security perspective.

When considering radiological risks, the analysis of representative Design-Basis scenarios highlights the high coolant activation as a main design security vulnerability for the SGTR design as it is. This elevates aircraft crashes and contact blasts to potential Maximal Hypothetical Threats (MHT) for the design. This result should encourage nuclear vendors to pay specific attention to the coolant safety and security features. Sodium fire extinguishing systems can be implemented, but if not operational, the ability of an intervention team to intervene on a radioactive sodium fire in a matter of tens of minutes will need to be considered. Addressing the vulnerability associated with coolant activation is also feasible by relocating the primary heat exchanger to Room A, shielded behind a robust 2m reinforced concrete wall, effectively eliminating the risk of leakage triggered by any DBT. To optimize spatial constraints, integration of the primary heat exchanger with the reactor vessel structure could be explored. Alternatively, reinforcing Room B's structure or the exchanger piping, or introducing additional physical barriers, could mitigate the risk of DBTs causing substantial primary sodium leaks. While these proposed configurations entail additional costs, the findings underscore the importance of early consideration of consequence-based security in the design process.

Security risks can also be mitigated through proactive measures aimed at anticipating and preparing for potential attack scenarios. In the event of contact blasts, it is imperative for the security

surveillance system to promptly detect intrusions, in time for the primary coolant to be drained. The installation time required for intruders is contingent upon their skills and training. To address the risk of aircraft crashes, locating the reactor in inaccessible areas such as basements or warehouses appears as the most effective strategy. If not implemented, the regulator could also request, in line with the principle of defense-in-depth, the addition of physical barriers to prevent coolant radioactivity release. Implementing Hesco barriers around the reactor is the most cost-effective way to make it resilient to large-scale explosion scenarios, while hindering and delaying trespassing. In scenarios involving sabotage of the Reactor Cavity Cooling System (RCCS) resulting in a Prolonged Loss-of-Heat-Removal (PLHR), setting up intervention processes to restore cooling before physical barriers breaching and any significant release occurring is crucial. Given that recovery measures can typically be accounted for after 7 days and that no release is expected within that timeframe, an intervention plan could even prevent a PLHR incident to necessitate the delineation of any LPZ or EPZ.

This comprehensive consequence-based security study suggests that deploying microreactors in urban areas may be feasible from a physical security standpoint. It underscores that extended loss of cooling does not pose a significant threat to public health. If coolant activation appears as a significant vulnerability for SGTR in several security scenarios, the risk can be effectively mitigated by integrating the primary heat exchanger within the main reactor vessel.

Considerations for useful future work

Improving the Structural assessment The possibility to mitigate the discussed threats by burying underground the reactor and its vault has not been thoroughly investigated, and could be the topic of future work. This could be a very economical strategy to provide additional protection against blasts or missiles: it reduces the target exposure (only one face of the reactor building could be hit provided it can be identified) and leverages the ground as a shock absorbing media. Moreover, from the source term perspective, such a configuration is likely to considerably diminish the amount of radioactivity released. However, two downsides must be mentioned: the earth provides a natural tamping which amplifies the effects of a blast from a buried explosive, and the RCCS inlet/outlet at the top of the structure could be more vulnerable to intruders tampering. The effects of the 6mm-steel containment liner on the overall structural behavior of the vault has not been accounted for. It is likely to increase significantly the resilience of the structure for example against missile penetration, or blast-induced deflection leading to collapse. Moreover, the potential failure of this liner has not been explored. This topic is important to understand radionuclide transport and the formation of pathways leading to radioactive release. To better estimate both the vault resilience against the threats herein mentioned and the source term, additional work could be conducted on the topic.

Improving the Source Term Assessment Suggestions to improve the Source Term Assessment of accident scenarios include advancements in sodium fire modeling, detailed mechanistic assessments during PLHR incidents, and refining atmospheric dispersion modeling:

Starting with scenarios involving a primary sodium fire (aircraft crash, large blast), current assumptions dictate the complete involvement of all fuel in the breached room, along with the prompt release of coolant activity into the atmosphere. Exploring the scenario impacts on key subsystems and considering sodium fire dynamics, including sodium deposition on debris, and plume elevation effects would enhance our comprehension of the scenario's impact on public health. It is however noted that

current NRC standards do not allow assessment credits based on these analyses, and overall, relocating the primary exchanger to Room A would lessen the need for such studies.

The mechanistic analysis of source terms during PLHR incidents could be refined to incorporate factors like adsorption and chemisorption of fission products with stainless steel pipes and cladding. Moreover, there is room for improvement in accounting for leakage rates and determining appropriate conservative margins in probabilistic studies. A comprehensive model for vessel metallic ring joint leakage regimes is currently lacking. Similarly, the existing containment leakage model, based on experimental data from large PWR containments, requires further validation for container-size buildings. Additionally, describing the leakage process through steel liner stress could be enhanced through advanced methodologies like Finite Element Method (FEM) simulations, integrating considerations for structural reinforcements and reinforced concrete layers. Finally, refinement in the probabilistic study could occur by incorporating a broader array of uncertainty sources and adjusting currently used distributions to suit microreactors.

Lastly, the adoption of an advanced atmospheric model, surpassing the limitations of the Gaussian plume 1D model, could enhance the estimation of public dose from the source term, by incorporating wind variability and site-specific considerations, thus providing a more accurate understanding of the accident's potential impact on public health.

ACKNOWLEDGMENTS

The authors wish to gratefully acknowledge the collaboration of Mr. Nikolaos Kallieros and Mr. Gyutae Park. We extend our sincere gratitude to Prof. Jacopo Buongiorno for his technical assistance and expertise. We are also indebted to Dr. Dave Grabaskas of Argonne National Laboratory and Dr. Matthew Denman of Kairos Power, for their useful suggestions. We acknowledge the financial support from our sponsors Shell, Equinor, ExxonMobil and EDF.

References

[1] U.S. Nuclear Regulatory Commission (NRC), *Rulemaking: Final rule: Emergency preparedness for small modular reactors and other new technologies*, No. SECY-22-0001, ML21200A059, Aug. 2023.

[2] Federal Register, *Code of federal regulations title 10*, Washington, D.C., 2023.

[3] B. Cipiti and A. Evans, "An evolving physical protection approach for small modular and microreators," in *Proceedings of the 2023 ANTPC Winter ANS Meeting*, Sandia National Lab., Washington D.C., 2023.

[4] U.S. Nuclear Regulatory Commission (NRC), *Rulemaking: Alternative physical security requirements for advanced reactors public meeting*, NRC-2017-0227-0036, ML22019A075, 2022.

[5] K. Shirvan, J. Buongiorno, R. L. Macdonald, B. Dunkin, S. Çetiner, E. Saito, T. Conboy, and C. Forsberg, "UO2-fueled microreactors: Near-term solutions to emerging markets," *Nuclear Engineering and Design*, vol. 412, pp. 112 470–112 470, Oct. 2023. DOI: https://doi.org/10.1016/j.nucengdes.2023.112470.

[6] E. Gateau, "Consequence-based security for micro-reactors," Department of Nuclear Science and Engineering (NSE), Massachusetts Institute of Technology (MIT), Research Internship report, 2022.

[7] U.S. Nuclear Regulatory Commission (NRC), *General site suitability criteria for nuclear power station*, Regulatory Guide 4.7, Revision 4, ML23348A082 and ML23123A095, 2023.

[8] U.S. Nuclear Regulatory Commission (NRC), *Emergency preparedness for small modular reactors and other new technologies*, Regulatory Guide 1.242, Revision 0, ML21238A072, 2022.

[9] U.S. Nuclear Regulatory Commission (NRC), *Alternative radiological source terms for evaluating design basis accidents at nuclear power reactors*, Regulatory Guide 1.183, ML21204A065, 2000.

[10] D. Grabaskas, M. Bucknor, J. Jerden, A. J. Brunett, M. Denman, A. Clark, and R. S. Denning, "Regulatory technology development plan sodium fast reactor. mechanistic source term development," Argonne National Lab.(ANL), Argonne, IL (United States), Tech. Rep. ANL-ART-3, 2015.

[11] N. Kallieros, K. Shirvan, and J. Buongiorno, "Safety analysis and design specifications of MIT's sodium graphite microreactor," in *Proceedings of the 2024 International Congress on Advances in Nuclear Power Plants (ICAPP)*, Las Vegas, 2024.

[12] S.A. McGuire, J.V. Ramsell Jr. and G.F. Athey, "Rascal 3.0.5: Description of models and methods," U.S. Nuclear Regulatory Commission (NRC), Office of Nuclear Security and Incident Response, Tech. Rep. NUREG-1887, ML072480633, 2007.

[13] D. R. Lide, *CRC Handbook of Chemistry and Physics*, 90th. CRC Press Inc, 2009, p. 2804, ISBN: 978-1-420-09084-0.

[14] National Fire Protection Association and Society of Fire Protection Engineers (SFPE), *SFPE Handbook of Fire Protection Engineering*. 2015.

[15] N. Iqbal and M. H. Salley, "Fire dynamic tools (fdts) quantitative fire hazard analysis methods for the u.s. nuclear regulatory commission fire protection inspection program," U.S. Nuclear Regulatory Commission (NRC), Tech. Rep. NUREG-1805, ML043290075, 2004.

[16] U.S. Department of Energy (DOE), "DOE handbook : Hazard and accident analysis handbook, interim use," BOOKLET to Provide Basic Information Regarding Health Effects of Radiation (1st Edition), 2018. DOI: DOE-HDBK-1224-2018.

[17] C. Mealy, M. Benfer, and D. Gottuk, "Fire dynamics and forensic analysis of liquid fuel fires," Office of Justice Programs, National Institute of Justice, Department of Justice, Tech. Rep. Grant No. 2008-DN-BX-K168, Feb. 2011. [Online]. Available: https://www.ncjrs.gov/pdffiles1/nij/grants/238704.pdf.

[18] G. Chambers, "Flight line extinguisher evaluation," U.S. Air Force, Tech. Rep. DOD-AGFSRS-76-9, 1977.

[19] M. Zabetakis and D. Burgess, "Research on hazards associated with the production of and handling of liquid hydrogen," U.S. Bureau of Mines, Tech. Rep. RI 5705, 1961.

[20] European Committee for Standardization (CEN), *Eurocode 1: Actions on structures — Part 1–2: General Actions—Actions on Structures Exposed to Fire*. Brussels, Belgium, 2002.

[21] W. McLain, "Investigation of the fire safety characteristics of portable polyethylene tanks containing flammable liquids," U.S. Coast Guard, Tech. Rep. Report No. CG-M-1-88, 1988.

[22] A. Taylor and D. J. Hards, "Engulfment fire tests on road tanker sections," Rarde Technical Report 7/75, Controller HMSO, Tech. Rep., 1975.

[23] D. N. Bilow and M. E. Kamara, "Fire and concrete structures," in *Structures Congress 2008*, pp. 1–10. DOI: 10.1061/41016(314)299. [Online]. Available: https://ascelibrary.org/doi/abs/10.1061/41016%28314%29299.

[24] International Atomic Energy Agency (IAEA), *Safety aspects of nuclear power plants in human induced external events: assessment of structures* (Safety Reports Series 87). 2018, ISBN: 978-92-0-101117-6. [Online]. Available: https://www.iaea.org/publications/10953/safety-aspects-of-nuclear-power-plants-in-human-induced-external-events-assessment-of-structures.

[25] J. Biggs, *Introduction to Structural Dynamics*. McGraw-Hill College, 1964.

[26] Department of Defense (DOD), "Design of Structures to Resist the Effects of Accidental Explosions," Report No UFC-3-340-02, Washington, D.C.: Department of Defense, Tech. Rep., 2008.

[27] M. Smith, *ABAQUS/Standard User's Manual, Version 6.9*, English. United States: Dassault Systèmes Simulia Corp, 2009.

[28] M. Hafezolghorani, F. Hejazi, R. Vaghei, M. S. B. Jaafar, and K. Karimzade, "Simplified damage plasticity model for concrete," *Structural Engineering International*, vol. 27, no. 1, pp. 68–78, 2017.

[29] P. Sherkar, A. Whittaker, and A. Aref, "Modeling the effects of detonations of high explosives to inform blast-resistant design," Tech. Rep MCEER-10-0009, 2010.

[30] Prolific North. "Barrier specialist hesco turns to enjoy digital for web revamp." (), [Online]. Available: https://www.prolificnorth.co.uk/news/barrier-specialist-hesco-turns-enjoy-digital-web-revamp/.

[31] U.S. Nuclear Regulatory Commission (NRC), "Characterizing explosive effects on underground structures," NRC NUREG/CR-7201, ML15245A640, Tech. Rep., 2015.

[32] A. Remennikov, I. Mentus, and B. Uy, "Explosive Breaching of Walls with Contact Charges: Theory and Applications," *International Journal of Protective Structures*, vol. 6, no. 4, pp. 629–647, 2015. DOI: 10.1260/2041-4196.6.4.629.

[33] Nuclear Energy Institute (NEI), "Methodology for performing aircraft impact assessment for new plant designs," Tech. Rep. NEI 07-13, 2011.

[34] Department of Energy (DOE), "DOE standard accident analysis for aircraft crash into hazardous facilities," Tech. Rep. DOE-STD-3014-2006, 1996.

[35] Q. Hossain, R. Kennedy, R. Murray, K. Mutreja, and B. Tripathi, "Evaluation technical support document, DOE Standard Accident analysis for aircraft crash into hazardous facilities," Lawrence Livermore National Laboratory, Tech. Rep. UCRL-ID-123577, 1997.

[36] C. Chelapati, R. Kennedy, and I. Wall, "Probabilistic assessment of aircraft hazard for nuclear power plants," *Nuclear Engineering and Design*, vol. 19, no. 2, May 1972.

[37] S. Dorofeev, V. Sidorov, A. Efimenko, A. Kochurko, M. Kuznetsov, B. Chaivanov, D. Matsukov, A. Pereverzev, and V. Avenyan, "Fireballs from deflagration and detonation of heterogeneous fuel-rich clouds," *Fire Saf. J.*, vol. 25, pp. 323–336, 1995.

[38] B.R. Terranova, A.S. Whittaker, and L. Schwer, "Design of concrete walls and slabs for wind-borne missile loadings," *Engineering Structures*, vol. 194, 2019.

[39] U.S. Nuclear Regulatory Commission (NRC), "Standard Review Plan: Missiles generated by extreme winds," Revision 4. Washington, D.C., Tech. Rep. 2015-07709, 2015, (ML14190A180).

[40] Department of Energy (DOE), "Natural phenomena hazards analysis and design criteria for DOE facilities," Tech. Rep. DOE-STD-1020-2016, 2016.

[41] U.S. Nuclear Regulatory Commission (NRC), "Design-basis tornado and tornado missiles for nuclear power plants," Tech. Rep. Regulatory Guide 1.76., ML053140225, Washington D.C. 2007.

[42] U.S. Nuclear Regulatory Commission (NRC), "Design-basis hurricane and hurricane missiles for nuclear power plants," Tech. Rep. Regulatory Guide 1.221. Washington D.C., ML110940300, 2011.

[43] American Nuclear Society (ANS), "Estimating tornado, hurricane, and extreme straight line wind characteristics at nuclear facility sites," La Grange Park, Illinois, Tech. Rep. ANS-2.3, 2016.

[44] B.R. Terranova, A.S. Whittaker, and L. Schwer, "Empirical formulae for the design of reinforced concrete nuclear power plants to resist the effects of wind-borne missile impact: a critical review," *Nucl Technol*, vol. 204, no. 2, pp. 119–30, 2018.

[45] B.R. Terranova, A.S. Whittaker, and L. Schwer, "Response of plain concrete panels impacted by wind-borne missiles at varying angles of obliquity," in *Transactions, 25th International Conference on Structural Mechanics in Reactor Technology (SMiRT25), Charlotte, NC*, 2018.

[46] U.S. Nuclear Regulatory Commission (NRC) and U.S. Environmental Protection Agency (EPA) Task Force on Emergency Planning, "Planning basis for the development of state and local government radiological emergency response plans in support of light water nuclear power plants," Tech. Rep. NUREG-0396, ML051390356, 1978.

[47] H. Panofsky and J. Dutton, *Atmospheric Turbulence: Models and Methods for Engineering Applications*. Wiley, 1984, ISBN: 9780471057147. [Online]. Available: https://books.google.com/books?id=pSVRAAAAMAAJ.

[48] E. Gallego. "7th MEREIA webinar on basic concepts - introduction to atmospheric dispersion process and models." IAEA Event Reference No. EVT2301631, IAEA. (Mar. 22, 2023).

[49] International Atomic Energy Agency (IAEA), *Atmospheric Dispersion In Nuclear Power Plant Siting, A Safety Guide* (Safety Series 50-SG-S3). Vienna: International Atomic Energy Agency, 1980.

[50] S. B. Ross, J. P. Rishel, and P. P. Lowry, "Engineering evaluation of x/q values consistent with regulatory guide 1.145," Pacific Northwest National Lab., Richland, WA, Tech. Rep. PNNL-19217, 2010.

[51] K. Eckerman, J. Harrison, H.-G. Menzel, and C. Clement, "Icrp publication 119: Compendium of dose coefficients based on icrp publication 60," *Annals of the International Commission on Radiological Protection (ICRP)*, 2012.

[52] K. F. Eckerman and J. C. Ryman, "External exposure to radionuclides in air, water, and soil," U.S. Environmental Protection Agency (EPA), Federal Guidance Report No. 12, 1993.

[53] R. Newman, "The ignition and burning behavior of sodium metal in air," *Progress in Nuclear Energy*, vol. 12, no. 2, pp. 119–147, 1983.

[54] P. Sahoo, S. Kannan, P. Muralidharan, and K. Chandran, "Studies on release and deposition behavior of cesium from contaminated sodium pools and cesium trap development for fbtr," in *Technical Committee Meeting on Evaluation of Radioactive Materials Release and Sodium Fires in Fast Reactors*, 1996.

[55] S. Kahawara, T. Murata, and N. Sagawa, "Release of sodium and radioisotopes into air associated with sodium combustion," *Journal of Nuclear Science and Technology*, vol. 13, pp. 382–388, 1976.

[56] U.S. Nuclear Regulatory Commission (NRC), "Snap/radtrad 4.0: Description of models and methods," Office of Nuclear Regulatory Research, Tech. Rep. NUREG/CR-7220, ML16160A019, 2016.

[57] L. Humphries, B. Beeny, F. Gelbard, D. Louie, and J. Phillips, *MELCOR Computer Code Manuals. Vol. 2: Reference Manual. Version 2.2.9541*. 2017, SAND2017-0876 O, Sandia National Laboratories.

[58] D. Grabaskas, M. Bucknor, and J. Jerden, "Development of the simplified radionuclide transport (srt) code version 2.0 for versatile test reactor (vtr) mechanistic source term calculation," in *Proceedings of the 2022 International Conference on Fast Reactors and Related Fuel Cycles (FR21)*, 2022.

[59] L. Soffer, S. B. Burson, C. M. Ferrell, R. Y. Lee, and J. N. Ridgely, "Accident source terms for light-water nuclear power plants: Final report," U.S. Nuclear Regulatory Commission (NRC), Tech. Rep. NUREG-1465, 1995.

[60] Thermal Fluids Central. "Thermophysical properties of sodium." (), [Online]. Available: https://www.thermalfluidscentral.org/encyclopedia/index.php/Thermophysical_Properties:_Sodium.

[61] U.S. Nuclear Regulatory Commission (NRC), "State-of-the-art reactor consequence analyses project, uncertainty analysis of the unmitigated short-term station blackout of the surry power station," Office of Nuclear Regulatory Research, Tech. Rep. NUREG/CR-7262, 2022.

[62] T. Starkus, D. Grabaskas, and S. Shahbazi, "Review and assessment of available data regarding the behavior of sodium aerosols," Argonne National Lab., Tech. Rep. ANL/NSE-22/68, 2023.

[63] M. P. Kissane, "A review of radionuclide behaviour in the primary system of a very-high-temperature reactor," *Nuclear Engineering and Design*, vol. 239, no. 12, 2009.

[64] A. Cheniour, G. Pastore, J. M. Harp, C. M. Petrie, and N. A. Capps, "Application of BISON to UO_2 minifuel fission gas release analysis," *Journal of Nuclear Materials*, vol. 565, p. 153 686, 2022, ISSN: 0022-3115. DOI: 10.1016/j.jnucmat.2022.153686.

[65] J. F. Saltsman, "Theorical analysis of swelling characteristics of cylindrical uranium dioxide fuel pins with a nobium - 1%-zirconium clad," Lewis Research Center, Cleveland, Ohio, Tech. Rep. NASA TM X-2717, 1973.

[66] R. Ecob, "Primary creep of 20/25Nb stainless steel AGR fuel cladding under conditions of non-steady stress and stress state," *Nuclear Energy*, vol. 29, no. 4, pp. 279–286, 1990.

[67] F. Yang, H. Xue, L. Zhao, and J. Tian, "Calculations and modeling of material constants in hyperbolic-sine creep model for 316 stainless steels," *Applied Mechanics and Materials*, vol. 457-458, p. 185, 2013. DOI: 10.4028/www.scientific.net/AMM.457-458.185.

[68] N. R. Nelson, N. S. Prasad, and A. S. Sekhar, "Structural integrity and sealing behaviour of bolted flange joint: A state of art review," *International Journal of Pressure Vessels and Piping*, vol. 204, pp. 104 975–104 975, Aug. 2023. DOI: https://doi.org/10.1016/j.ijpvp.2023.104975.

[69] X. Feng and B. Q. Gu, "Fractal characterization of sealing surface topography and leakage model of metallic gaskets," *Key Engineering Materials*, vol. 353-358, pp. 2977–2980, Sep. 2007. DOI: https://doi.org/10.4028/www.scientific.net/kem.353-358.2977.

[70] B. G. Kim, J. L. Rempe, D. L. Knudson, K. G. Condie, and B. H. Sencer, *In-situ Creep Testing Capability Development for Advanced Test Reactor*. Aug. 2010. DOI: https://doi.org/10.2172/989906.

[71] M. H. Jawad and J. R. Farr, *Structural analysis and design of process equipment*. Hoboken, NJ: Wiley, 2019, ISBN: 9781119102830.

[72] J. Lee, Y. Choi, C. Jo, and D. Chang, "Design of a prismatic pressure vessel: An engineering solution for non-stiffened-type vessels," *Ocean Engineering*, vol. 142, pp. 639–649, Sep. 2017. DOI: https://doi.org/10.1016/j.oceaneng.2017.07.039.

[73] M. Naritomi, M. Murata, and Y. Yoshida, "Monitoring technique for radioiodine in sodium aerosol," Japan Atomic Energy Research Institute, Tokai, Ibaraki, Japan, Tech. Rep., 1971.

[74] H. Yamada, "Failure of type 316 stainless steel cladding during thermal transients," *Journal of Nuclear Materials*, vol. 78, no. 1, pp. 24–32, Nov. 1978. DOI: https://doi.org/10.1016/0022-3115(78)90500-7.

[75] T. Chu, M. Pilch, J. Bentz, and A. Behbahani, "Experimental investigation of creep behavior of reactor vessel lower head," Sandia National Lab., Albuquerque, NM, Tech. Rep. NEA-CSNI-R–1998-18, 1998.

[76] P. J. Pelto, K. R. Ames, and R. H. Gallucci, "Reliability analysis of containment isolation systems," Pacific Northwest National Lab., Richland, WA, Tech. Rep. NUREG/CR-4220; PNL-5432, 1985.

[77] A. J. Harman, "Wilk's tolerance limit sample sizes," *The Indian Journal of Statistics, Series A (1961-2002)*, vol. 29, no. 2, pp. 215–218, 1967.